



THE UNIVERSITY *of* EDINBURGH

Edinburgh Research Explorer

## Proteome profile of peripheral myelin in healthy mice and in a neuropathy model

**Citation for published version:**

Siems, SB, Jahn, O, Eichel, MA, Kannaiyan, N, Wu, L-MN, Sherman, D, Kusch, K, Hesse, D, Jung, RB, Fledrich, R, Sereda, MW, Rossner, MJ, Brophy, P & Werner, HB 2020, 'Proteome profile of peripheral myelin in healthy mice and in a neuropathy model', *eLIFE*. <https://doi.org/10.7554/eLife.51406>

**Digital Object Identifier (DOI):**

[10.7554/eLife.51406](https://doi.org/10.7554/eLife.51406)

**Link:**

[Link to publication record in Edinburgh Research Explorer](#)

**Document Version:**

Peer reviewed version

**Published In:**

eLIFE

**General rights**

Copyright for the publications made accessible via the Edinburgh Research Explorer is retained by the author(s) and / or other copyright owners and it is a condition of accessing these publications that users recognise and abide by the legal requirements associated with these rights.

**Take down policy**

The University of Edinburgh has made every reasonable effort to ensure that Edinburgh Research Explorer content complies with UK legislation. If you believe that the public display of this file breaches copyright please contact [openaccess@ed.ac.uk](mailto:openaccess@ed.ac.uk) providing details, and we will remove access to the work immediately and investigate your claim.



## FOR PEER REVIEW - CONFIDENTIAL

**Proteome profile of peripheral myelin in healthy mice and in a neuropathy model**

Tracking no: 27-08-2019-TR-eLife-51406R2

**Impact statement:** Comprehensive compendium of myelin proteins in the peripheral nervous system and method to address molecular diversity of myelin sheaths in health and disease.**Competing interests:** No competing interests declared**Author contributions:**

Sophie Siems: Sophie B. Siems performed all experiments not specified otherwise, conducted statistical analysis, contributed to analysis and interpretation of data. Olaf Jahn: Olaf Jahn performed proteome analysis, contributed to analysis and interpretation of data. Maria Eichel: Maria A. Eichel performed teased fiber labeling and microscopy. Nirmal Kannaiyan: Nirmal Kannaiyan performed bioinformatic analysis of RNA-Seq data. Lai Man Wu: Lai Man N. Wu performed histological analysis. Diane Sherman: Diane L. Sherman performed histological analysis. Kathrin Kusch: Kathrin Kusch provided unpublished reagents. Dörte Hesse: Dörte Hesse contributed to proteome analysis. Ramona Jung: Ramona B. Jung performed biochemical purification of myelin. Robert Fledrich: Robert Fledrich provided an unpublished RNA-Seq dataset. Michael Sereda: Michael W. Sereda provided an unpublished RNA-Seq dataset. Moritz Rossner: Moritz J. Rossner supervised bioinformatic analysis of RNA-Seq data. Peter Brophy: Peter J. Brophy supervised histological analysis. Hauke Werner: Hauke B. Werner conceived, designed and directed the study, analyzed and interpreted data and wrote the article.

**Funding:**

Deutsche Forschungsgemeinschaft (DFG): Hauke B. Werner, WE 2720/2-2; Deutsche Forschungsgemeinschaft (DFG): Hauke B. Werner, WE 2720/4-1; Deutsche Forschungsgemeinschaft (DFG): Hauke B. Werner, WE 2720/5-1; Deutsche Forschungsgemeinschaft (DFG): Moritz J. Rossner, RO 4076/3-2; Wellcome: Peter Brophy, 0842424 The funders had no role in study design, data collection and interpretation, or the decision to submit the work for publication.

**Data Availability:**

All data generated or analysed during this study are included in the manuscript and supporting files. This includes the mass spectrometry proteomics data. Source data files have been provided for Figures 1, 3 and 5. Additional to being provided in the source data files, mass spectrometry proteomics data have been deposited to the PRIDE/ProteomeXchange Consortium with dataset identifier PXD015960 and are available to the reviewers. Please use username: reviewer94825@ebi.ac.uk and password: C5r5SVMi. Upon acceptance of the manuscript, we will notify PRIDE support to make the dataset publicly available.

N/A

**Ethics:**

Human Subjects: No Animal Subjects: Yes Ethics Statement: All animal work conformed to United Kingdom legislation (Scientific Procedures) Act 1986 and to the University of Edinburgh Ethical Review Committee policy; Home Office project license No. P0F4A25E9.

**Information for reviewers (full submissions):**

eLife aims to publish work of the highest scientific standards and importance in all areas of the life and biomedical sciences, from the most basic and theoretical work through to translational, applied and clinical research. Articles must be methodologically and scientifically rigorous, ethically conducted, and objectively presented according to the appropriate community standards.

You will be asked for a general assessment and a summary of any major concerns (ideally in fewer than 500 words), as well as a list of any minor comments (optional). You will also have the opportunity to comment on the statistical rigour of the work (optional).

In your general assessment, please articulate what is exciting and whether the work represents a significant contribution. Please note our guidelines about requests for additional work:

1. We will only request new work, such as experiments, analyses, or data collection, if the new data are essential to support the major conclusions. The authors must be able to do any new work in a reasonable time frame (additional work should be conducted and written up within two months); otherwise, we will usually reject the manuscript.
2. Any requests for new work must fall within the scope of the current submission and the technical expertise of the authors.

Our goal is to make peer review constructive and collaborative: after the reviews have been submitted independently, there is an online discussion between the reviewers in which each reviewer will see the identity of the other reviewers.



1  
2  
3  
4  
5  
6  
7  
8 **Proteome profile of peripheral myelin in healthy mice and in a neuropathy model**  
9

10  
11  
12  
13  
14  
15 Sophie B. Siems<sup>1,7</sup>, Olaf Jahn<sup>2,7</sup>, Maria A. Eichel<sup>1</sup>, Nirmal Kannaiyan<sup>3</sup>, Lai Man N. Wu<sup>4</sup>,  
16 Diane L. Sherman<sup>4</sup>, Kathrin Kusch<sup>1</sup>, Dörte Hesse<sup>2</sup>, Ramona B. Jung<sup>1</sup>, Robert Fledrich<sup>1,5</sup>,  
17 Michael W. Sereda<sup>1,6</sup>, Moritz J. Rossner<sup>3</sup>, Peter J. Brophy<sup>4</sup>, Hauke B. Werner<sup>1,\*</sup>  
18  
19  
20

21 **Affiliations**

22 <sup>1</sup>Department of Neurogenetics, Max Planck Institute of Experimental Medicine, 37075 Göttingen, Germany

23 <sup>2</sup>Proteomics Group, Max Planck Institute of Experimental Medicine, 37075 Göttingen, Germany

24 <sup>3</sup>Department of Psychiatry and Psychotherapy, University Hospital, LMU Munich, 80336 Munich, Germany

25 <sup>4</sup>Centre for Discovery Brain Sciences, University of Edinburgh, Edinburgh, EH16 4SB, UK

26 <sup>5</sup>Institute of Anatomy, University of Leipzig, 04103 Leipzig, Germany

27 <sup>6</sup>Department of Clinical Neurophysiology, University Medical Center, 37075 Göttingen, Germany

28 <sup>7</sup>These authors contributed equally to this work  
29

30 **\* Corresponding author**

31 Dr. Hauke Werner

32 Max Planck Institute of Experimental Medicine

33 Department of Neurogenetics

34 Hermann-Rein-Str. 3

35 D-37075 Göttingen, Germany

36 Tel.: +49 (551) 3899-759; Fax.: +49 (551) 3899-758

37 E-mail: [Hauke@em.mpg.de](mailto:Hauke@em.mpg.de)  
38

39 **Key words**

40 Schwann cell, peripheral nervous system (PNS), myelin proteome, neuropathy, Charcot-  
41 Marie-Tooth disease (CMT4F), periaxin (PRX), MCT1/SLC16A1, demyelination, axon  
42 degeneration, transcriptome  
43

44 **Word and figure count**

45 Abstract 149 words; Introduction/results/discussion 4786 words

46 6 main figures; 2 figure supplements; 2 main tables; 4 source data files  
47  
48

49 **ABSTRACT**

50

51 Proteome and transcriptome analyses aim at comprehending the molecular profiles of the  
52 brain, its cell-types and subcellular compartments including myelin. Despite the relevance of  
53 the peripheral nervous system for normal sensory and motor capabilities, analogous  
54 approaches to peripheral nerves and peripheral myelin have fallen behind evolving technical  
55 standards. Here we assess the peripheral myelin proteome by gel-free, label-free mass-  
56 spectrometry for deep quantitative coverage. Integration with RNA-Sequencing-based  
57 developmental mRNA-abundance profiles and neuropathy disease genes illustrates the utility  
58 of this resource. Notably, the periaxin-deficient mouse model of the neuropathy Charcot-  
59 Marie-Tooth 4F displays a highly pathological myelin proteome profile, exemplified by the  
60 discovery of reduced levels of the monocarboxylate transporter MCT1/SLC16A1 as a novel  
61 facet of the neuropathology. This work provides the most comprehensive proteome resource  
62 thus far to approach development, function and pathology of peripheral myelin, and a  
63 straightforward, accurate and sensitive workflow to address myelin diversity in health and  
64 disease.

65

66

## 67 INTRODUCTION

68

69 The ensheathment of axons with myelin enables rapid impulse propagation, a prerequisite  
70 for normal motor and sensory capabilities of vertebrates (1,2). This is illustrated by  
71 demyelinating neuropathies of the Charcot-Marie-Tooth (CMT) spectrum, in which mutations  
72 affecting myelin genes as *MPZ*, *PMP22*, *GJB1* and *PRX* impair myelin integrity and reduce  
73 the velocity of nerve conduction in the peripheral nervous system (PNS) (3).  
74 Developmentally, myelination by Schwann cells in peripheral nerves is regulated by axonal  
75 neuregulin-1 (4,5) and the basal lamina (6–8) that is molecularly linked to the abaxonal  
76 Schwann cell membrane via integrins and the dystroglycan complex (9–12). In adulthood,  
77 the basal lamina continues to enclose all axon/myelin-units (13), probably to maintain myelin.  
78 Beyond regulation by extracellular cues, myelination involves multiple proteins mediating  
79 radial sorting of axons out of Remak bundles, myelin membrane growth and layer  
80 compaction (14–18). For example, the Ig-domain containing myelin protein zero (MPZ; also  
81 termed P0) mediates adhesion between adjacent extracellular membrane surfaces in  
82 compact myelin (19). At their intracellular surfaces, myelin membranes are compacted by the  
83 cytosolic domain of MPZ/P0 together with myelin basic protein (MBP; previously termed P1)  
84 (20,21). Not surprisingly, MPZ/P0 and MBP were early identified as the most abundant  
85 peripheral myelin proteins (22,23).

86

87 A system of cytoplasmic channels through the otherwise compacted myelin sheath remains  
88 non-compacted throughout life, i.e. the adaxonal myelin layer, paranodal loops, Schmidt-  
89 Lanterman incisures (SLI), and abaxonal longitudinal and transverse bands of cytoplasm  
90 termed bands of Cajal (14,24,25). Non-compacted myelin comprises cytoplasm, cytoskeletal  
91 elements, vesicles and lipid-modifying enzymes, and thus numerous proteins involved in  
92 maintaining the myelin sheath. The cytosolic channels probably also represent transport  
93 routes toward Schwann cell-dependent metabolic support of myelinated axons (26–31).

94

95 Considering that Schwann cells constitute a major proportion of the cells in the PNS,  
96 oligonucleotide microarray analyses have been used for mRNA abundance profiling of total  
97 sciatic nerves (32,33). Indeed, these systematic approaches allowed the identification of  
98 novel myelin constituents including non-compact myelin-associated protein (NCMAP/MP11)  
99 (34). Notwithstanding that the number of known peripheral myelin proteins has grown in  
100 recent years, a comprehensive molecular inventory has been difficult to achieve because  
101 applications of systematic ('omics') approaches specifically to Schwann cells and peripheral  
102 myelin remained comparatively scarce, different from studies addressing oligodendrocytes  
103 and CNS myelin (35–40). One main reason may be that the available techniques were not

104 sufficiently straightforward for general application. For example, the protein composition of  
105 peripheral myelin was previously assessed by proteome analysis (41). However, at that time  
106 the workflow of sample preparation and data acquisition (schematically depicted in **Figure**  
107 **1A**) was very labor-intensive and required a substantial amount of input material; yet the depth  
108 of the resulting datasets remained limited. In particular, differential myelin proteome analysis  
109 by 2-dimensional fluorescence intensity gel electrophoresis (2D-DIGE) requires considerable  
110 hands-on-time and technical expertise (41,42). While this method is powerful for the  
111 separation of proteoforms (43), it typically suffers from under-representation of highly basic  
112 and transmembrane proteins. It thus allows comparing the abundance of only few myelin  
113 proteins rather than quantitatively covering the entire myelin proteome. Because of these  
114 limitations and an only modest sample-to-sample reproducibility, 2D-DIGE analysis of myelin,  
115 although unbiased, has not been commonly applied beyond specialized laboratories.

116

117 The aim of the present study was to establish a straightforward and readily applicable  
118 workflow to facilitate both comprehensive knowledge about the protein composition of  
119 peripheral myelin and systematic assessment of differences between two states, e.g.,  
120 pathological alterations in a neuropathy model. The major prerequisites were the biochemical  
121 purification of myelin, its solubilization with the detergent ASB-14 and the subsequent  
122 automated digestion with trypsin during filter-aided sample preparation (FASP). The tryptic  
123 peptides were fractionated by liquid chromatography and analyzed by mass spectrometry for  
124 gel-free, label-free quantitative proteome analysis. More specifically, we used nano-flow  
125 ultra-performance liquid chromatography (nanoUPLC) coupled to an electrospray-ionization  
126 quadrupole time-of-flight (ESI-QTOF) mass spectrometer with ion mobility option, providing  
127 an orthogonal dimension of peptide separation. The utilized data-independent acquisition  
128 (DIA) strategy relies on collecting data in an alternating low and elevated energy mode  
129 ( $MS^E$ ); it enables simultaneous sequencing and quantification of all peptides entering the  
130 mass spectrometer without prior precursor selection (reviewed in (44,45)). With their high-  
131 duty cycle utilized for the acquisition of precursor ions,  $MS^E$ -type methods are ideally suited  
132 to reliably quantify proteins based on peptide intensities. Notably, these methods do not  
133 involve the use of spectral libraries in the identification of proteins, different from other DIA  
134 strategies. Instead, the achieved high-complexity fragmentation spectra are deconvoluted  
135 before submission to dedicated search engines for peptide and protein identification (46,47).  
136 In the  $MS^E$  mode, this deconvolution involves precursor-fragment ion alignment solely on the  
137 basis of chromatographic elution profiles; on top, drift times of ion mobility-separated  
138 precursors are used in the high-definition (HD) $MS^E$  mode. An expansion of the latter referred  
139 to as the ultra-definition (UD) $MS^E$  mode, additionally implements drift time-dependent  
140 collision energy profiles for more effective precursor fragmentation (48,49).

141  
142  
143  
144  
145  
146  
147  
148  
149  
150  
151  
152

Indeed, compared to the previously used manual handling and in-gel digestion, the current workflow (schematically depicted in **Figure 1A**) is considerably less labor-intensive, and automated FASP increases sample-to-sample reproducibility. Moreover, differential analysis by quantitative mass spectrometry (MS) facilitates reproducible quantification of hundreds rather than a few distinct myelin proteins. Together, the present workflow increases the efficacy of assessing the peripheral myelin proteome while shifting the main workload from manual sample preparation and gel-separation to automated acquisition and processing of data. We propose that comprehending the expression profiles of all myelin proteins in the healthy PNS and in myelin-related disorders can contribute to advancing our understanding of the physiology and pathophysiology of peripheral nerves.



## 153 RESULTS

154

### 155 Purification of peripheral myelin

156 We biochemically enriched myelin as a light-weight membrane fraction from pools of sciatic  
157 nerves dissected from mice at postnatal day 21 (P21) using an established protocol of  
158 discontinuous sucrose density gradient centrifugation (41,50), in which myelin membranes  
159 accumulate at the interface between 0.29 and 0.85 M sucrose. By immunoblotting, proteins  
160 specific for both compact (MPZ/P0, MBP, PMP2) and non-compact (PRX) myelin were  
161 substantially enriched in the myelin fraction compared to nerve lysates (**Figure 1B**).  
162 Conversely, axonal (NEFH, KCNA1) and mitochondrial (VDAC) proteins and a marker for the  
163 Schwann cell nucleus (KROX20/EGR2) were strongly reduced in purified myelin. Together,  
164 these results imply that biochemically purified peripheral myelin is suitable for systematic  
165 analysis of its protein composition.

166

### 167 Proteome analysis of peripheral myelin

168 It has long been difficult to accurately quantify the most abundant myelin proteins both in the  
169 CNS (PLP, MBP, CNP (51)) and the PNS (MPZ/P0, MBP, PRX; this work), probably owing to  
170 their exceptionally high relative abundance. For example, the major CNS myelin constituents  
171 PLP, MBP and CNP comprise 17, 8 and 4% of the total myelin protein, respectively (51). We  
172 have recently provided proof of principle (52) that the mass spectrometric quantification of  
173 these high-abundant myelin proteins is accurate and precise when data are acquired in the  
174 MS<sup>E</sup> data acquisition mode and proteins are quantified according to the TOP3 method, i.e. if  
175 their abundance values are obtained based on the proven correlation between the average  
176 intensity of the three peptides exhibiting the most intense mass spectrometry response and  
177 the absolute amount of their source protein (53,54). Using data acquisition by MS<sup>E</sup> we  
178 confirmed that CNP constitutes about 4% of the total CNS myelin proteome and that the  
179 abundance of CNP in myelin from mice heterozygous for the *Cnp* gene (*Cnp*<sup>WT/null</sup>) compared  
180 to wild-type mice is 50.7% ( $\pm 0.4\%$ ), in agreement with the halved gene dosage and gel-  
181 based quantification by silver staining or immunoblotting (52).

182

183 When applying the MS<sup>E</sup> mode to PNS myelin, we quantified 351 proteins with a false  
184 discovery rate (FDR) of <1% at peptide and protein level and an average sequence coverage  
185 of 35.5% (**Figure 1-source data 1**). While MS<sup>E</sup> (labeled in orange in **Figure 1C**) indeed  
186 provided a dynamic range of more than four orders of magnitude and thus quantitatively  
187 covered the exceptionally abundant myelin proteins MPZ/P0, MBP and PRX, the number of  
188 quantified proteins appeared limited when spectral complexity was deconvoluted solely on  
189 the basis of chromatographic elution profiles. Accordingly, by using the UDMS<sup>E</sup> mode, which

190 comprises ion mobility for additional peptide separation as well as drift time-specific collision  
191 energies for peptide fragmentation, proteome coverage was increased about three-fold (1078  
192 proteins quantified; average sequence coverage 34.3%; **Figure 1-source data 1**). However,  
193 the dynamic range of UDMS<sup>E</sup> (labeled in blue in **Figure 1C**) was found to be somewhat  
194 compressed compared to that of MS<sup>E</sup>, which can be considered an expectable feature of  
195 traveling wave ion mobility devices (55), where the analysis of pulsed ion packages leads to  
196 a temporal and spatial binning of peptides during ion mobility separation. Indeed, this  
197 manifests as a ceiling effect for the detection of exceptionally intense peptide signals, which  
198 results in an underestimation of the relative abundance of MPZ/P0, MBP and PRX by  
199 UDMS<sup>E</sup>.

200

201 The complementary nature of the MS<sup>E</sup> and UDMS<sup>E</sup> data acquisition modes led us to  
202 conclude that a comprehensive analysis of the myelin proteome that facilitates both correct  
203 quantification of the most abundant proteins and deep quantitative coverage of the proteome  
204 would require analyzing the same set of samples with two different instrument settings for  
205 MS<sup>E</sup> and UDMS<sup>E</sup>, respectively. Considering that instrument time is a bottleneck for the  
206 routine differential proteome analysis of myelin from mutant mice, we aimed to combine the  
207 strengths of MS<sup>E</sup> and UDMS<sup>E</sup> into a single data acquisition mode. Based on a gene ontology  
208 enrichment analysis for cellular components of the 200 proteins of highest and lowest  
209 abundance from the UDMS<sup>E</sup> dataset, we realized that the 'bottom' of the quantified proteome  
210 is probably largely unrelated to myelin but dominated by contaminants from other subcellular  
211 sources including mitochondria. We thus reasoned that for a myelin-directed data acquisition  
212 mode, proteome depth may be traded in for a gain in dynamic range and devised a novel  
213 method referred to as dynamic range enhancement (DRE)-UDMS<sup>E</sup>, in which a deflection lens  
214 is used to cycle between full and reduced ion transmission during mass spectrometric  
215 scanning. Indeed, DRE-UDMS<sup>E</sup> quantified an intermediate number of proteins in PNS myelin  
216 (554 proteins; average sequence coverage 30.6%; **Figure 1-source data 1**) while providing  
217 an intermediate dynamic range (labeled in green in **Figure 1C**). We thus consider DRE-  
218 UDMS<sup>E</sup> as the data acquisition mode of choice most suitable for routine differential myelin  
219 proteome profiling (see below).

220

221 Overall, we found a high reproducibility between replicates and even among the different  
222 data acquisition modes as indicated by Pearson's correlation coefficients for protein  
223 abundance in the range of 0.765-0.997 (**Figure 1-supplement 1**). When comparing the  
224 proteins identified in PNS myelin using the three data acquisition modes, we found a very  
225 high overlap (**Figure 1D**). We also found a high overlap (**Figure 1E**) between the proteins  
226 identified in the present study by UDMS<sup>E</sup> and those detected in previous proteomic

227 approaches to PNS myelin (41,42), thus allowing a high level of confidence. Together, the  
228 three data acquisition modes exhibit distinct strengths in the efficient quantification of  
229 exceptionally abundant proteins (MS<sup>E</sup>), establishing a comprehensive inventory (UDMS<sup>E</sup>)  
230 and gel-free, label-free differential analysis of hundreds of distinct proteins (DRE-UDMS<sup>E</sup>) in  
231 peripheral myelin (see **Figure 1A**). Yet, analyzing the same set of samples by different  
232 modes may not always be feasible in all routine applications when considering required  
233 instrument time.

234

### 235 **Relative abundance of peripheral myelin proteins**

236 Considering that MS<sup>E</sup> provides the high dynamic range required for the quantification of the  
237 most abundant myelin proteins, we calculated the relative abundance of the 351 proteins  
238 identified in myelin by MS<sup>E</sup> (**Figure 1-source data 1**). According to quantitative assessment  
239 of this dataset, the most abundant PNS myelin protein, myelin protein zero (MPZ/P0),  
240 constitutes 44% (+/-4% relative standard deviation (RSD)) of the total myelin protein (**Figure**  
241 **2**). Myelin basic protein (MBP), periaxin (PRX) and tetraspanin-29 (CD9) constitute 18% (+/-  
242 1% RSD), 15% (+/-1%) and 1% (+/-0.2%) of the total myelin protein, respectively (**Figure 2**).  
243 For MPZ/P0 and MBP, our quantification by MS<sup>E</sup> is in agreement with but specifies prior  
244 estimations upon gel-separation and protein labeling by Sudan-Black, Fast-Green or  
245 Coomassie-Blue, in which they were judged to constitute 45–70% and 2–26% of the total  
246 myelin protein, respectively (22,56–58). However, gel-based estimates of the relative  
247 abundance of myelin proteins were not very precise with respect to many other proteins,  
248 including those of high molecular weight. Indeed, periaxin was identified as a constituent of  
249 peripheral myelin after the advent of gradient SDS-PAGE gels (59), which allowed improved  
250 migration of large proteins into gels. The present MS<sup>E</sup>-based quantification of myelin proteins  
251 also extends beyond and partially adjusts an earlier mass spectrometric approach (41).  
252 Indeed, the current approach identified and quantified more myelin proteins, probably owing  
253 to improved protein solubilization during sample preparation and higher dynamic range of the  
254 used mass spectrometer. By MS<sup>E</sup>, known myelin proteins (**Table 1**) collectively constitute  
255 over 85% of the total myelin protein (**Figure 2**) while proteins not yet associated with myelin  
256 account for the remaining 15% of the total myelin protein.

257

### 258 **Comprehensive compendium and comparison to the transcriptome**

259 To systematically elucidate the developmental abundance profiles of the transcripts that  
260 encode peripheral myelin proteins (**Figure 3**), we used our combined proteome inventory of  
261 peripheral myelin (**Figure 1-source data 1**) to filter mRNA abundance data of all genes  
262 expressed in sciatic nerves. By this strategy, **Figure 3** displays only those transcripts of  
263 which the protein product was identified in peripheral myelin rather than all transcripts in the

264 nerve, thereby discriminating myelin-related mRNAs from other mRNAs such as those  
265 present in peripheral axons, fibroblasts, immune cells etc. In this assessment we additionally  
266 included PMP22 although it was not detected by MS as well as 45 proteins exclusively  
267 identified by LC-MS of myelin separated by SDS-PAGE (**Figure 1-source data 1**). For  
268 mRNA abundance profiles, we exploited a recently established RNA sequencing analysis  
269 (RNA-Seq; platform Illumina HiSeq 2000) of sciatic nerves dissected from wild type Sprague  
270 Dawley rats at embryonic day 21 (E21), P6, P18 and 6 months (60). RNA-Seq provides  
271 reliable information about the relative abundance of all significantly expressed genes and is  
272 thus not limited to those represented on the previously used oligonucleotide microarrays  
273 (41). The raw data (accessible under GEO accession number GSE115930) were normalized  
274 (**Figure 3-source data 1**) and standardized. When comparing the proteome and  
275 transcriptome datasets, significant mRNA abundance was detected for all 1046 transcripts  
276 for which an unambiguous unique gene identifier was found (**Figure 3**). 126 transcripts  
277 displayed developmentally unchanged abundance levels, i.e., abundance changes below a  
278 threshold of 10% coefficient of variation (**Figure 3B; Figure 3-source data 1**).

279  
280 By fuzzy c-means clustering, those 920 transcripts that showed developmental abundance  
281 changes were grouped into 5 clusters (**Figure 3A; Figure 3-source data 1**). Among those,  
282 one cluster corresponds to an mRNA-abundance peak coinciding with an early phase of  
283 myelin biogenesis (cluster 'P6-UP'), which includes the highest proportion of known myelin  
284 proteins (**Table 1**) such as MPZ/P0, MBP, PRX, cyclic nucleotide phosphodiesterase (CNP),  
285 fatty acid synthase (FASN), myelin-associated glycoprotein (MAG), proteolipid protein  
286 (PLP/DM20), cell adhesion molecule-4 (CADM4/NECL4), connexin-29 (GJC3), claudin-19  
287 (CLDN19) and CKLF-like MARVEL-transmembrane domain containing protein-5 (CMTM5).  
288 However, many known myelin proteins clustered together according to their mRNA-  
289 abundance peak coinciding with a later phase of myelination (cluster 'P18-UP'), including  
290 peripheral myelin protein 2 (PMP2), tetraspanin-29 (CD9), tetraspanin-28 (CD81), connexin-  
291 32 (GJB1), plasmalipin (PLLP), junctional adhesion molecule-3 (JAM3), CD59 and  
292 dystrophin-related protein-2 (DRP2). The proportion of known myelin proteins was lower in  
293 the clusters corresponding to mRNA-abundance peaks in adulthood (clusters 'late-UP', 'U-  
294 shaped'). Yet, a considerable number of transcripts displayed abundance peaks at the  
295 embryonic time-point (cluster 'Descending'), including carbonic anhydrase 2 (CA2), cofilin-1  
296 CFL1), tubulin beta-4 (TUBB4b) and band 4.1-protein B (EPB41L3). Generalized, the  
297 clusters were roughly similar when comparing previous oligonucleotide microarray analysis  
298 of mouse sciatic nerves (41) and the RNA-Seq analysis of rat sciatic nerves (this study); yet,  
299 the latter provides information on a larger number of genes and with a higher level of

300 confidence. Together, clustering of mRNA abundance profiles allows categorizing peripheral  
301 myelin proteins into developmentally co-regulated groups.

302

303 When systematically assessing the proteins identified in myelin by gene ontology (GO)-term  
304 analysis, the functional categories over-represented in the entire myelin proteome included  
305 cell adhesion, cytoskeleton and extracellular matrix (labeled in turquoise in **Figure 4**). When  
306 analyzing the clusters of developmentally co-expressed transcripts (from **Figure 3**), proteins  
307 associated with the lipid metabolism were particularly enriched in the P6-UP and P18-UP  
308 clusters, while those associated with the extracellular matrix (ECM) were over-represented in  
309 the U-shaped and Descending clusters (**Figure 4**). For comparison, known myelin proteins  
310 (**Table 1**) were over-represented in the P6-UP and P18-UP clusters (**Figure 4**). Together,  
311 our proteome dataset provides comprehensive in-depth coverage of the protein constituents  
312 of peripheral myelin purified from the sciatic nerves of wild type mice, and comparison to the  
313 transcriptome allows identifying developmentally co-regulated and functional groups of  
314 myelin proteins. Our data thus supply a solid resource for the molecular characterization of  
315 myelin and for discovering functionally relevant myelin proteins.

316

### 317 **Neuropathy genes encoding myelin proteins**

318 Heritable neuropathies can be caused by mutations affecting genes preferentially expressed  
319 in neurons, Schwann cells or both (3,61–63). To systematically assess which neuropathy-  
320 causing genes encode peripheral myelin proteins, we compared our myelin proteome  
321 dataset with a current overview about disease genes at the NIH National Library of Medicine  
322 at <https://ghr.nlm.nih.gov/condition/charcot-marie-tooth-disease#genes>. Indeed, 31 myelin  
323 proteins were identified to be encoded by a proven neuropathy gene (**Table 2**), a  
324 considerable increase compared to eight disease genes found in a similar previous approach  
325 (41). Notably, this increase is owing to both the larger size of the current myelin proteome  
326 dataset (**Figure 1E**) and the recent discovery of numerous neuropathy genes by the  
327 widespread application of next generation sequencing.

328

### 329 **Pathological proteomic profile of peripheral myelin in a neuropathy model**

330 The results presented thus far were based on analyzing myelin of healthy wild type mice; yet  
331 we also sought to establish a straightforward method to systematically assess myelin  
332 diversity, as exemplified by alterations in a pathological situation. As a model we chose mice  
333 carrying a homozygous deletion of the periaxin gene (*Prx*<sup>-/-</sup>) (26,64). Periaxin (PRX) is the  
334 third-most abundant peripheral myelin protein (**Figure 2**) and scaffolds the dystroglycan  
335 complex in Schwann cells. *Prx*<sup>-/-</sup> mice represent an established model of Charcot-Marie-  
336 Tooth disease type 4F (65–67). Aiming to assess the myelin proteome, we purified myelin

337 from pools of sciatic nerves dissected from *Prx*<sup>-/-</sup> and control mice at P21. Upon SDS-PAGE  
338 separation and silver staining the band patterns appeared roughly similar (**Figure 5A**), with  
339 the most obvious exception of the absence of the high-molecular weight band constituted by  
340 periaxin in *Prx*<sup>-/-</sup> myelin. Yet, several other bands also displayed genotype-dependent  
341 differences in intensity. As expected, PRX was also undetectable by MS<sup>E</sup> in *Prx*<sup>-/-</sup> myelin, in  
342 which most of the total myelin protein was constituted by MPZ/P0 and MBP (**Figure 5B**;  
343 **Figure 5-source data 1**).

344  
345 Upon differential analysis by DRE-UDMS<sup>E</sup> (**Figure 5-source data 2**), multiple proteins  
346 displayed genotype-dependent differences as visualized in a heatmap displaying those 40  
347 proteins of which the abundance was reduced or increased with the highest statistical  
348 significance in *Prx*<sup>-/-</sup> compared to control myelin (**Figure 5C**). For example, the abundance of  
349 the periaxin-associated dystrophin-related protein 2 (DRP2) was strongly reduced in *Prx*<sup>-/-</sup>  
350 myelin, as previously shown by immunoblotting (9). Notably, the abundance of multiple other  
351 proteins was also significantly reduced in *Prx*<sup>-/-</sup> myelin, including the extracellular matrix  
352 protein laminin C1 (LAMC1; previously termed LAMB2), the laminin-associated protein  
353 nidogen (NID1), Ig-like cell adhesion molecules (CADM4, MAG), the desmosomal junction  
354 protein desmin (DES), cytoskeletal and cytoskeleton-associated proteins (EPB41L3, MAP1A,  
355 CORO1A, SPTBN1, various microtubular and intermediate filament monomers), the  
356 monocarboxylate transporter MCT1 (also termed SLC16A1) and the MCT1-associated (68)  
357 immunoglobulin superfamily protein basigin (BSG, also termed CD147). On the other hand,  
358 proteins displaying the strongest abundance increase in *Prx*<sup>-/-</sup> myelin included immune-  
359 related proteins (LGALS3, LYZZ2, CTSD), cytoskeletal and cytoskeleton-associated proteins  
360 (CAPG, CORO1C, CNN3, several myosin heavy chain subunits), peroxisomal enzymes  
361 (CAT, HSD17B4, MDH1) and known myelin proteins (PLLP/plasmolipin, CRYAB,  
362 GJB1/CX32). For comparison, the abundance of the marker proteolipid protein (PLP/DM20)  
363 (69) and the periaxin-associated integrin beta-4 (ITGB4) (12) in myelin was unaltered in *Prx*<sup>-/-</sup>  
364 myelin. Together, differential proteome analysis finds considerably more proteins and protein  
365 groups to be altered in *Prx*<sup>-/-</sup> myelin than previously known (**Figure 5C, D-D''''**), probably  
366 reflecting the complex pathology observed in this model (26,64).

367  
368 The monocarboxylate transporter MCT1/SLC16A1 expressed by myelinating  
369 oligodendrocytes (70,71) and Schwann cells (28,72) has been proposed to supply lactate or  
370 other glucose breakdown products to axons, in which they may serve as substrate for the  
371 mitochondrial production of ATP (73–75). In this respect it was striking to find the abundance  
372 of MCT1 significantly reduced in peripheral myelin when PRX is lacking (**Figure 5C**), a result  
373 that we were able to confirm by immunoblotting (**Figure 5E**) and immunolabeling of teased

374 fiber preparations of sciatic nerves (**Figure 5F**). Notably, reduced expression of MCT1 in  
375 *Slc16a1<sup>+/-</sup>* mice impairs axonal integrity at least in the CNS (70,76). The reduced abundance  
376 of MCT1 thus represents an interesting novel facet of the complex pathology in *Prx<sup>-/-</sup>* mice.  
377 Considering that the integrity of peripheral axons may be impaired in *Prx<sup>-/-</sup>* mice, we  
378 assessed their quadriceps nerves. Indeed, *Prx<sup>-/-</sup>* mice displayed reduced axonal diameters, a  
379 progressively reduced total number of axons and a considerable number of myelin whorls  
380 lacking a visible axon (**Figure 6**), indicative of impaired axonal integrity (77). Yet we note that  
381 molecular or neuropathological features other than the reduced abundance of MCT1  
382 probably also contribute to the axonopathy in *Prx<sup>-/-</sup>* mice.

383

384 Together, gel-free, label free proteome analysis provides a cost- and time-efficient method  
385 that provides an accurate, sensitive tool to gain systematic insight into the protein  
386 composition of healthy peripheral myelin and its alterations in pathological situations. Indeed,  
387 gel-free proteome analysis is particularly powerful and comprehensive compared to 2D-  
388 DIGE; the workflow presented here appears readily applicable to other neuropathy models,  
389 thereby promising discovery of relevant novel features of their neuropathology.

390

391

392 **DISCUSSION**

393

394 We used gel-free, label-free quantitative mass spectrometry to assess the protein  
395 composition of myelin biochemically purified from the sciatic nerves of wild-type mice,  
396 thereby establishing a straightforward and readily applicable workflow to approach the  
397 peripheral myelin proteome. The key to comprehensiveness was to combine the strengths of  
398 three data acquisition modes, i.e., MS<sup>E</sup> for correct quantification of high-abundant proteins,  
399 UDMS<sup>E</sup> for deep quantitative proteome coverage including low-abundant proteins and DRE-  
400 UDMS<sup>E</sup> for differential analysis. We suggest that DRE-UDMS<sup>E</sup> provides a good compromise  
401 between dynamic range, identification rate and instrument run time for routine differential  
402 myelin proteome profiling as a prerequisite for a molecular understanding of myelin  
403 (patho)biology. We have also integrated the resulting compendium with RNA-Seq-based  
404 mRNA abundance profiles in peripheral nerves and neuropathy disease loci. Beyond  
405 providing the largest peripheral myelin proteome dataset thus far, the workflow is appropriate  
406 to serve as starting point for assessing relevant variations of myelin protein composition, e.g.,  
407 in different nerves, ages, species and in pathological conditions. The identification of  
408 numerous pathological alterations of myelin protein composition in the *Prx*<sup>-/-</sup> neuropathy  
409 model indicates that the method is well suited to assess such diversity.

410

411 Aiming to understand nervous system function at the molecular level, multiple 'omics'-scale  
412 projects assess the spatio-temporal expression profiles of all mRNAs and proteins in the  
413 CNS including oligodendrocytes and myelin (35–39). Yet, peripheral nerves are also  
414 essential for normal sensory and motor capabilities. Prior approaches to the molecular  
415 profiles of Schwann cells and PNS myelin thus far, however, were performed >8 years ago  
416 (32–34,41,78–80), and the techniques have considerably advanced since. For example,  
417 current gel-free, label-free mass spectrometry can simultaneously identify and quantify the  
418 vast majority of proteins in a sample, thereby providing comprehensive in depth-information.  
419 Moreover, RNA-Seq technology has overcome limitations of the previously used microarrays  
420 for characterizing mRNA abundance profiles with respect to the number of represented  
421 genes and the suitability of the oligonucleotide probes. The present compendium thus  
422 provides high confidence with respect to the identification of myelin proteins, their relative  
423 abundance and their developmental mRNA expression profiles. This view is supported by the  
424 finding that over 80% of the total myelin proteome is constituted by approximately 50  
425 previously known myelin proteins. We believe that the majority of the other identified proteins  
426 represent low-abundant myelin-associated constituents in line with the high efficiency of  
427 biochemical myelin purification. Doubtless, however, the myelin proteome also comprises



428 contaminants from other cellular sources, underscoring the need of independent validation  
429 for establishing newly identified constituents as true myelin proteins.

430

431 Do myelin proteins exist that escape identification by standard proteomic approaches?  
432 Indeed, some proteins display atypically distributed lysine and arginine residues, which  
433 represent the cleavage sites of the commonly used protease trypsin. The tryptic digest of  
434 these proteins leads to peptides that are not well suited for chromatographic separation  
435 and/or mass spectrometric detection/sequencing, as exemplified by the small hydrophobic  
436 tetraspan-transmembrane myelin proteins MAL (81) and PMP22 (82). We can thus not  
437 exclude that additional proteins with atypical tryptic digest patterns exist in peripheral myelin,  
438 which would need to be addressed by the use of alternative proteases. Moreover, potent  
439 signaling molecules including erbB receptor tyrosine kinases (83,84) and G-protein coupled  
440 receptors (GPRs) (85–87) display exceptionally low abundance. Such proteins may be  
441 identified when applying less stringent identification criteria, e.g., by requiring the sequencing  
442 of only one unique peptide per protein. However, lower stringency would also result in  
443 identifying false-positive proteins, which we wished to avoid for the purpose of the present  
444 compendium. We note that a truly comprehensive spatio-temporally resolved myelin  
445 proteome should preferentially also include systematic information about protein isoforms  
446 and post-translational modifications, which still poses technical challenges.

447

448 Mutations affecting the periaxin (*PRX*) gene in humans cause CMT type 4F (65,88–90); the  
449 neuropathology resulting from mutations affecting periaxin has been mainly investigated in  
450 the *Prx*<sup>-/-</sup> mouse model. Indeed, *Prx*<sup>-/-</sup> mice display a progressive peripheral neuropathy  
451 including axon/myelin-units with abnormal myelin thickness, demyelination, tomaculae, onion  
452 bulbs, reduced nerve conduction velocity (64), reduced abundance and mislocalization of the  
453 periaxin-associated DRP2 (9) and reduced internode length (26). Absence of SLIs (64) and  
454 bands of Cajal (26) imply that the non-compact myelin compartments are impaired when  
455 PRX is lacking. In the differential analysis of myelin purified from *Prx*<sup>-/-</sup> and control mice we  
456 find that the previously reported reduced abundance of DRP2 (9) represents one of the  
457 strongest molecular changes in the myelin proteome when PRX is lacking. Notably, the  
458 reported morphological changes in this neuropathy model (9,26,64) go along with alterations  
459 affecting the abundance of multiple other myelin-associated proteins, including junctional,  
460 cytoskeletal, extracellular matrix and immune-related proteins as well as lipid-modifying  
461 enzymes. Thus, the neuropathology in *Prx*<sup>-/-</sup> mice at the molecular level is more complex  
462 than previously anticipated. It is striking that the abundance of the monocarboxylate  
463 transporter MCT1/SLC16A1 that may contribute to the metabolic supply of lactate from  
464 myelinating cells to axons (27–31) is strongly reduced in *Prx*<sup>-/-</sup> myelin. Considering that

465 MCT1 in Schwann cells mainly localizes to Schmidt Lanterman incisures (SLI) (28) and that  
466 SLI are largely absent from myelin when PRX is lacking (64), the reduced abundance of  
467 MCT1 in *Prx*<sup>-/-</sup> myelin may be a consequence of the impaired myelin ultrastructure. Yet,  
468 considering that SLI are part of the cytosolic channels that may represent transport routes  
469 toward Schwann cell-dependent metabolic support of myelinated axons, the diminishment of  
470 MCT1 may contribute to reduced axonal diameters or axonal loss in *Prx*<sup>-/-</sup> mice, probably in  
471 conjunction with other molecular or morphological defects. Together, the in depth-analysis of  
472 proteins altered in neuropathy models can contribute to an improved understanding of nerve  
473 pathophysiology.

474

475 Compared to a previous approach (41), the number of proven neuropathy genes of which the  
476 encoded protein is mass spectrometrically identified in peripheral myelin has increased four-  
477 fold from eight to 32 in the present study. This reflects both that the number of proteins  
478 identified in myelin has approximately doubled and that more neuropathy genes are known  
479 due to the common use of genome sequencing. We note that our compendium comprises  
480 not only myelin-associated proteins causing (when mutated) demyelinating CMT1 (e.g.,  
481 MPZ/P0, NEFL, PMP2) or intermediate CMT4 (GDAP1, NDRG1, PRX) but also axonal  
482 CMT2 (RAB7, GARS, HSPB1). Yet, the expression of genes causative of CMT2 is not  
483 necessarily limited to neurons, as exemplified by the classical myelin protein MPZ/P0.  
484 Indeed, a subset of *MPZ*-mutations causes axonal CMT2I or CMT2J (91–95), probably  
485 reflecting impaired axonal integrity as consequence of a mutation primarily affecting  
486 Schwann cells. We also note that the nuclear *EGR2/KROX20* causative of demyelinating  
487 CMT1D has not been mass spectrometrically identified in myelin, reflecting that Schwann cell  
488 nuclei are efficiently removed during myelin purification.

489

490 While morphological analysis of peripheral nerves by light and electron microscopy is routine  
491 in numerous laboratories, systematic molecular analysis has been less straightforward.  
492 Using the sciatic nerve as a model, we show that systematic assessment of the myelin  
493 proteome and the total nerve transcriptome are suited to determine comprehensive  
494 molecular profiles in healthy nerves and in myelin-related disorders. Myelin proteome  
495 analysis can thus complement transcriptome analysis in assessing development, function  
496 and pathophysiology of peripheral nerves.

497

498 **MATERIALS AND METHODS**

499

500 **Mouse models**

501 *Prx*<sup>-/-</sup> mice (64) were kept on c57Bl/6 background in the animal facility of the University of  
502 Edinburgh (United Kingdom). Genotyping was by PCR on genomic DNA using the forward  
503 primers 5'-CAGATTTGCT CTGCCCAAGT and 5'-CGCCTTCTAT CGCCTTCTTGAC in  
504 combination with reverse primer 5'-ATGCCCTCAC CCACTAACAG. The PCR yielded a 0.5  
505 kb fragment for the wildtype allele and a 0.75 kb product for the mutant allele. The age of  
506 experimental animals is given in the figure legends. All animal work conformed to United  
507 Kingdom legislation (Scientific Procedures) Act 1986 and to the University of Edinburgh  
508 Ethical Review Committee policy; Home Office project license No. P0F4A25E9.

509

510 **Myelin purification**

511 A light-weight membrane fraction enriched for myelin was purified from sciatic nerves of mice  
512 by sucrose density centrifugation and osmotic shocks as described (41,52). Myelin  
513 accumulates at the interface between 0.29 and 0.85 M sucrose. *Prx*<sup>-/-</sup> and wild type control  
514 C57Bl/6 mice were sacrificed by cervical dislocation at postnatal day 21 (P21). For each  
515 genotype, myelin was purified as three biological replicates (n=3); each biological replicate  
516 representing a pool of 20 sciatic nerves dissected from 10 mice. Protein concentration was  
517 determined using the DC Protein Assay Kit (Bio-Rad).

518

519 **Filter-aided sample preparation for proteome analysis**

520 Protein fractions corresponding to 10 µg myelin protein were dissolved and processed  
521 according to a filter-aided sample preparation (FASP) protocol essentially as previously  
522 described for synaptic protein fractions (96) and as adapted to CNS myelin (52,97). Unless  
523 stated otherwise, all steps were automated on a liquid-handling workstation equipped with a  
524 vacuum manifold (Freedom EVO 150, Tecan) by using an adaptor device constructed in-  
525 house. Briefly, myelin protein samples were lysed and reduced in lysis buffer (7 M urea, 2 M  
526 thiourea, 10 mM DTT, 0.1 M Tris pH 8.5) containing 1% ASB-14 by shaking for 30 min at  
527 37°C. Subsequently, the sample was diluted with ~10 volumes lysis buffer containing 2%  
528 CHAPS to reduce the ASB-14 concentration and loaded on centrifugal filter units (30 kDa  
529 MWCO, Merck Millipore). After removal of the detergents by washing twice with wash buffer  
530 (8 M urea, 10 mM DTT, 0.1 M Tris pH 8.5), proteins were alkylated with 50 mM  
531 iodoacetamide in 8 M urea, 0.1 M Tris pH 8.5 (20 min at RT), followed by two washes with  
532 wash buffer to remove excess reagent. Buffer was exchanged by washing three times with  
533 50 mM ammonium bicarbonate (ABC) containing 10 % acetonitrile. After three additional  
534 washes with 50 mM ABC/10% acetonitrile, which were performed by centrifugation to ensure

535 quantitative removal of liquids potentially remaining underneath the ultrafiltration membrane,  
536 proteins were digested overnight at 37°C with 400 ng trypsin in 40 µl of the same buffer.  
537 Tryptic peptides were recovered by centrifugation followed by two additional extraction steps  
538 with 40 µl of 50 mM ABC and 40 µl of 1% trifluoroacetic acid (TFA), respectively. Aliquots of  
539 the combined flow-throughs were spiked with 10 fmol/µl of yeast enolase-1 tryptic digest  
540 standard (Waters Corporation) for quantification purposes and directly subjected to analysis  
541 by liquid chromatography coupled to electrospray mass spectrometry (LC-MS). A pool of all  
542 samples was injected at least before and after any sample set to monitor stability of  
543 instrument performance.

544

#### 545 **Mass spectrometry**

546 Nanoscale reversed-phase UPLC separation of tryptic peptides was performed with a  
547 nanoAcquity UPLC system equipped with a Symmetry C18 5 µm, 180 µm × 20 mm trap  
548 column and a HSS T3 C18 1.8 µm, 75 µm × 250 mm analytical column (Waters Corporation)  
549 maintained at 45°C. Injected peptides were trapped for 4 min at a flow rate of 8 µl/min 0.1%  
550 TFA and then separated over 120 min at a flow rate of 300 nl/min with a gradient comprising  
551 two linear steps of 3-35% mobile phase B in 105 min and 35-60% mobile phase B in 15 min,  
552 respectively. Mobile phase A was water containing 0.1% formic acid while mobile phase B  
553 was acetonitrile containing 0.1% formic acid. Mass spectrometric analysis of tryptic peptides  
554 was performed using a Synapt G2-S quadrupole time-of-flight mass spectrometer equipped  
555 with ion mobility option (Waters Corporation). Positive ions in the mass range  $m/z$  50 to 2000  
556 were acquired with a typical resolution of at least 20,000 FWHM (full width at half maximum)  
557 and data were lock mass corrected post-acquisition. UDMS<sup>E</sup> and DRE-UDMS<sup>E</sup> analyses  
558 were performed in the ion mobility-enhanced data-independent acquisition mode with drift  
559 time-specific collision energies as described in detail by Distler et al. (48,49). Specifically, for  
560 DRE-UDMS<sup>E</sup> a deflection device (DRE lens) localized between the quadrupole and the ion  
561 mobility cell of the mass spectrometer was cycled between full (100% for 0.4 sec) and  
562 reduced (5% for 0.4 sec) ion transmission during one 0.8 sec full scan. Continuum LC-MS  
563 data were processed for signal detection, peak picking, and isotope and charge state  
564 deconvolution using Waters ProteinLynx Global Server (PLGS) version 3.0.2 (47). For  
565 protein identification, a custom database was compiled by adding the sequence information  
566 for yeast enolase 1 and porcine trypsin to the UniProtKB/Swiss-Prot mouse proteome and by  
567 appending the reversed sequence of each entry to enable the determination of false  
568 discovery rate (FDR). Precursor and fragment ion mass tolerances were automatically  
569 determined by PLGS 3.0.2 and were typically below 5 ppm for precursor ions and below 10  
570 ppm (root mean square) for fragment ions. Carbamidomethylation of cysteine was specified  
571 as fixed and oxidation of methionine as variable modification. One missed trypsin cleavage

572 was allowed. Minimal ion matching requirements were two fragments per peptide, five  
573 fragments per protein, and one peptide per protein. The FDR for protein identification was set  
574 to 1% threshold.

575

### 576 **Analysis of proteomic data**

577 For each genotype (*Prx*<sup>-/-</sup> and wild type control mice sacrificed at P21), biochemical fractions  
578 enriched for PNS myelin were analyzed as three biological replicates (n=3 per condition);  
579 each biological replicate representing a pool of 20 sciatic nerves dissected from 10 mice. The  
580 samples were processed with replicate digestion and injection, resulting in four technical  
581 replicates per biological replicate and thus a total of 12 LC-MS runs per condition to be  
582 compared, essentially as previously reported for CNS myelin (36,97). The freely available  
583 software ISOQuant ([www.isoquant.net](http://www.isoquant.net)) was used for post-identification analysis including  
584 retention time alignment, exact mass and retention time (EMRT) and ion mobility clustering,  
585 peak intensity normalization, isoform/homology filtering and calculation of absolute in-sample  
586 amounts for each detected protein (48,49,98) according to the TOP3 quantification approach  
587 (53,54). Only peptides with a minimum length of seven amino acids that were identified with  
588 scores above or equal to 5.5 in at least two runs were considered. FDR for both peptides and  
589 proteins was set to 1% threshold and only proteins reported by at least two peptides (one of  
590 which unique) were quantified using the TOP3 method. The parts per million (ppm)  
591 abundance values (i.e. the relative amount (w/w) of each protein in respect to the sum over  
592 all detected proteins) were log<sub>2</sub>-transformed and normalized by subtraction of the median  
593 derived from all data points for the given protein. Significant changes in protein abundance  
594 were detected by moderated t-statistics essentially as described (96,97) across all technical  
595 replicates using an empirical Bayes approach and false discovery (FDR)-based correction for  
596 multiple comparisons (100). For this purpose, the Bioconductor R packages "limma" (101)  
597 and "q-value" (102) were used in RStudio, an integrated development environment for the  
598 open source programming language R. Proteins identified as contaminants (e.g. components  
599 of blood or hair cells) were removed from the analysis. Proteins with ppm values below 100  
600 which were not identified in one genotype were considered as just above detection level and  
601 also removed from the analysis. The relative abundance of a protein in myelin was accepted  
602 as altered if both statistically significant (q-value <0.05). Pie charts, heatmaps and volcano  
603 plots were prepared in Microsoft Excel 2013 and GraphPad Prism 7. Pearson's correlation  
604 coefficients derived from log<sub>2</sub>-transformed ppm abundance values were clustered and  
605 visualized with the tool heatmap.2 contained in the R package gplots ([CRAN.R-](http://CRAN.R-project.org/package=gplots)  
606 [project.org/package=gplots](http://project.org/package=gplots)). Only pairwise complete observations were considered to  
607 reduce the influence of missing values on clustering behavior. The mass spectrometry  
608 proteomics data have been deposited to the ProteomeXchange Consortium

609 ([proteomecentral.proteomexchange.org](http://proteomecentral.proteomexchange.org)) via the PRIDE partner repository (103) with the  
610 dataset identifier PXD015960.

611

### 612 **Gel electrophoresis and silver staining of gels**

613 Protein concentration was determined using the DC Protein Assay kit (BioRad). Samples  
614 were separated on a 12% SDS-PAGE for 1 h at 200 V using the BioRad system, fixated  
615 overnight in 10% [v/v] acetic acid and 40 % [v/v] ethanol and then washed in 30% ethanol (2x  
616 20 min) and ddH<sub>2</sub>O (1x 20 min). For sensitization, gels were incubated 1 min in 0.012% [v/v]  
617 Na<sub>2</sub>S<sub>2</sub>O<sub>3</sub> and subsequently washed with ddH<sub>2</sub>O (3x 20 sec). For silver staining, gels were  
618 impregnated for 20 min in 0.2 % [w/v] AgNO<sub>3</sub> / 0.04% formaldehyde, washed with ddH<sub>2</sub>O (3x  
619 20 sec) and developed in 3% [w/v] Na<sub>2</sub>CO<sub>3</sub> / 0.02% [w/v] formaldehyde. The reaction was  
620 stopped by exchanging the solution with 5% [v/v] acetic acid.

621

### 622 **Immunoblotting**

623 Immunoblotting was performed as described (104,105). Primary antibodies were specific for  
624 dystrophin-related-protein 2 (DRP2; Sigma; 1:1000), peripheral myelin protein 2 (PMP2;  
625 ProteinTech Group 12717-1-AP; 1:1000), proteolipid protein (PLP/DM20; A431 (106);  
626 1:5000), Monocarboxylate transporter 1 (MCT1/SLC16A1; (107); 1:1000), periaxin (PRX;  
627 (59); 1:1000), sodium/potassium-transporting ATPase subunit alpha-1 (ATP1A1; 1:2000;  
628 Abcam #13736-1-AP), myelin protein zero (MPZ/P0; (108); kind gift by J. Archelos-Garcia;  
629 1:10.000), voltage-dependent anion-selective channel protein (VDAC; Abcam #ab15895;  
630 1:1000), basigin (BSG/CD147; ProteinTech Group #ab64616; 1:1000), neurofilament H  
631 (NEFH/NF-H; Covance #SMI-32P; 1:1000), voltage-gated potassium channel subunit A  
632 member 1 (KCNA1; Neuromab #73-007; 1:1000), EGR2/KROX20 ((109); kind gift by D.  
633 Meijer, Edinburgh; 1:1000) and myelin basic protein (MBP; 1:2000). To generate the latter  
634 antisera, rabbits were immunized (Pineda Antikörper Service, Berlin, Germany) with the  
635 KLH-coupled peptide CQDENPVVHFFK corresponding to amino acids 212-222 of mouse  
636 MBP isoform 1 (Swisprot/Uniprot-identifier P04370-1). Anti-MBP antisera were purified by  
637 affinity chromatography and extensively tested for specificity by immunoblot analysis of  
638 homogenate of brains dissected from wild-type mice compared to *Mbp*<sup>shiverer/shiverer</sup> mice that  
639 lack expression of MBP. Appropriate secondary anti-mouse or -rabbit antibodies conjugated  
640 to HRP were from dianova. Immunoblots were developed using the Enhanced  
641 Chemiluminescence Detection kit (Western Lightning® Plus, Perkin Elmer) and detected with  
642 the Intas ChemoCam system (INTAS Science Imaging Instruments GmbH, Göttingen,  
643 Germany).

644

### 645 **Immunolabelling of teased fibers**

646 Teased fibers were prepared as previously described (9,110). For each genotype, one male  
647 mouse was sacrificed by cervical dislocation at P17. Immunolabelling of teased fibers was  
648 performed as described (69). Briefly, teased fibers were fixed for 5 min in 4%  
649 paraformaldehyde, permeabilized 5 min with ice-cold methanol, washed in PBS (3x 5 min)  
650 and blocked for 1 h at 21°C in blocking buffer (10% horse serum, 0.25% Triton X-100, 1%  
651 bovine serum albumin in PBS). Primary antibodies were applied overnight at 4°C in  
652 incubation buffer (1.5% horse serum, 0.25% Triton X-100 in PBS). Samples were washed in  
653 PBS (3x 5 min) and secondary antibodies were applied in incubation buffer (1 h, RT).  
654 Samples were again washed in PBS (2x 5 min), and 4',6-diamidino-2-phenylindole (DAPI;  
655 1:50 000 in PBS) was applied for 10 min at RT. Samples were briefly washed 2x with ddH<sub>2</sub>O  
656 and mounted using Aqua-Poly/Mount (Polysciences, Eppelheim, Germany). Antibodies were  
657 specific for myelin-associated glycoprotein (MAG clone 513; Chemicon MAB1567; 1:50) and  
658 MCT1/SLC16A1 (107). Secondary antibodies were donkey α-rabbit-Alexa488 (Invitrogen  
659 A21206; 1:1000) and donkey α-mouse-Alexa555 (Invitrogen A21202; 1:1000). Labeled  
660 teased fibers were imaged using the confocal microscope Leica SP5. The signal was  
661 collected with the objective HCX PL APO lambda blue 63.0.x1.20. DAPI staining was excited  
662 with 405 nm and collected between 417 nm - 480 nm. To excite the Alexa488 fluorophore an  
663 Argon laser with the excitation of 488 nm was used and the emission was set to 500 nm -  
664 560 nm. Alexa555 was excited by using the DPSS561 laser at an excitation of 561 nm and  
665 the emission was set to 573 nm - 630 nm. To export and process the images LAS AF lite and  
666 Adobe Photoshop were used.

667

### 668 **mRNA abundance profiles**

669 Raw data were previously established (60) from the sciatic nerves of wild type Sprague  
670 Dawley rats at the indicated ages (E21, P6, P18; n=4 per time point). Briefly, sciatic nerves  
671 were dissected, the epineurium was removed, total RNA was extracted with the RNeasy Kit  
672 (Qiagen), concentration and quality (ratio of absorption at 260/280 nm) of RNA samples were  
673 determined using the NanoDrop spectrophotometer (ThermoScientific), integrity of the  
674 extracted RNA was determined with the Agilent 2100 Bioanalyser (Agilent Technologies) and  
675 RNA-Seq was performed using the Illumina HiSeq2000 platform. RNA-Seq raw data are  
676 available under the GEO accession number GSE115930 (60). For the present analysis, the  
677 fastqfiles were mapped to *rattus norvegicus* m6 using Tophat Aligner and then quantified  
678 based on the Ensemble Transcripts release v96. The raw read counts were then normalized  
679 using the R package DESeq2. The normalized gene expression data was then standardized  
680 to a mean of zero and a standard deviation of one, therefore genes with similar changes in  
681 expression are close in the euclidian space. Clustering was performed on the standardized

682 data using the R package mfuzz. Transcripts displaying abundance differences of less than  
683 10% coefficient of variation were considered developmentally unchanged.

684

### 685 **Venn diagrams**

686 Area-proportional Venn diagrams were prepared using BioVenn (111) at [www.biovenn.nl/](http://www.biovenn.nl/).

687

### 688 **GO-term**

689 For functional categorization of the myelin proteome the associated gene ontology terms  
690 were systematically analyzed on the mRNA abundance cluster using the Database for  
691 Annotation, Visualization and Integrated Discovery (DAVID; <https://david.ncifcrf.gov>). For  
692 comparison known myelin proteins according to literature were added.

693

### 694 **Histological analysis**

695 *Prx*<sup>-/-</sup> and control mice were perfused at the indicated ages intravascularly with fixative  
696 solution (2.5% glutaraldehyde, 4% paraformaldehyde, 0.1 M sodium cacodylate buffer, pH  
697 7.4). Quadriceps nerves were removed, fixed for 2 h at room temperature, followed by 18 h  
698 at 4°C in the same fixative, postfixed in OsO<sub>4</sub>, dehydrated a graded series of ethanol,  
699 followed by propylene oxide and embedded in Araldite. All axons not associated with a  
700 Remak bundle were counted and categorized as myelinated or non-myelinated. All myelin  
701 profiles lacking a recognizable axon were counted. The total number of axons were counted  
702 on micrographs of toluidine blue stained Araldite sections (0.5 μm) of quadriceps nerves.  
703 Precise p-values for the quantitative comparison between Ctrl and *Prx*<sup>-/-</sup> mice were: Total  
704 number of axons (**Figure 6B**; Student's unpaired t-test): 2 mo p=0.01734; 4 mo p=2.1E-05; 9  
705 mo p=0.007625; Number of myelinated axons (**Figure 6C**; Student's unpaired t-test): 2 mo  
706 p=0.00444; 4 mo p=2.12E-05; 9 mo p=0.005766; Number of empty myelin profiles (**Figure**  
707 **6D**; Student's unpaired t-test): 2 mo p=0.004445; 4 mo p=0.001461; 9 mo p=0.000695;  
708 Axonal diameters (**Figure 6E-G**; two-sided Kolmogorow-Smirnow test): 2 mo p=2.20E-16; 4  
709 mo p=2.20E-16; 9 mo p=2.20E-16.

710

711



712 **ACKNOWLEDGMENTS**

713 We thank J. Archelos-Garcia and D. Meijer for antibodies, T. Buscham and J. Edgar for  
714 discussions, L. Piepkorn for support in data analysis, K.-A. Nave for support made possible  
715 by a European Research Council Advanced Grant ('MyeliNano' to K.-A.N.) and the  
716 International Max Planck Research School for Genome Science (IMPRS-GS) for supporting  
717 S.B.S..

718

719

720 **FUNDING**

721 Our work is supported by the Deutsche Forschungsgemeinschaft (DFG; Grants WE 2720/2-  
722 2, WE 2720/4-1 and WE 2720/5-1 to H.B.W. and RO 4076/3-2 to M.J.R.) and the Wellcome  
723 Trust (Grant No 0842424 to P.J.B.).

724

725

726 **CONFLICT OF INTEREST STATEMENT**

727 The authors declare no conflict of interest.

728

729

730

731 **REFERENCES**

732

- 733 1. Weil M-T, Heibeck S, Töpperwien M, tom Dieck S, Ruhwedel T, Salditt T, et al. Axonal  
734 Ensheathment in the Nervous System of Lamprey: Implications for the Evolution of Myelinating  
735 Glia. *J Neurosci* [Internet]. 2018 Jul 18;38(29):6586–96. Available from:  
736 <http://www.jneurosci.org/lookup/doi/10.1523/JNEUROSCI.1034-18.2018>
- 737 2. Hartline DK, Colman DR. Rapid Conduction and the Evolution of Giant Axons and Myelinated  
738 Fibers. *Curr Biol* [Internet]. 2007 Jan;17(1):R29–35. Available from:  
739 <https://linkinghub.elsevier.com/retrieve/pii/S0960982206025231>
- 740 3. Rossor AM, Polke JM, Houlden H, Reilly MM. Clinical implications of genetic advances in  
741 Charcot–Marie–Tooth disease. *Nat Rev Neurol* [Internet]. 2013 Oct 10;9(10):562–71. Available  
742 from: <http://www.nature.com/articles/nrneuro.2013.179>
- 743 4. Michailov G V. Axonal Neuregulin-1 Regulates Myelin Sheath Thickness. *Science* (80- )  
744 [Internet]. 2004 Apr 30;304(5671):700–3. Available from:  
745 <http://www.sciencemag.org/cgi/doi/10.1126/science.1095862>
- 746 5. Taveggia C, Zanazzi G, Petrylak A, Yano H, Rosenbluth J, Einheber S, et al. Neuregulin-1  
747 Type III Determines the Ensheathment Fate of Axons. *Neuron* [Internet]. 2005 Sep;47(5):681–  
748 94. Available from: <https://linkinghub.elsevier.com/retrieve/pii/S0896627305006926>
- 749 6. Chernousov MA, Yu W-M, Chen Z-L, Carey DJ, Strickland S. Regulation of Schwann cell  
750 function by the extracellular matrix. *Glia* [Internet]. 2008 Nov 1;56(14):1498–507. Available  
751 from: <http://doi.wiley.com/10.1002/glia.20740>
- 752 7. Petersen SC, Luo R, Liebscher I, Giera S, Jeong S-J, Mogha A, et al. The Adhesion GPCR  
753 GPR126 Has Distinct, Domain-Dependent Functions in Schwann Cell Development Mediated  
754 by Interaction with Laminin-211. *Neuron* [Internet]. 2015 Feb;85(4):755–69. Available from:  
755 <https://linkinghub.elsevier.com/retrieve/pii/S0896627314011660>
- 756 8. Ghidinelli M, Poitelon Y, Shin YK, Ameroso D, Williamson C, Ferri C, et al. Laminin 211 inhibits  
757 protein kinase A in Schwann cells to modulate neuregulin 1 type III-driven myelination. Emery  
758 B, editor. *PLOS Biol* [Internet]. 2017 Jun 21;15(6):e2001408. Available from:  
759 <https://dx.plos.org/10.1371/journal.pbio.2001408>
- 760 9. Sherman DL, Fabrizi C, Gillespie CS, Brophy PJ. Specific Disruption of a Schwann Cell  
761 Dystrophin-Related Protein Complex in a Demyelinating Neuropathy. *Neuron* [Internet]. 2001  
762 May;30(3):677–87. Available from:  
763 <https://linkinghub.elsevier.com/retrieve/pii/S0896627301003270>
- 764 10. Masaki T, Matsumura K, Hirata A, Yamada H, Hase A, Arai K, et al. Expression of  
765 Dystroglycan and the Laminin- $\alpha$ 2 Chain in the Rat Peripheral Nerve during Development. *Exp*  
766 *Neurol* [Internet]. 2002 Mar;174(1):109–17. Available from:  
767 <https://linkinghub.elsevier.com/retrieve/pii/S0014488601978562>
- 768 11. Nodari A, Previtali SC, Dati G, Occhi S, Court FA, Colombelli C, et al.  $\alpha$ 4 Integrin and  
769 Dystroglycan Cooperate to Stabilize the Myelin Sheath. *J Neurosci* [Internet]. 2008 Jun  
770 25;28(26):6714–9. Available from: [http://www.jneurosci.org/cgi/doi/10.1523/JNEUROSCI.0326-](http://www.jneurosci.org/cgi/doi/10.1523/JNEUROSCI.0326-08.2008)  
771 08.2008

- 772 12. Raasakka A, Linxweiler H, Brophy PJ, Sherman DL, Kursula P. Direct Binding of the Flexible  
773 C-Terminal Segment of Periaxin to  $\beta$ 4 Integrin Suggests a Molecular Basis for CMT4F. *Front*  
774 *Mol Neurosci* [Internet]. 2019 Apr 9;12. Available from:  
775 <https://www.frontiersin.org/article/10.3389/fnmol.2019.00084/full>
- 776 13. Hess A, Lansing AI. The fine structure of peripheral nerve fibers. *Anat Rec.* 1953;
- 777 14. Sherman DL, Brophy PJ. Mechanisms of axon ensheathment and myelin growth. *Nat Rev*  
778 *Neurosci* [Internet]. 2005 Sep;6(9):683–90. Available from:  
779 <http://www.nature.com/articles/nrn1743>
- 780 15. Pereira JA, Lebrun-Julien F, Suter U. Molecular mechanisms regulating myelination in the  
781 peripheral nervous system. *Trends Neurosci* [Internet]. 2012 Feb;35(2):123–34. Available from:  
782 <https://linkinghub.elsevier.com/retrieve/pii/S0166223611001937>
- 783 16. Grove M, Brophy PJ. FAK Is Required for Schwann Cell Spreading on Immature Basal Lamina  
784 to Coordinate the Radial Sorting of Peripheral Axons with Myelination. *J Neurosci* [Internet].  
785 2014 Oct 1;34(40):13422–34. Available from:  
786 <http://www.jneurosci.org/cgi/doi/10.1523/JNEUROSCI.1764-14.2014>
- 787 17. Monk KR, Feltri ML, Taveggia C. New insights on schwann cell development. *Glia* [Internet].  
788 2015 Aug;63(8):1376–93. Available from: <http://doi.wiley.com/10.1002/glia.22852>
- 789 18. Feltri ML, Poitelon Y, Previtali SC. How Schwann Cells Sort Axons. *Neurosci* [Internet]. 2016  
790 Jun 16;22(3):252–65. Available from:  
791 <http://journals.sagepub.com/doi/10.1177/1073858415572361>
- 792 19. Giese KP, Martini R, Lemke G, Soriano P, Schachner M. Mouse P0 gene disruption leads to  
793 hypomyelination, abnormal expression of recognition molecules, and degeneration of myelin  
794 and axons. *Cell* [Internet]. 1992 Nov;71(4):565–76. Available from:  
795 <https://linkinghub.elsevier.com/retrieve/pii/009286749290591Y>
- 796 20. Martini R, Mohajeri MH, Kasper S, Giese KP, Schachner M. Mice doubly deficient in the genes  
797 for P0 and myelin basic protein show that both proteins contribute to the formation of the major  
798 dense line in peripheral nerve myelin. *J Neurosci.* 1995;
- 799 21. Nawaz S, Schweitzer J, Jahn O, Werner HB. Molecular evolution of myelin basic protein, an  
800 abundant structural myelin component. *Glia* [Internet]. 2013 Aug;61(8):1364–77. Available  
801 from: <http://doi.wiley.com/10.1002/glia.22520>
- 802 22. Greenfield S, Brostoff S, Eylar EH, Morell P. PROTEIN COMPOSITION OF MYELIN OF THE  
803 PERIPHERAL NERVOUS SYSTEM. *J Neurochem* [Internet]. 1973 Apr;20(4):1207–16.  
804 Available from: <http://doi.wiley.com/10.1111/j.1471-4159.1973.tb00089.x>
- 805 23. Brostoff SW, Karkhanis YD, Carlo DJ, Reuter W, Eylar EH. Isolation and partial  
806 characterization of the major proteins of rabbit sciatic nerve myelin. *Brain Res* [Internet]. 1975  
807 Mar;86(3):449–58. Available from:  
808 <https://linkinghub.elsevier.com/retrieve/pii/0006899375908951>
- 809 24. Nave K-A, Werner HB. Myelination of the Nervous System: Mechanisms and Functions. *Annu*  
810 *Rev Cell Dev Biol* [Internet]. 2014 Oct 11;30(1):503–33. Available from:  
811 <http://www.annualreviews.org/doi/10.1146/annurev-cellbio-100913-013101>
- 812 25. Kleopa KA, Sargiannidou I. Connexins, gap junctions and peripheral neuropathy. *Neurosci Lett*

- 813 [Internet]. 2015 Jun;596:27–32. Available from:  
814 <https://linkinghub.elsevier.com/retrieve/pii/S0304394014008453>
- 815 26. Court FA, Sherman DL, Pratt T, Garry EM, Ribchester RR, Cottrell DF, et al. Restricted growth  
816 of Schwann cells lacking Cajal bands slows conduction in myelinated nerves. *Nature* [Internet].  
817 2004 Sep;431(7005):191–5. Available from: <http://www.nature.com/articles/nature02841>
- 818 27. Beirowski B, Babetto E, Golden JP, Chen Y-J, Yang K, Gross RW, et al. Metabolic regulator  
819 LKB1 is crucial for Schwann cell-mediated axon maintenance. *Nat Neurosci* [Internet]. 2014  
820 Oct 7;17(10):1351–61. Available from: <http://www.nature.com/articles/nn.3809>
- 821 28. Domenech-Estevez E, Baloui H, Repond C, Rosafio K, Medard J-J, Tricaud N, et al.  
822 Distribution of Monocarboxylate Transporters in the Peripheral Nervous System Suggests  
823 Putative Roles in Lactate Shuttling and Myelination. *J Neurosci* [Internet]. 2015 Mar  
824 11;35(10):4151–6. Available from: [http://www.jneurosci.org/cgi/doi/10.1523/JNEUROSCI.3534-](http://www.jneurosci.org/cgi/doi/10.1523/JNEUROSCI.3534-14.2015)  
825 14.2015
- 826 29. Kim S, Maynard JC, Sasaki Y, Strickland A, Sherman DL, Brophy PJ, et al. Schwann Cell O-  
827 GlcNAc Glycosylation Is Required for Myelin Maintenance and Axon Integrity. *J Neurosci*  
828 [Internet]. 2016 Sep 14;36(37):9633–46. Available from:  
829 <http://www.jneurosci.org/cgi/doi/10.1523/JNEUROSCI.1235-16.2016>
- 830 30. Gonçalves NP, Vægter CB, Andersen H, Østergaard L, Calcutt NA, Jensen TS. Schwann cell  
831 interactions with axons and microvessels in diabetic neuropathy. *Nat Rev Neurol* [Internet].  
832 2017 Mar 30;13(3):135–47. Available from: <http://www.nature.com/articles/nrneurol.2016.201>
- 833 31. Stassart RM, Möbius W, Nave K-A, Edgar JM. The Axon-Myelin Unit in Development and  
834 Degenerative Disease. *Front Neurosci* [Internet]. 2018 Jul 11;12. Available from:  
835 <https://www.frontiersin.org/article/10.3389/fnins.2018.00467/full>
- 836 32. Nagarajan R, Le N, Mahoney H, Araki T, Milbrandt J. Deciphering peripheral nerve myelination  
837 by using Schwann cell expression profiling. *Proc Natl Acad Sci* [Internet]. 2002 Jun  
838 25;99(13):8998–9003. Available from: <http://www.pnas.org/cgi/doi/10.1073/pnas.132080999>
- 839 33. Le N, Nagarajan R, Wang JYT, Araki T, Schmidt RE, Milbrandt J. Analysis of congenital  
840 hypomyelinating Egr2Lo/Lo nerves identifies Sox2 as an inhibitor of Schwann cell  
841 differentiation and myelination. *Proc Natl Acad Sci* [Internet]. 2005 Feb 15;102(7):2596–601.  
842 Available from: <http://www.pnas.org/cgi/doi/10.1073/pnas.0407836102>
- 843 34. Ryu EJ, Yang M, Gustin JA, Chang L-W, Freimuth RR, Nagarajan R, et al. Analysis of  
844 Peripheral Nerve Expression Profiles Identifies a Novel Myelin Glycoprotein, MP11. *J Neurosci*  
845 [Internet]. 2008 Jul 23;28(30):7563–73. Available from:  
846 <http://www.jneurosci.org/cgi/doi/10.1523/JNEUROSCI.1659-08.2008>
- 847 35. Zhang Y, Chen K, Sloan SA, Bennett ML, Scholze AR, O’Keeffe S, et al. An RNA-Sequencing  
848 Transcriptome and Splicing Database of Glia, Neurons, and Vascular Cells of the Cerebral  
849 Cortex. *J Neurosci* [Internet]. 2014 Sep 3;34(36):11929–47. Available from:  
850 <http://www.jneurosci.org/cgi/doi/10.1523/JNEUROSCI.1860-14.2014>
- 851 36. Patzig J, Erwig MS, Tenzer S, Kusch K, Dibaj P, Möbius W, et al. Septin/anillin filaments  
852 scaffold central nervous system myelin to accelerate nerve conduction. *Elife*. 2016;5:e17119.
- 853 37. Sharma K, Schmitt S, Bergner CG, Tyanova S, Kannaiyan N, Manrique-Hoyos N, et al. Cell

- 854 type- and brain region-resolved mouse brain proteome. *Nat Neurosci* [Internet]. 2015 Dec  
855 2;18(12):1819–31. Available from: <http://www.nature.com/articles/nn.4160>
- 856 38. Thakurela S, Garding A, Jung RB, Müller C, Goebbels S, White R, et al. The transcriptome of  
857 mouse central nervous system myelin. *Sci Rep* [Internet]. 2016 May 13;6(1):25828. Available  
858 from: <http://www.nature.com/articles/srep25828>
- 859 39. Marques S, Zeisel A, Codeluppi S, van Bruggen D, Mendanha Falcao A, Xiao L, et al.  
860 Oligodendrocyte heterogeneity in the mouse juvenile and adult central nervous system.  
861 *Science* (80- ) [Internet]. 2016 Jun 10;352(6291):1326–9. Available from:  
862 <http://www.sciencemag.org/cgi/doi/10.1126/science.aaf6463>
- 863 40. De Monasterio-Schrader P, Jahn O, Tenzer S, Wichert SP, Patzig J, Werner HB. Systematic  
864 approaches to central nervous system myelin. *Cellular and Molecular Life Sciences*. 2012.
- 865 41. Patzig J, Jahn O, Tenzer S, Wichert SP, de Monasterio-Schrader P, Rosfa S, et al.  
866 Quantitative and Integrative Proteome Analysis of Peripheral Nerve Myelin Identifies Novel  
867 Myelin Proteins and Candidate Neuropathy Loci. *J Neurosci* [Internet]. 2011 Nov  
868 9;31(45):16369–86. Available from:  
869 <http://www.jneurosci.org/cgi/doi/10.1523/JNEUROSCI.4016-11.2011>
- 870 42. Kangas SM, Ohlmeier S, Sormunen R, Jouhilahti E-M, Peltonen S, Peltonen J, et al. An  
871 approach to comprehensive genome and proteome expression analyses in Schwann cells and  
872 neurons during peripheral nerve myelin formation. *J Neurochem* [Internet]. 2016  
873 Sep;138(6):830–44. Available from: <http://doi.wiley.com/10.1111/jnc.13722>
- 874 43. Kusch K, Uecker M, Liepold T, Möbius W, Hoffmann C, Neumann H, et al. Partial  
875 Immunoblotting of 2D-Gels: A Novel Method to Identify Post-Translationally Modified Proteins  
876 Exemplified for the Myelin Acetylome. *Proteomes* [Internet]. 2017 Jan 12;5(4):3. Available  
877 from: <http://www.mdpi.com/2227-7382/5/1/3>
- 878 44. Neilson KA, Ali NA, Muralidharan S, Mirzaei M, Mariani M, Assadourian G, et al. Less label,  
879 more free: Approaches in label-free quantitative mass spectrometry. *Proteomics*. 2011.
- 880 45. Distler U, Kuharev J, Tenzer S. Biomedical applications of ion mobility-enhanced data-  
881 independent acquisition-based label-free quantitative proteomics. *Expert Rev Proteomics*.  
882 2014;
- 883 46. Geromanos SJ, Vissers JPC, Silva JC, Dorschel CA, Li GZ, Gorenstein M V., et al. The  
884 detection, correlation, and comparison of peptide precursor and product ions from data  
885 independent LC-MS with data dependant LC-MS/MS. *Proteomics*. 2009;
- 886 47. Li GZ, Vissers JPC, Silva JC, Golick D, Gorenstein M V., Geromanos SJ. Database searching  
887 and accounting of multiplexed precursor and product ion spectra from the data independent  
888 analysis of simple and complex peptide mixtures. *Proteomics*. 2009;
- 889 48. Distler U, Kuharev J, Navarro P, Tenzer S. Label-free quantification in ion mobility-enhanced  
890 data-independent acquisition proteomics. *Nat Protoc* [Internet]. 2016 Apr 24;11(4):795–812.  
891 Available from: <http://www.nature.com/articles/nprot.2016.042>
- 892 49. Distler U, Kuharev J, Navarro P, Levin Y, Schild H, Tenzer S. Drift time-specific collision  
893 energies enable deep-coverage data-independent acquisition proteomics. *Nat Methods*  
894 [Internet]. 2014 Feb 15;11(2):167–70. Available from:

- 895 <http://www.nature.com/articles/nmeth.2767>
- 896 50. Larocca JN, Norton WT. Isolation of Myelin. *Curr Protoc Cell Biol* [Internet]. 2006  
897 Dec;33(1):3.25.1-3.25.19. Available from: <http://doi.wiley.com/10.1002/0471143030.cb0325s33>
- 898 51. Jahn O, Tenzer S, Werner HB. Myelin proteomics: Molecular anatomy of an insulating sheath.  
899 *Molecular Neurobiology*. 2009.
- 900 52. Erwig MS, Hesse D, Jung RB, Uecker M, Kusch K, Tenzer S, et al. Myelin: Methods for  
901 Purification and Proteome Analysis. In: *Methods in Molecular Biology* [Internet]. 2019. p. 37–  
902 63. Available from: [http://link.springer.com/10.1007/978-1-4939-9072-6\\_3](http://link.springer.com/10.1007/978-1-4939-9072-6_3)
- 903 53. Silva JC, Gorenstein M V., Li G-Z, Vissers JPC, Geromanos SJ. Absolute Quantification of  
904 Proteins by LCMS E. *Mol Cell Proteomics* [Internet]. 2006 Jan;5(1):144–56. Available from:  
905 <http://www.mcponline.org/lookup/doi/10.1074/mcp.M500230-MCP200>
- 906 54. Ahrné E, Molzahn L, Glatter T, Schmidt A. Critical assessment of proteome-wide label-free  
907 absolute abundance estimation strategies. *Proteomics*. 2013;
- 908 55. Dodds JN, Baker ES. Ion Mobility Spectrometry: Fundamental Concepts, Instrumentation,  
909 Applications, and the Road Ahead. *J Am Soc Mass Spectrom*. 2019;
- 910 56. Micko S, Schlaepfer WW. PROTEIN COMPOSITION OF AXONS and MYELIN FROM RAT  
911 and HUMAN PERIPHERAL NERVES. *J Neurochem* [Internet]. 1978 May;30(5):1041–9.  
912 Available from: <http://doi.wiley.com/10.1111/j.1471-4159.1978.tb12397.x>
- 913 57. Smith ME, Curtis BM. FROG SCIATIC NERVE MYELIN: A CHEMICAL CHARACTERIZATION.  
914 *J Neurochem* [Internet]. 1979 Aug;33(2):447–52. Available from:  
915 <http://doi.wiley.com/10.1111/j.1471-4159.1979.tb05174.x>
- 916 58. Whitaker JN. The protein antigens of peripheral nerve myelin. *Ann Neurol* [Internet].  
917 1981;9(S1):56–64. Available from: <http://doi.wiley.com/10.1002/ana.410090710>
- 918 59. Gillespie CS, Sherman DL, Blair GE, Brophy PJ. Periaxin, a novel protein of myelinating  
919 schwann cells with a possible role in axonal ensheathment. *Neuron* [Internet]. 1994  
920 Mar;12(3):497–508. Available from:  
921 <https://linkinghub.elsevier.com/retrieve/pii/0896627394902089>
- 922 60. Fledrich R, Abdelaal T, Rasch L, Bansal V, Schütza V, Brügger B, et al. Targeting myelin lipid  
923 metabolism as a potential therapeutic strategy in a model of CMT1A neuropathy. *Nat Commun*  
924 [Internet]. 2018 Dec 2;9(1):3025. Available from: [http://www.nature.com/articles/s41467-018-](http://www.nature.com/articles/s41467-018-05420-0)  
925 [05420-0](http://www.nature.com/articles/s41467-018-05420-0)
- 926 61. Pareyson D, Marchesi C. Diagnosis, natural history, and management of Charcot–Marie–Tooth  
927 disease. *Lancet Neurol* [Internet]. 2009 Jul;8(7):654–67. Available from:  
928 <https://linkinghub.elsevier.com/retrieve/pii/S1474442209701103>
- 929 62. Baets J, De Jonghe P, Timmerman V. Recent advances in Charcot–Marie–Tooth disease. *Curr*  
930 *Opin Neurol* [Internet]. 2014 Oct;27(5):532–40. Available from:  
931 [http://content.wkhealth.com/linkback/openurl?sid=WKPTLP:landingpage&an=00019052-](http://content.wkhealth.com/linkback/openurl?sid=WKPTLP:landingpage&an=00019052-201410000-00006)  
932 [201410000-00006](http://content.wkhealth.com/linkback/openurl?sid=WKPTLP:landingpage&an=00019052-201410000-00006)
- 933 63. Brennan KM, Bai Y, Shy ME. Demyelinating CMT—what’s known, what’s new and what’s in  
934 store? *Neurosci Lett* [Internet]. 2015 Jun;596:14–26. Available from:  
935 <https://linkinghub.elsevier.com/retrieve/pii/S0304394015000725>

- 936 64. Gillespie CS, Sherman DL, Fleetwood-Walker SM, Cottrell DF, Tait S, Garry EM, et al.  
937 Peripheral Demyelination and Neuropathic Pain Behavior in Periaxin-Deficient Mice. *Neuron*  
938 [Internet]. 2000 May;26(2):523–31. Available from:  
939 <https://linkinghub.elsevier.com/retrieve/pii/S0896627300811848>
- 940 65. Guilbot A. A mutation in periaxin is responsible for CMT4F, an autosomal recessive form of  
941 Charcot-Marie-Tooth disease. *Hum Mol Genet* [Internet]. 2001 Feb 1;10(4):415–21. Available  
942 from: <https://academic.oup.com/hmg/article-lookup/doi/10.1093/hmg/10.4.415>
- 943 66. Berger P, Niemann A, Suter U. Schwann cells and the pathogenesis of inherited motor and  
944 sensory neuropathies (Charcot-Marie-Tooth disease). *Glia* [Internet]. 2006 Sep;54(4):243–57.  
945 Available from: <http://doi.wiley.com/10.1002/glia.20386>
- 946 67. Marchesi C, Milani M, Morbin M, Cesani M, Lauria G, Scaioli V, et al. Four novel cases of  
947 periaxin-related neuropathy and review of the literature. *Neurology* [Internet]. 2010 Nov  
948 16;75(20):1830–8. Available from:  
949 <http://www.neurology.org/cgi/doi/10.1212/WNL.0b013e3181fd6314>
- 950 68. Philp NJ, Ochrietor JD, Rudoy C, Muramatsu T, Linser PJ. Loss of MCT1, MCT3, and MCT4  
951 Expression in the Retinal Pigment Epithelium and Neural Retina of the 5A11/Basigin-Null  
952 Mouse. *Investig Ophthalmology Vis Sci* [Internet]. 2003 Mar 1;44(3):1305. Available from:  
953 <http://iovs.arvojournals.org/article.aspx?doi=10.1167/iovs.02-0552>
- 954 69. Patzig J, Kusch K, Fledrich R, Eichel MA, Lüders KA, Möbius W, et al. Proteolipid protein  
955 modulates preservation of peripheral axons and premature death when myelin protein zero is  
956 lacking. *Glia* [Internet]. 2016 Jan;64(1):155–74. Available from:  
957 <http://doi.wiley.com/10.1002/glia.22922>
- 958 70. Lee Y, Morrison BM, Li Y, Lengacher S, Farah MH, Hoffman PN, et al. Oligodendroglia  
959 metabolically support axons and contribute to neurodegeneration. *Nature* [Internet]. 2012 Jul  
960 11;487(7408):443–8. Available from: <http://www.nature.com/articles/nature11314>
- 961 71. Fünfschilling U, Supplie LM, Mahad D, Boretius S, Saab AS, Edgar J, et al. Glycolytic  
962 oligodendrocytes maintain myelin and long-term axonal integrity. *Nature* [Internet]. 2012 May  
963 29;485(7399):517–21. Available from: <http://www.nature.com/articles/nature11007>
- 964 72. Morrison BM, Tsingalia A, Vidensky S, Lee Y, Jin L, Farah MH, et al. Deficiency in  
965 monocarboxylate transporter 1 (MCT1) in mice delays regeneration of peripheral nerves  
966 following sciatic nerve crush. *Exp Neurol* [Internet]. 2015 Jan;263:325–38. Available from:  
967 <https://linkinghub.elsevier.com/retrieve/pii/S0014488614003549>
- 968 73. Morrison BM, Lee Y, Rothstein JD. Oligodendroglia: Metabolic supporters of axons. *Trends in*  
969 *Cell Biology*. 2013.
- 970 74. Saab AS, Tzvetanova ID, Nave K-A. The role of myelin and oligodendrocytes in axonal energy  
971 metabolism. *Curr Opin Neurobiol* [Internet]. 2013 Dec;23(6):1065–72. Available from:  
972 <https://linkinghub.elsevier.com/retrieve/pii/S0959438813001888>
- 973 75. Rinholm JE, Bergersen LH. White matter lactate – Does it matter? *Neuroscience* [Internet].  
974 2014 Sep;276:109–16. Available from:  
975 <https://linkinghub.elsevier.com/retrieve/pii/S0306452213008464>
- 976 76. Jha MK, Lee Y, Russell KA, Yang F, Dastgheyb RM, Deme P, et al. Monocarboxylate

- 977 transporter 1 in Schwann cells contributes to maintenance of sensory nerve myelination during  
978 aging. *Glia*. 2019;
- 979 77. Edgar JM, McLaughlin M, Werner HB, McCulloch MC, Barrie JA, Brown A, et al. Early  
980 ultrastructural defects of axons and axon-glia junctions in mice lacking expression of *Cnp1*.  
981 *Glia*. 2009;
- 982 78. Verheijen MHG. Local regulation of fat metabolism in peripheral nerves. *Genes Dev* [Internet].  
983 2003 Oct 1;17(19):2450–64. Available from:  
984 <http://www.genesdev.org/cgi/doi/10.1101/gad.1116203>
- 985 79. Buchstaller J. Efficient Isolation and Gene Expression Profiling of Small Numbers of Neural  
986 Crest Stem Cells and Developing Schwann Cells. *J Neurosci* [Internet]. 2004 Mar  
987 10;24(10):2357–65. Available from:  
988 <http://www.jneurosci.org/cgi/doi/10.1523/JNEUROSCI.4083-03.2004>
- 989 80. D'antonio M, Michalovich D, Paterson M, Droggiti A, Woodhoo A, Mirsky R, et al. Gene  
990 profiling and bioinformatic analysis of Schwann cell embryonic development and myelination.  
991 *Glia* [Internet]. 2006 Apr 1;53(5):501–15. Available from:  
992 <http://doi.wiley.com/10.1002/glia.20309>
- 993 81. Schaeren-Wiemers N, Bonnet A, Erb M, Erne B, Bartsch U, Kern F, et al. The raft-associated  
994 protein MAL is required for maintenance of proper axon–glia interactions in the central nervous  
995 system. *J Cell Biol* [Internet]. 2004 Aug 30;166(5):731–42. Available from:  
996 <http://www.jcb.org/lookup/doi/10.1083/jcb.200406092>
- 997 82. Adlkofer K, Martini R, Aguzzi A, Zielasek J, Toyka K V., Suter U. Hypermyelination and  
998 demyelinating peripheral neuropathy in *Pmp22*-deficient mice. *Nat Genet* [Internet]. 1995  
999 Nov;11(3):274–80. Available from: <http://www.nature.com/articles/ng1195-274>
- 1000 83. Riethmacher D, Sonnenberg-Riethmacher E, Brinkmann V, Yamaai T, Lewin GR, Birchmeier  
1001 C. Severe neuropathies in mice with targeted mutations in the ErbB3 receptor. *Nature*  
1002 [Internet]. 1997 Oct;389(6652):725–30. Available from: <http://www.nature.com/articles/39593>
- 1003 84. Woldeyesus MT, Britsch S, Riethmacher D, Xu L, Sonnenberg-Riethmacher E, Abou-Rebyeh  
1004 F, et al. Peripheral nervous system defects in *erbB2* mutants following genetic rescue of heart  
1005 development. *Genes Dev* [Internet]. 1999 Oct 1;13(19):2538–48. Available from:  
1006 <http://www.genesdev.org/cgi/doi/10.1101/gad.13.19.2538>
- 1007 85. Ackerman SD, Luo R, Poitelon Y, Mogha A, Harty BL, D'Rozario M, et al. GPR56/ADGRG1  
1008 regulates development and maintenance of peripheral myelin. *J Exp Med* [Internet]. 2018 Mar  
1009 5;215(3):941–61. Available from: <http://www.jem.org/lookup/doi/10.1084/jem.20161714>
- 1010 86. Monk KR, Oshima K, Jors S, Heller S, Talbot WS. Gpr126 is essential for peripheral nerve  
1011 development and myelination in mammals. *Development* [Internet]. 2011 Jul 1;138(13):2673–  
1012 80. Available from: <http://dev.biologists.org/cgi/doi/10.1242/dev.062224>
- 1013 87. Monk KR, Naylor SG, Glenn TD, Mercurio S, Perlin JR, Dominguez C, et al. A G Protein-  
1014 Coupled Receptor Is Essential for Schwann Cells to Initiate Myelination. *Science* (80- )  
1015 [Internet]. 2009 Sep 11;325(5946):1402–5. Available from:  
1016 <http://www.sciencemag.org/cgi/doi/10.1126/science.1173474>
- 1017 88. Kabzinska D, Drac H, Sherman DL, Kostera-Pruszczyk A, Brophy PJ, Kochanski A, et al.



- 1018 Charcot-Marie-Tooth type 4F disease caused by S399fsx410 mutation in the PRX gene.  
1019 Neurology [Internet]. 2006 Mar 14;66(5):745–7. Available from:  
1020 <http://www.neurology.org/cgi/doi/10.1212/01.wnl.0000201269.46071.35>
- 1021 89. Baránková L, Šišková D, Hühne K, Vyháňalová E, Sakmaryová I, Bojar M, et al. A 71-  
1022 nucleotide deletion in the periaxin gene in a Romani patient with early-onset slowly progressive  
1023 demyelinating CMT. Eur J Neurol [Internet]. 2008 Jun;15(6):548–51. Available from:  
1024 <http://doi.wiley.com/10.1111/j.1468-1331.2008.02104.x>
- 1025 90. Tokunaga S, Hashiguchi A, Yoshimura A, Maeda K, Suzuki T, Haruki H, et al. Late-onset  
1026 Charcot-Marie-Tooth disease 4F caused by periaxin gene mutation. Neurogenetics [Internet].  
1027 2012 Nov 1;13(4):359–65. Available from: <http://link.springer.com/10.1007/s10048-012-0338-5>
- 1028 91. Gallardo E, García A, Ramón C, Maraví E, Infante J, Gastón I, et al. Charcot-Marie-Tooth  
1029 disease type 2J with MPZ Thr124Met mutation: clinico-electrophysiological and MRI study of a  
1030 family. J Neurol [Internet]. 2009 Dec 22;256(12):2061–71. Available from:  
1031 <http://link.springer.com/10.1007/s00415-009-5251-y>
- 1032 92. Leal A, Berghoff C, Berghoff M, Rojas-Araya M, Ortiz C, Heuss D, et al. A Costa Rican family  
1033 affected with Charcot-Marie-Tooth disease due to the myelin protein zero (MPZ) p.Thr124Met  
1034 mutation shares the Belgian haplotype. Rev Biol Trop [Internet]. 2014 Dec 1;62(4):1285.  
1035 Available from: <http://revistas.ucr.ac.cr/index.php/rbt/article/view/13473>
- 1036 93. Tokuda N, Noto Y, Kitani-Morii F, Hamano A, Kasai T, Shiga K, et al. Parasympathetic  
1037 Dominant Autonomic Dysfunction in Charcot-Marie-Tooth Disease Type 2J with the *MPZ*  
1038 Thr124Met Mutation. Intern Med [Internet]. 2015;54(15):1919–22. Available from:  
1039 [https://www.jstage.jst.go.jp/article/internalmedicine/54/15/54\\_54.4259/\\_article](https://www.jstage.jst.go.jp/article/internalmedicine/54/15/54_54.4259/_article)
- 1040 94. Duan X, Gu W, Hao Y, Wang R, Wen H, Sun S, et al. A Novel Asp121Asn Mutation of Myelin  
1041 Protein Zero Is Associated with Late-Onset Axonal Charcot-Marie-Tooth Disease, Hearing  
1042 Loss and Pupil Abnormalities. Front Aging Neurosci [Internet]. 2016 Sep 22;8. Available from:  
1043 <http://journal.frontiersin.org/Article/10.3389/fnagi.2016.00222/abstract>
- 1044 95. Fabrizi GM, Tamburin S, Cavallaro T, Cabrini I, Ferrarini M, Taioli F, et al. The spectrum of  
1045 Charcot-Marie-Tooth disease due to myelin protein zero: An electrodiagnostic, nerve  
1046 ultrasound and histological study. Clin Neurophysiol [Internet]. 2018 Jan;129(1):21–32.  
1047 Available from: <https://linkinghub.elsevier.com/retrieve/pii/S1388245717310854>
- 1048 96. Ambrozkiwicz MC, Schwark M, Kishimoto-Suga M, Borisova E, Hori K, Salazar-Lázaro A, et  
1049 al. Polarity Acquisition in Cortical Neurons Is Driven by Synergistic Action of Sox9-Regulated  
1050 Wwp1 and Wwp2 E3 Ubiquitin Ligases and Intronic miR-140. Neuron [Internet]. 2018  
1051 Dec;100(5):1097-1115.e15. Available from:  
1052 <https://linkinghub.elsevier.com/retrieve/pii/S0896627318308961>
- 1053 97. Erwig MS, Patzig J, Steyer AM, Dibaj P, Heilmann M, Heilmann I, et al. Anillin facilitates septin  
1054 assembly to prevent pathological unfoldings of central nervous system myelin. Elife [Internet].  
1055 2019 Jan 23;8. Available from: <https://elifesciences.org/articles/43888>
- 1056 98. Kuharev J, Navarro P, Distler U, Jahn O, Tenzer S. In-depth evaluation of software tools for  
1057 data-independent acquisition based label-free quantification. Proteomics [Internet]. 2015  
1058 Sep;15(18):3140–51. Available from: <http://doi.wiley.com/10.1002/pmic.201400396>

- 1059 99. Silva JC, Denny R, Dorschel C, Gorenstein M V., Li G-Z, Richardson K, et al. Simultaneous  
1060 Qualitative and Quantitative Analysis of the Escherichia coli Proteome. *Mol Cell Proteomics*  
1061 [Internet]. 2006 Apr;5(4):589–607. Available from:  
1062 <http://www.mcponline.org/lookup/doi/10.1074/mcp.M500321-MCP200>
- 1063 100. Kammers K, Cole RN, Tiengwe C, Ruczinski I. Detecting significant changes in protein  
1064 abundance. *EuPA Open Proteomics* [Internet]. 2015 Jun;7:11–9. Available from:  
1065 <https://linkinghub.elsevier.com/retrieve/pii/S2212968515000069>
- 1066 101. Ritchie ME, Phipson B, Wu D, Hu Y, Law CW, Shi W, et al. limma powers differential  
1067 expression analyses for RNA-sequencing and microarray studies. *Nucleic Acids Res* [Internet].  
1068 2015 Apr 20;43(7):e47–e47. Available from:  
1069 [http://academic.oup.com/nar/article/43/7/e47/2414268/limma-powers-differential-expression-](http://academic.oup.com/nar/article/43/7/e47/2414268/limma-powers-differential-expression-analyses-for)  
1070 [analyses-for](http://academic.oup.com/nar/article/43/7/e47/2414268/limma-powers-differential-expression-analyses-for)
- 1071 102. Storey JD. The positive false discovery rate: a Bayesian interpretation and the  $q$ -value. *Ann*  
1072 *Stat* [Internet]. 2003 Dec;31(6):2013–35. Available from:  
1073 <http://projecteuclid.org/euclid.aos/1074290335>
- 1074 103. Vizcaíno JA, Csordas A, Del-Toro N, Dianes JA, Griss J, Lavidas I, et al. 2016 update of the  
1075 PRIDE database and its related tools. *Nucleic Acids Res* [Internet]. 2016 Jan 4;44(D1):D447–  
1076 56. Available from: <https://academic.oup.com/nar/article-lookup/doi/10.1093/nar/gkv1145>
- 1077 104. Schardt A, Brinkmann BG, Mitkovski M, Sereda MW, Werner HB, Nave K-A. The SNARE  
1078 protein SNAP-29 interacts with the GTPase Rab3A: Implications for membrane trafficking in  
1079 myelinating glia. *J Neurosci Res* [Internet]. 2009 Nov 15;87(15):3465–79. Available from:  
1080 <http://doi.wiley.com/10.1002/jnr.22005>
- 1081 105. de Monasterio-Schrader P, Patzig J, Möbius W, Barrette B, Wagner TL, Kusch K, et al.  
1082 Uncoupling of neuroinflammation from axonal degeneration in mice lacking the myelin protein  
1083 tetraspanin-2. *Glia*. 2013;
- 1084 106. Jung M, Sommer I, Schachner M, Nave KA. Monoclonal antibody O10 defines a  
1085 conformationally sensitive cell- surface epitope of proteolipid protein (PLP): Evidence that PLP  
1086 misfolding underlies dysmyelination in mutant mice. *J Neurosci*. 1996;16(24):7920–9.
- 1087 107. Stumpf SK, Berghoff SA, Trevisiol A, Spieth L, Düking T, Schneider L V., et al. Ketogenic diet  
1088 ameliorates axonal defects and promotes myelination in Pelizaeus–Merzbacher disease. *Acta*  
1089 *Neuropathol* [Internet]. 2019 Jul 27;138(1):147–61. Available from:  
1090 <http://link.springer.com/10.1007/s00401-019-01985-2>
- 1091 108. Archelos JJ, Roggenbuck K, Scheider-Schaulies J, Lington C, Toyka K V., Hartung H-P.  
1092 Production and characterization of monoclonal antibodies to the extracellular domain of P0. *J*  
1093 *Neurosci Res* [Internet]. 1993 May 1;35(1):46–53. Available from:  
1094 <http://doi.wiley.com/10.1002/jnr.490350107>
- 1095 109. Darbas A, Jaegle M, Walbeehm E, van den Burg H, Driegen S, Broos L, et al. Cell autonomy of  
1096 the mouse claw paw mutation. *Dev Biol* [Internet]. 2004 Aug;272(2):470–82. Available from:  
1097 <https://linkinghub.elsevier.com/retrieve/pii/S0012160604003616>
- 1098 110. Catenaccio A, Court FA. Teased Fiber Preparation of Myelinated Nerve Fibers from Peripheral  
1099 Nerves for Vital Dye Staining and Immunofluorescence Analysis. In: *Methods in Molecular*

1100 Biology [Internet]. 2018. p. 329–37. Available from: <http://link.springer.com/10.1007/978-1->  
1101 [4939-7649-2\\_21](http://link.springer.com/10.1007/978-1-4939-7649-2_21)  
1102 111. Hulsen T, de Vlieg J, Alkema W. BioVenn – a web application for the comparison and  
1103 visualization of biological lists using area-proportional Venn diagrams. BMC Genomics  
1104 [Internet]. 2008;9(1):488. Available from:  
1105 <http://bmcbgenomics.biomedcentral.com/articles/10.1186/1471-2164-9-488>  
1106  
1107

1108 **FIGURE LEGENDS**

1109

1110

1111 **Figure 1. Proteome analysis of peripheral myelin**

1112 **(A)** Schematic illustration of a previous approach to the peripheral myelin proteome (41)  
1113 compared with the present workflow. Note that the current workflow allows largely automated  
1114 sample processing and omits labor-intense 2-dimensional differential gel-electrophoresis,  
1115 thereby considerably reducing hands-on time. Nano LC-MS analysis by data-independent  
1116 acquisition (DIA) using three different data acquisition modes provides efficient identification  
1117 and quantification of abundant myelin proteins ( $MS^E$ ; see **Figure 2**), a comprehensive  
1118 inventory (UDMS<sup>E</sup>; see **Figures 3-4**) and gel-free differential analysis of hundreds of distinct  
1119 proteins (DRE-UDMS<sup>E</sup>; see **Figure 5**). Samples were analyzed in three biological replicates.

1120 **(B)** Immunoblot of myelin biochemically enriched from sciatic nerves of wild-type mice at  
1121 postnatal day 21 (P21). Equal amounts of corresponding nerve lysate were loaded to  
1122 compare the abundance of marker proteins for compact myelin (MPZ/P0, MBP, PMP2), non-  
1123 compact myelin (PRX), the Schwann cell nucleus (KROX20/EGR2), axons (NEFH, KCNA1)  
1124 and mitochondria (VDAC). Blots show n=2 biological replicates representative of n=3  
1125 biological replicates. Note that myelin markers are enriched in purified myelin; other cellular  
1126 markers are reduced.

1127 **(C)** Number and relative abundance of proteins identified in myelin purified from the sciatic  
1128 nerves of wild-type mice using three different data acquisition modes ( $MS^E$ , UDMS<sup>E</sup>, DRE-  
1129 UDMS<sup>E</sup>). Note that  $MS^E$  (orange) provides the best information about the relative abundance  
1130 of high-abundant myelin proteins (dynamic range of more than four orders of magnitude) but  
1131 identifies comparatively fewer proteins in purified myelin. UDMS<sup>E</sup> (blue) identifies the largest  
1132 number of proteins but provides only a lower dynamic range of about three orders of  
1133 magnitude. DRE-UDMS<sup>E</sup> (green) identifies an intermediate number of proteins with an  
1134 intermediate dynamic range of about four orders of magnitude. Note that  $MS^E$  with very high  
1135 dynamic range is required for the quantification of the exceptionally abundant myelin protein  
1136 zero (MPZ/P0), myelin basic protein (MBP) and periaxin (PRX). ppm, parts per million.

1137 **(D)** Venn diagram comparing the number of proteins identified in PNS myelin by  $MS^E$ ,  
1138 UDMS<sup>E</sup> and DRE-UDMS<sup>E</sup>. Note the high overlap of identified proteins.

1139 **(E)** Venn diagram of the proteins identified in PNS myelin by UDMS<sup>E</sup> in this study compared  
1140 with those identified in two previous approaches (41,42).

1141

1142

1143 **Figure 1-supplement 1. Clustered heatmap of Pearson's correlation coefficients for**  
1144 **protein abundance comparing data acquisition modes.**

1145 The heatmap compares the  $\log_2$  transformed ppm protein abundance values to assess  
1146 peripheral myelin purified from wild type mice using three data acquisition modes ( $MS^E$ ,  
1147  $UDMS^E$ ,  $DRE-UDMS^E$ ). The inset shows the color key and the histogram for the values of the  
1148 correlation coefficients. Note that the runs cluster with a high overall correlation ( $>0.75$ ) into  
1149 three conditions defined by the acquisition mode, in agreement with the experimental design.  
1150 Among the samples analyzed by different acquisition modes,  $DRE-UDMS^E$  similarly  
1151 correlates with both  $MS^E$  and  $UDMS^E$ , reflecting its intermediate nature.

1152

1153

#### 1154 **Figure 2. Relative abundance of peripheral myelin proteins**

1155  $MS^E$  was used to identify and quantify proteins in myelin purified from the sciatic nerves of  
1156 wild-type mice at P21; their relative abundance is given as percent with relative standard  
1157 deviation (% +/- RSD). Note that known myelin proteins constitute  $>80\%$  of the total myelin  
1158 protein; proteins not previously associated with myelin constitute  $<20\%$ . Mass spectrometric  
1159 quantification based on 3 biological replicates per genotype with 4 technical replicates each  
1160 (see **Figure 1-source data 1**).

1161

1162

#### 1163 **Figure 3. Developmental mRNA abundance profiles of myelin-associated genes**

1164 **(A)** K-means clustering was performed for the mRNA profiles of those 1046 proteins in our  
1165 myelin proteome inventory for which significant mRNA expression was found by RNA-Seq in  
1166 the sciatic nerve of rats dissected at ages E21, P6, P18 and 6 months (M6). Note that this  
1167 filtering strategy allows to selectively display the developmental abundance profiles of those  
1168 transcripts that encode myelin-associated proteins rather than of all transcripts present in the  
1169 nerve. Standardized mRNA abundance profiles are shown (n=4 biological replicates per  
1170 age). Known myelin genes are displayed in red. For comparison, *Pmp22* mRNA was  
1171 included although the small tetraspan protein PMP22 was not mass spectrometrically  
1172 identified due to its unfavorable distribution of tryptic cleavage sites. Normalized counts for all  
1173 mRNAs including those displaying developmentally unchanged abundance are provided in  
1174 **Figure 3-Source data 1**.

1175 **(B)** Numbers of mRNAs per cluster.

1176

1177

#### 1178 **Figure 4. Categorization of annotated protein functions**

1179 All proteins identified in peripheral myelin by  $UDMS^E$  (turquoise) and the respective  
1180 developmental expression clusters (**Figure 3**; shades of red) were analyzed for  
1181 overrepresented functional annotations using gene ontology (GO) terms. The graph displays

1182 the percentage of proteins in each cluster that were annotated with a particular function. For  
1183 comparison, known myelin proteins were annotated. n.o., not over-represented.

1184

1185

1186 **Figure 5. Molecular analysis of myelin in the *Prx*<sup>-/-</sup> mouse model of CMT4F**

1187 **(A)** Myelin purified from sciatic nerves dissected from *Prx*<sup>-/-</sup> and control mice at P21 was  
1188 separated by SDS-PAGE (0.5 µg protein load) and proteins were visualized by silver  
1189 staining. Bands constituted by the most abundant myelin proteins (MPZ/P0, MBP, PRX) are  
1190 annotated. Note that no band constituted by PRX was detected in *Prx*<sup>-/-</sup> myelin and that  
1191 several other bands also display genotype-dependent differences in intensity. Gel shows n=2  
1192 biological replicates representative of n=3 biological replicates.

1193 **(B)** The relative abundance of proteins in myelin purified from *Prx*<sup>-/-</sup> sciatic nerves as  
1194 quantified by MS<sup>E</sup> is given as percent with relative standard deviation (% +/- RSD). Note the  
1195 increased relative abundance of MPZ/P0 and MBP compared to wild-type myelin (see  
1196 **Figure 2**) when PRX is lacking. Mass spectrometric quantification based on 3 biological  
1197 replicates with 4 technical replicates each (see **Figure 5-source data 1**).

1198 **(C,D)** Differential proteome analysis by DRE-UDMS<sup>E</sup> of myelin purified from *Prx*<sup>-/-</sup> and wild-  
1199 type mice. Mass spectrometric quantification based on 3 biological replicates per genotype  
1200 with 4 technical replicates each (see **Figure 5-source data 2**). **(C)** Top 40 proteins of which  
1201 the abundance is reduced (blue) or increased (red) in peripheral myelin purified from *Prx*<sup>-/-</sup>  
1202 compared to wild-type mice with the highest level of significance according to the -log<sub>10</sub>  
1203 transformed q-value (green). In the heatmaps, each horizontal line corresponds to the fold-  
1204 change (FC) of a distinct protein compared to its average abundance in wild-type myelin  
1205 plotted on a log<sub>2</sub> color scale. Heatmaps display 12 replicates, i.e. 3 biological replicates per  
1206 genotype with 4 technical replicates each. **(D-D''')** Volcano plots representing genotype-  
1207 dependent quantitative myelin proteome analysis. Data points represent quantified proteins  
1208 in *Prx*<sup>-/-</sup> compared to wild-type myelin and are plotted as the log<sub>2</sub>-transformed fold-change  
1209 (FC) on the x-axis against the -log<sub>10</sub>-transformed q-value on the y-axis. Stippled lines mark a  
1210 -log<sub>10</sub>-transformed q-value of 1.301, reflecting a q-value of 0.05 as significance threshold.  
1211 Highlighted are the datapoints representing the Top 10 proteins displaying highest zdist  
1212 values (Euclidean distance between the two points (0,0) and (x,y) with x = log<sub>2</sub>(FC) and y = -  
1213 log<sub>10</sub>(q-value) (red circles in **D**), immune-related proteins (purple circles in **D'**), proteins of  
1214 the extracellular matrix (ECM; yellow circles in **D''**) and known myelin proteins (blue circles in  
1215 **D'''**). n.d., not detected; n.q., no q-value computable due to protein identification in one  
1216 genotype only. Also see **Figure 5-supplement 1**.

1217 **(E)** Immunoblot of myelin purified from *Prx*<sup>-/-</sup> and control sciatic nerves confirms the reduced  
1218 abundance of DRP2, SLC16A1/MCT1, BSG and PMP2 in *Prx*<sup>-/-</sup> myelin, as found by

1219 differential DRE-UDMS<sup>E</sup> analysis (in **Figure 5C,D**). PRX was detected as genotype control;  
1220 PLP/DM20 and ATP1A1 serve as markers. Blot shows n=2 biological replicates per  
1221 genotype.

1222 **(F)** Teased fiber preparations of sciatic nerves dissected from *Prx*<sup>-/-</sup> and control mice  
1223 immunolabelled for MAG (red) and SLC16A1 (green). Note that SLC16A1 co-distributes with  
1224 MAG in Schmidt-Lanterman incisures (SLI) in control but not in *Prx*<sup>-/-</sup> nerves, in accordance  
1225 with the reduced abundance of SLC16A1 in *Prx*<sup>-/-</sup> myelin (**Figure 5C-E**). Also note that, in  
1226 *Prx*<sup>-/-</sup> myelin, SLI were largely undetectable by MAG immunolabeling.

1227

1228

1229 **Figure 5-supplement 1. Clustered heatmap of Pearson's correlation coefficients for**  
1230 **protein abundance comparing genotypes.**

1231 **(A)** The heatmap compares the log<sub>2</sub> transformed ppm protein abundance values from the  
1232 DRE-UDMS<sup>E</sup> runs to assess peripheral myelin purified from wild type and *Prx*<sup>-/-</sup> mice. The  
1233 inset shows the color key and the histogram for the values of the correlation coefficients.  
1234 Note that the runs cluster with a high overall correlation (>0.85) into two conditions defined  
1235 by the genotype, in agreement with the experimental design.

1236 **(B)** Volcano plot representing genotype-dependent quantitative myelin proteome analysis.  
1237 Data points represent quantified proteins in *Prx*<sup>-/-</sup> compared to wild-type myelin plotted as the  
1238 log<sub>2</sub>-transformed fold-change (FC) on the x-axis against the -log<sub>10</sub>-transformed q-value on  
1239 the y-axis. Note the different axis scale compared to **Figure 5D**. Stippled line marks a -log<sub>10</sub>-  
1240 transformed q-value of 1.301, reflecting a q-value of 0.05 as significance threshold.  
1241 Highlighted is the datapoint for PRX to illustrate that only trace amounts of PRX were  
1242 detected when assessing *Prx*<sup>-/-</sup> myelin. ATP2A1, ATP1A4 and PLCD1 were not detected in  
1243 *Prx*<sup>-/-</sup> myelin.

1244

1245

1246 **Figure 6. Progressive loss and reduced diameters of peripheral axons in *Prx*<sup>-/-</sup> mice**

1247 **(A-D)** Genotype-dependent quantitative assessment of light micrographs of toluidine-stained  
1248 semi-thin sectioned quadriceps nerve dissected at 2, 4 and 9 months of age reveals  
1249 progressive loss of peripheral axons in *Prx*<sup>-/-</sup> compared to control mice.

1250 **(A)** Representative micrographs. Arrows point at myelinated axons; asterisk denotes an  
1251 unmyelinated axon; arrowhead points at a myelin whorl lacking a recognizable axon. Scale  
1252 bars, 10 μm.

1253 **(B)** Total number of axons per nerve that are not associated with a Remak bundle.

1254 **(C)** Total number of myelinated axons per nerve.

1255 **(D)** Total number per nerve of myelin whorls that lack a recognizable axon.

1256 Mean +/- SD, n=3-4 mice per genotype and age; \*P<0.05, \*\*P<0.01, \*\*\*P<0.001 by Student's  
1257 unpaired t-test.

1258 **(E-G)** Genotype-dependent assessment of myelinated axons shows a shift toward reduced  
1259 axonal diameters in quadriceps nerves of *Prx*<sup>-/-</sup> compared to control mice at 2 months **(E)**, 4  
1260 months **(F)** and 9 months **(G)** of age. Data are presented as frequency distribution with 0.5  
1261 µm bin width. \*\*\*, p<0.001 by two-sided Kolmogorow-Smirnow test. For precise p-values see  
1262 methods section.

1263

1264

1265 **Figure 1-source data 1. Label-free quantification of proteins in wild-type PNS myelin**  
1266 **fractions by three different data acquisition modes**

1267 Identification and quantification data of detected myelin-associated proteins. Tryptic peptides  
1268 derived from four technical replicates (replicate digestion and replicate injection) per three  
1269 biological replicate (20 sciatic nerves pooled from 10 animals) were analyzed by LC-MS (12  
1270 runs in total). Proteins (FDR < 1%; 2 peptides/protein) and peptides (FDR < 1%; ≥7 amino  
1271 acids) were identified by database search against the UniprotKB/SwissProt mouse database  
1272 using PLGS. Data were post-processed with the software package ISOQuant to calculate  
1273 absolute in-sample amounts for each detected protein based on the TOP3 approach.  
1274 Reported abundance values are defined as the relative amount of each protein in respect to  
1275 the sum over all detected proteins (ppm: parts per million (w/w) of total protein). Typical  
1276 contaminant proteins like keratins were filtered.

1277 → sheet 1: protein identification details

1278 → sheet 2: WT myelin proteome by MS<sup>E</sup>

1279 → sheet 3: WT myelin proteome by UD-MS<sup>E</sup>

1280 → sheet 4: WT myelin proteome by DRE UD-MS<sup>E</sup>

1281 → sheet 5: 45 proteins additionally identified in WT myelin by 1D-gel-LC-MS

1282

1283

1284 **Figure 3-source data 1. Normalized developmental mRNA abundance data**

1285 → sheet 1: normalized values for all individual 4 biological replicates per age

1286 → sheet 2: normalized values for biological replicates averaged to give mean per age

1287

1288

1289 **Figure 5-source data 1. Label-free quantification of proteins in PNS myelin fractions**  
1290 **from *Prx*<sup>-/-</sup> mice by MSe**

1291 Identification and quantification data of detected myelin-associated proteins. Tryptic peptides  
1292 derived from four technical replicates (replicate digestion and replicate injection) per three



1293 biological replicate (20 sciatic nerves pooled from 10 animals) were analyzed by LC-MS (12  
1294 runs in total). Proteins (FDR < 1%; 2 peptides/protein) and peptides (FDR < 1%; ≥7 amino  
1295 acids) were identified by database search against the UniprotKB/SwissProt mouse database  
1296 using PLGS. Data were post-processed with the software package ISOQuant to calculate  
1297 absolute in-sample amounts for each detected protein based on the TOP3 approach.  
1298 Reported abundance values are defined as the relative amount of each protein in respect to  
1299 the sum over all detected proteins (ppm: parts per million (w/w) of total protein). Typical  
1300 contaminant proteins like keratins were filtered.

1301 → sheet 1: protein identification details

1302 → sheet 2: *Prx*<sup>-/-</sup> myelin proteome by MS<sup>E</sup>

1303

1304

1305 **Figure 5-source data 2. Label-free quantification of proteins in PNS myelin fractions**  
1306 **from WT and *Prx*<sup>-/-</sup> mice by DRE-UDMS<sup>e</sup>**

1307 Identification and quantification data of detected myelin-associated proteins by DRE-UDMS<sup>e</sup>.  
1308 For each genotype, tryptic peptides derived from four technical replicates (replicate digestion  
1309 and replicate injection) per three biological replicate (20 sciatic nerves pooled from 10  
1310 animals) were analyzed by LC-MS (24 runs in total). Proteins (FDR < 1%; 2 peptides/protein)  
1311 and peptides (FDR < 1%; ≥7 amino acids) were identified by database search against the  
1312 UniprotKB/SwissProt mouse database using PLGS. Data were post-processed with the  
1313 software package ISOQuant to calculate absolute in-sample amounts for each detected  
1314 protein based on the TOP3 approach. Reported abundance values are defined as the  
1315 relative amount of each protein in respect to the sum over all detected proteins (ppm: parts  
1316 per million (w/w) of total protein). Typical contaminant proteins like keratins were filtered. The  
1317 -log<sub>10</sub>-transformed q-value was plotted against the log<sub>2</sub>-transformed fold change to obtain  
1318 the volcano plot shown in Figure 5D. As no imputation of missing values was performed,  
1319 proteins exclusive for only one of the conditions do not appear in the volcano plot, but are  
1320 appended at the end of the list. Criteria for statistically significant regulation were as follows:  
1321 fold change of at least 1.5 and q-value below 0.05.

1322 → sheet 1: protein identification details

1323 → sheet 2: comparison of WT vs. *Prx*<sup>-/-</sup> myelin proteome by DRE-UDMS<sup>E</sup>

1324

1325

Protein name	Gene	Reference	TMD	Cluster
2-hydroxyacylsphingosine 1-beta-galactosyltransferase	<i>Ugt8</i>	Bosio et al., 1996	2	P6-up
Syntrophin $\alpha$ 1	<i>Snta1</i>	Fuhrmann-Stroissnigg et al., 2012	-	P18-up
Annexin A2	<i>Anxa2</i>	Hayashi et al., 2007	-	Descending
Band 4.1 protein B / 4.1B	<i>Epb4113</i>	Ivanovic et al., 2012	-	Descending
Band 4.1 protein G / 4.1G	<i>Epb4112</i>	Ohno et al., 2006	-	P6-up
Breast carcinoma-amplified sequence 1	<i>Bcas1</i>	Ishimoto et al., 2017	-	P6-up
Cadherin 1/ E-Cadherin	<i>Cdh1</i>	Fannon et al., 1995	1	P18-up
Carbonic anhydrase 2	<i>Ca2</i>	Cammer et al., 1987	-	Descending
Catenin $\alpha$ 1	<i>Ctnna1</i>	Murata et al., 2006	-	U-shaped
Catenin $\beta$ 1	<i>Ctnnb1</i>	Fannon et al., 1995	-	Descending
Caveolin 1	<i>Cav1</i>	Mikol et al., 2002	1	P18-up
CD9, tetraspanin 29	<i>Cd9</i>	Ishibashi et al., 2004	4	P18-p
CD59A	<i>Cd59a</i>	Funabashi et al., 1994	1	P18-up
CD47, integrin-associated signal transducer	<i>Cd47</i>	Gitik et al., 2011	5	P6-up
CD81, tetraspanin 28	<i>Cd81</i>	Ishibashi et al., 2004	4	P18-up
CD82, tetraspanin 27	<i>Cd82</i>	Chernousov et al., 2013	4	P18-up
CD151, tetraspanin 24	<i>Cd151</i>	Patzig et al., 2011	4	P18-up
Cell adhesion molecule 4/ NECL4	<i>Cadm4</i>	Spiegel et al., 2007	1	P6-up
Cell division control protein 42	<i>Cdc42</i>	Benninger et al., 2007	-	P6-up
Cell surface glycoprotein MUC18	<i>Mcam</i>	Shi et al., 1998	1	Descending
Ciliary neurotrophic factor	<i>Cntf</i>	Rende et al., 1992	-	Late-up
CKLF-like MARVEL TMD-containing 5	<i>Cmtm5</i>	Patzig et al., 2011	4	P6-up
Claudin-19	<i>Cldn19</i>	Miyamoto et al., 2005	4	P6-up
Cofilin 1	<i>Cfl1</i>	Sparrow et al., 2012	-	Descending
Crystallin $\alpha$ 2	<i>Cryab</i>	d'Antonio et al., 2006	-	P18-up
Cyclic nucleotide phosphodiesterase	<i>Cnp</i>	Matthieu et al., 1980	-	P6-up
Sarcoglycan $\delta$	<i>Sgcd</i>	Cai et al., 2007	1	Late-up
Dihydropyrimidinase related protein 1	<i>Crmp1</i>	d'Antonio et al., 2006	-	Descending
Disks large homolog 1	<i>Dlg1</i>	Cotter et al., 2010	-	Descending
Dynein light chain 1	<i>Dynll1</i>	Mylykoski et al. 2018	-	P6-up
Dystroglycan	<i>Dag1</i>	Yamada et al., 1994	1	P6-up
Dystrophin/DP116	<i>Dmd</i>	Cai et al., 2007	-	P6-up
Dystrophin-related protein 2	<i>Drp2</i>	Sherman et al., 2001	-	P18-up
E3 ubiquitin-protein ligase NEDD4	<i>Nedd4</i>	Liu et al., 2009	-	Descending
Ezrin	<i>Ezr</i>	Scherer et al., 2001	-	P6-up
Fatty acid synthase	<i>Fasn</i>	Salles et al., 2002	-	P6-up
Flotillin 1	<i>Flot1</i>	Lee et al., 2014	-	P18-up
Gap junction $\beta$ 1 protein / Cx32	<i>Gjb1</i>	Li et al., 2002	4	P18-up
Gap junction $\gamma$ 3 protein / Cx29	<i>Gjc3</i>	Li et al., 2002	1	P6-up
Gelsolin	<i>Gsn</i>	Gonçaves et al., 2010	-	Late-up
Glycogen synthase kinase 3 $\beta$	<i>Gsk3b</i>	Ogata et al., 2004	-	P6-up
Integrin $\alpha$ 6	<i>Itga6</i>	Nodari et al., 2008	1	P6-up
Integrin $\alpha$ V	<i>Itgav</i>	Chernousov & Carey, 2003	1	Descending
Integrin $\beta$ 1	<i>Itgb1</i>	Feltri et al., 2002	1	Descending
Integrin $\beta$ 4	<i>Itgb4</i>	Quattrini et al., 1996	2	P18-up
Junctional adhesion molecule C	<i>Jam3</i>	Scheiermann et al., 2007	1	P18-up
Laminin $\alpha$ 2	<i>Lama2</i>	Yang et al., 2005	-	P6-up
Laminin $\alpha$ 4	<i>Lama4</i>	Yang et al., 2005	-	Descending
Laminin $\beta$ 1	<i>Lamb1</i>	LeBeau et al., 1994	-	Descending
Laminin $\beta$ 2	<i>Lamb2</i>	LeBeau et al., 1994	-	P18-up
Laminin $\gamma$ 1	<i>Lamc1</i>	Chen & Strickland, 2003	-	Descending
Membrane Palmitoylated Protein 6	<i>Mpp6</i>	Saitoh et al., 2019	-	P6-up
Microtubule-associated protein 1A	<i>Map1a</i>	Fuhrmann-Stroissnigg et al., 2012	-	P18-up
Microtubule-associated protein 1B	<i>Map1b</i>	Fuhrmann-Stroissnigg et al., 2012	-	P6-up
Mitogen-activated protein kinase 1/ ERK2	<i>Mapk1</i>	Mantuano et al., 2015	-	Descending
Mitogen-activated protein kinase 3/ ERK1	<i>Mapk3</i>	Mantuano et al., 2015	-	P18-up
Moesin	<i>Msn</i>	Scherer et al., 2001	-	Unchanged
Monocarboxylate transporter 1	<i>Slc16a1</i>	Domenech-Estevéz et al., 2015	11	P18-up

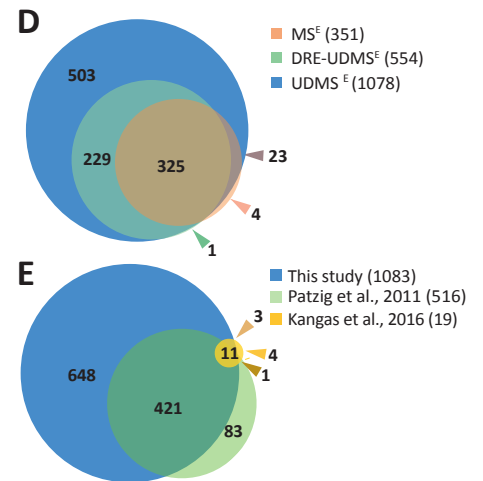
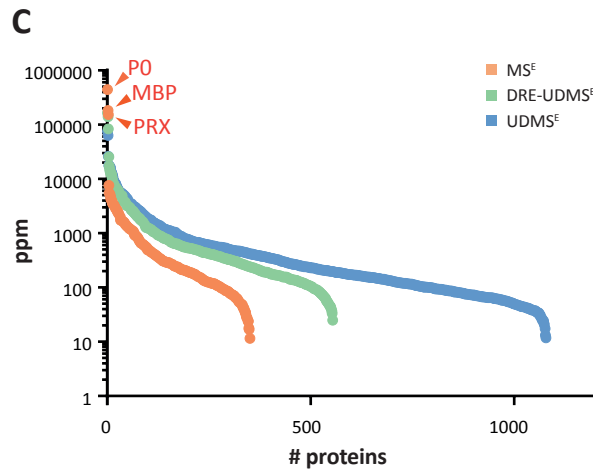
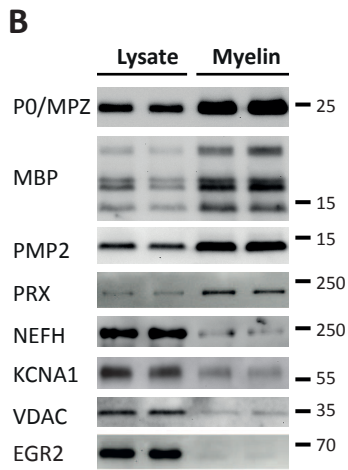
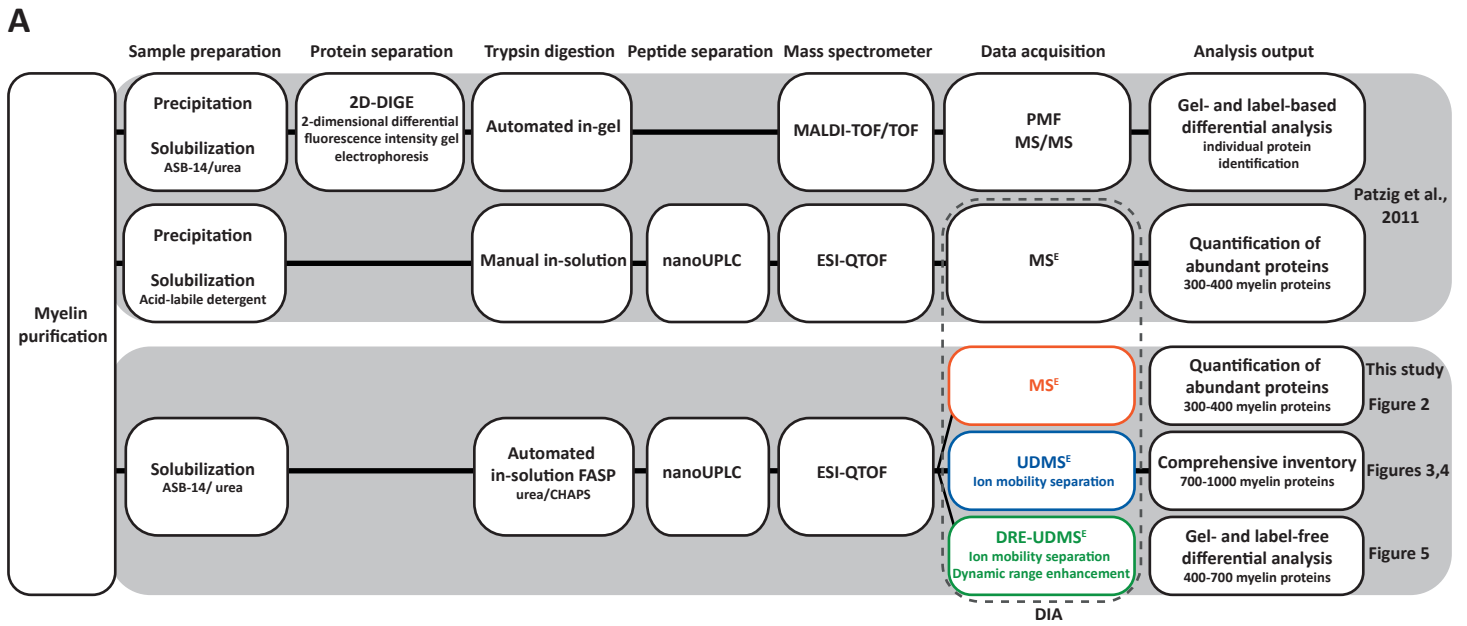
Myelin associated glycoprotein	<i>Mag</i>	Figlewicz et al., 1981	1	P6-up
Myelin basic protein	<i>Mbp</i>	Boggs, 2006	-	P6-up
Myelin protein 2	<i>Pmp2</i>	Trapp et al., 1984	-	P18-up
Myelin protein zero/ P0	<i>Mpz</i>	Giese et al., 1992	1	P6-up
Myelin proteolipid protein	<i>Plp1</i>	Garbern et al., 1997	4	P6-up
Myotubularin-related protein 2	<i>Mtmr2</i>	Bolino et al., 2004	-	P6-up
Noncompact myelin-associated protein	<i>Nemap</i>	Ryu et al., 2008	1	P18-up
NDRG1, N-myc downstream regulated	<i>Ndrg1</i>	Berger et al., 2004	-	P18-uP
Neurofascin	<i>Nfasc</i>	Tait et al., 2000	2	P18-up
Nidogen 1	<i>Nid1</i>	Lee et al., 2007	-	Descending
P2X purinoceptor 7	<i>P2rx7</i>	Faroni et al., 2014	-	P6-up
Paxillin	<i>Pxn</i>	Fernandez-Valle et al., 2002	-	P6-up
Periaxin	<i>Prx</i>	Gillespie et al., 1994	-	P6-up
Plasmalipin	<i>Pllp</i>	Bosse et al., 2003	4	P18-up
Profilin 1	<i>Pfn1</i>	Montani et al., 2014	-	Descending
Lin-7 homolog C	<i>Lin7c</i>	Saitoh et al., 2017	-	P6-up
Rac1	<i>Rac1</i>	Benninger et al., 2007	-	U-Shaped
Radixin	<i>Rdx</i>	Scherer et al., 2001	-	Descending
RhoA	<i>Rhoa</i>	Brancolini et al., 1999	-	U-Shaped
Septin 2	<i>Sept 2</i>	Buser et al., 2009	-	Descending
Septin 7	<i>Sept 7</i>	Buser et al., 2009	-	U-Shaped
Septin 8	<i>Sept 8</i>	Patzig et al., 2011	-	P18-up
Septin 9	<i>Sept 9</i>	Patzig et al., 2011	-	P6-up
Septin 11	<i>Sept 11</i>	Buser et al., 2009	-	Descending
Sirtuin 2, NAD-dependent deacetylase	<i>Sirt2</i>	Werner et al., 2007	-	P18-up
Spectrin alpha chain, non-erythrocytic 1	<i>Sptan1</i>	Susuki et al., 2018	-	P18-up
Spectrin beta chain, non-erythrocytic 1	<i>Sptbn1</i>	Susuki et al., 2018	-	P18-up
Tight junction protein ZO-1	<i>Tjpl</i>	Poliak et al., 2007	-	P6-up
Tight junction protein ZO-2	<i>Tjp2</i>	Poliak et al., 2007	-	P6-up
Transferrin	<i>Tf</i>	Liu et al., 1990	2	Late-up
Vimentin	<i>Vim</i>	Triolo et al., 2012	-	Unchanged
Vinculin	<i>Vcl</i>	Beppu et al., 2015	-	Descending

**Table 1. Known myelin proteins in the myelin proteome.** Proteins mass-spectrometrically identified in peripheral myelin are compiled according to availability of prior references as myelin proteins. Given are the official gene name, one selected reference, the number of transmembrane domains (TMD) and the mRNA abundance profile cluster (see **Figure 3**).

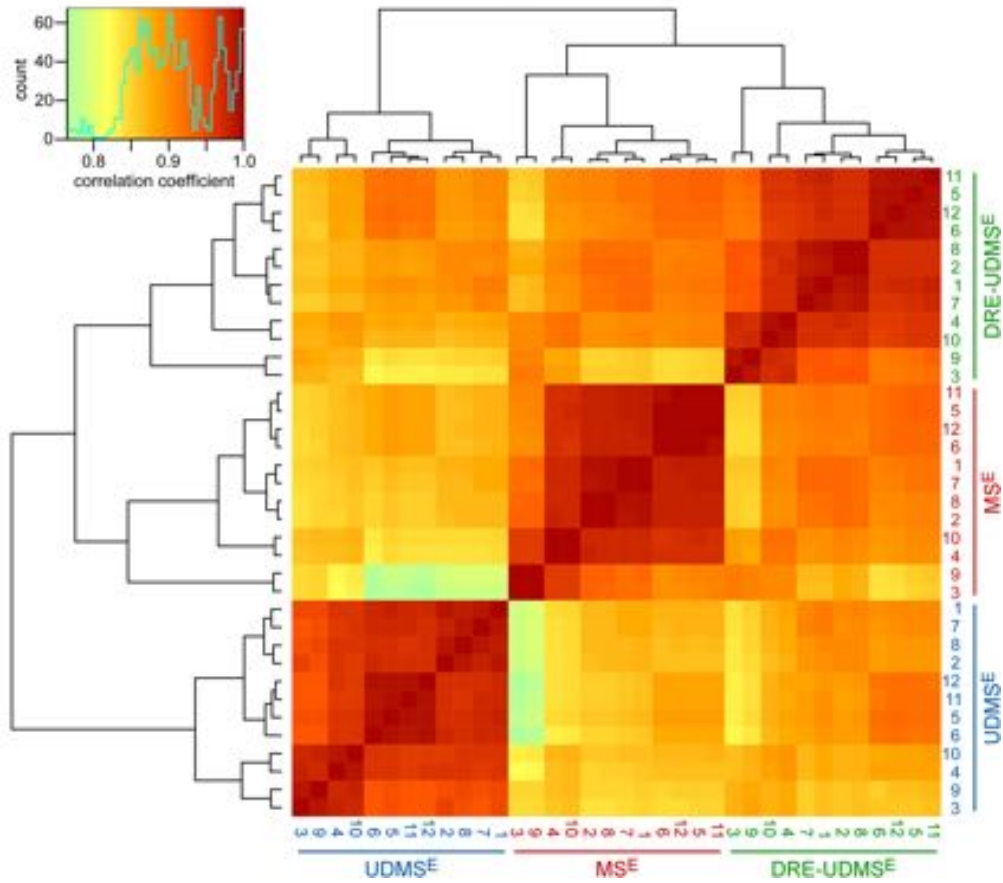
1327  
1328  
1329  
1330  
1331

Protein name	Gene name	OMIM#	Gene Locus	Neuropathy
Monoacylglycerol lipase ABHD12	<i>ABHD12</i>	613599	20p11.21	PHARC
Apoptosis-inducing factor 1	<i>AIFM1</i>	300169	Xq26.1	CMTX4, DFNX5
Na <sup>+</sup> /K <sup>+</sup> -transporting ATPase $\alpha$ 1	<i>ATP1A1</i>	182310	1p13.1	CMT2DD
Cytochrome c oxidase subunit 6A1	<i>COX6A1</i>	602072	12q24.31	CMTRID
Dystrophin-related protein 2	<i>DRP2</i>	300052	Xq22.1	CMTX
Dynactin subunit 1	<i>DCTN1</i>	601143	2p13.1	DHMN7B
Dynamamin 2	<i>DNM2</i>	602378	19p13.2	CMT2M, CMTDIB
Cytoplasmic dynein 1 heavy chain 1	<i>DYNC1H1</i>	600112	14q32.31	CMT20, SMALED1
E3 SUMO-protein ligase	<i>EGR2</i>	129010	10q21.3	CMT1D, CMT3, CMT4E
Glycine-tRNA ligase	<i>GARS</i> (Gart)	600287	7p14.3	CMT2D, HMN5A
Gap junction $\beta$ 1 protein / Cx32	<i>GJB1</i>	304040	Xq13.1	CMTX1
Guanine nucleotide-binding protein $\beta$ 4	<i>GNB4</i>	610863	3q26.33	CMTDIF
Histidine triad nucleotide-binding protein 1	<i>HINT1</i>	601314	5q23.3	NMAN
Hexokinase 1	<i>HK1</i>	142600	10q22.1	CMT4G
Heat shock protein $\beta$ 1	<i>HSPB1</i>	602195	7q11.23	CMT2F, DHMN2B
Kinesin heavy chain isoform 5A	<i>KIF5A</i>	602821	12q13.3	SPG10
Prelamin A/C	<i>LMNA</i>	150330	1q22	CMT2B1
Neprilysin	<i>MME</i>	120520	3q25.2	CMT2T, SCA43
Myelin protein zero/ P0	<i>MPZ</i>	159440	1q23.3	CHN2, CMT1B, CMT2I, CMT2J, CMT3, CMTDID, Roussy-Levy syndrome
Myotubularin-related protein 2	<i>MTMR2</i>	603557	11q21	CMT4B1
Alpha-N-acetylglucosaminidase	<i>NAGLU</i> (NAGA)	609701	17q21.2	CMT2V
NDRG1, N-myc downstream regulated	<i>NDRG1</i>	605262	8q24.22	CMT4D
Neurofilament heavy polypeptide	<i>NEFH</i>	162230	22q12.2	CMT2CC
Neurofilament light polypeptide	<i>NEFL</i>	162280	8p21.2	CMT2E, CMT1F, CMTDIG
Peripheral myelin protein 2	<i>PMP2</i>	170715	8q21.13	CMT1G
Peripheral myelin protein 22	<i>PMP22</i>	601907	17p12	CMT1A, CMT1E, CMT3, HNPP, Roussy-Levy syndrome
Ribose-phosphate pyrophosphokinase 1	<i>PRPS1</i>	311850	Xq22.3	Arts syndrome, CMTX5, DFNX1
Periaxin	<i>PRX</i>	605725	19q13.2	CMT4F, CMT3
Ras-related protein Rab 7a	<i>RAB7A</i>	602298	3q21.3	CMT2B
Septin 9	<i>SEPT9</i>	604061	17q25.3	HNA
Transitional ER-ATPase	<i>VCP</i>	601023	9p13.3	CMT2Y
Tryptophan-tRNA ligase, cytoplasmic	<i>WARS</i>	191050	14q32.32	HMN9
Tyrosine-tRNA ligase, cytoplasmic	<i>YARS</i>	603623	1p35.1	DI-CMTC

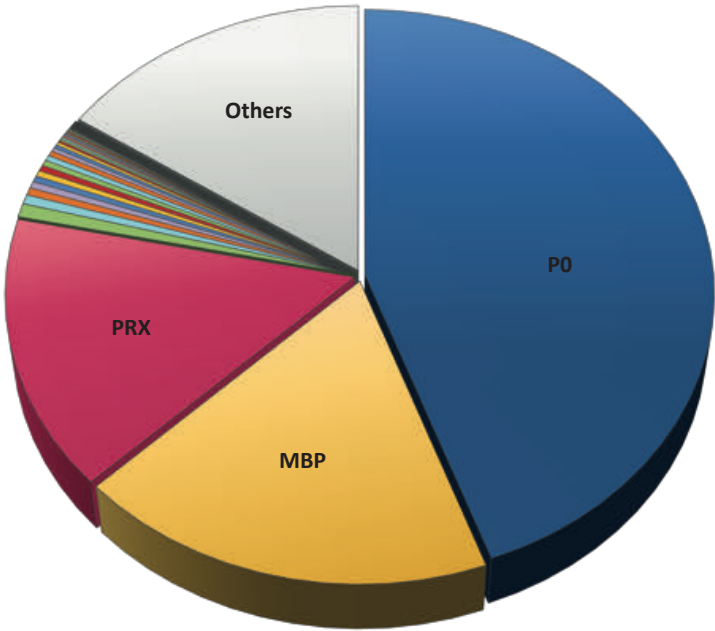
1333 **Table 2. Peripheral myelin proteins identified in PNS myelin involved in neuropathological diseases.** Proteins  
1334 massspectrometrically identified in peripheral myelin were analyzed regarding the involvement of the ortholog human gene  
1335 in neuropathological diseases. PMP22 was added, though it was not identified by MS analyses due to its unfavorable  
1336 distribution of tryptic cleavage sites. CMT, Charcot-Marie-Tooth disease; DHMN, distal hereditary motor neuropathy; DI-  
1337 CMTC, dominant intermediate CMTC; DFN, X-linked deafness; HMN, hereditary motor neuropathy; HSAN, hereditary  
1338 sensory and autonomic neuropathy; HNA, hereditary sensory and autonomic neuropathy; OMIM, Online Mendelian  
1339 Inheritance in Man; PHARC, polyneuropathy, hearing loss, ataxia, retinitis pigmentosa and cataract; SCA, spinocerebellar  
1340 ataxia; SPG, spastic paraplegia.



Siems et al., Figure 1-supplement 1



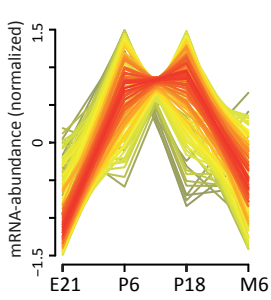
Siems et al., Figure 2



Protein	% (+/- RSD)		Protein	% (+/- RSD)	
PO/ MPZ	44.48	4.15	LAMC1	0.06	0.01
MBP	18.35	1.15	RAC1	0.05	0.01
PRX	15.48	1.46	VCL	0.04	0.00
CD9	0.77	0.15	CA2	0.04	0.01
SPTBN1	0.52	0.06	SEPT2	0.04	0.00
SPTAN1	0.42	0.07	CFL1	0.04	0.01
EPB41L2	0.38	0.05	CRYAB	0.03	0.00
VIM	0.34	0.07	MPP6	0.03	0.00
CNP	0.33	0.06	CAV1	0.03	0.00
TF	0.33	0.03	SEPT7	0.02	0.00
PMP2	0.32	0.03	GJC3	0.02	0.00
MAP1B	0.31	0.06	RDX	0.02	0.00
FASN	0.29	0.04	CDC42	0.02	0.01
ANXA2	0.22	0.03	PFN1	0.02	0.00
MAG	0.20	0.02	SEPT11	0.02	0.00
PLP1	0.17	0.02	CRMP1	0.02	0.00
CD81	0.12	0.01	RHOA	0.02	0.00
GSN	0.11	0.02	MAPK3	0.02	0.00
PLLP	0.11	0.01	MAPK1	0.01	0.00
BCAS1	0.09	0.00	CMTM5	0.01	0.00
NDRG1	0.09	0.03	JAM3	0.01	0.00
MSN	0.09	0.01	DYNLL1	0.01	0.03
EPB41L3	0.07	0.01	EZR	0.01	0.00
NID1	0.07	0.01	CD59A	0.01	0.00
CADM4	0.07	0.01	Others	15.39	

**A**

**P6-up**

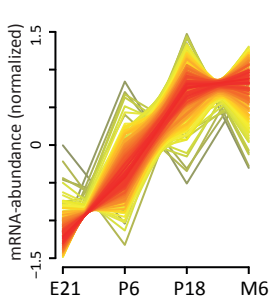


Aacs	<b>Cd47</b>	Cpne3	Eml1	Gmfb	<b>Lama2</b>	<b>Mpp6</b>	Osbp1a	Pygb	<b>Tjp1</b>
Abcd3	<b>Cdc42</b>	Cpt1a	<b>Epb4112</b>	Gna11	Letm1	<b>Mpz</b>	<b>P2rx7</b>	Rab8b	<b>Tjp2</b>
Acaca	Cf12	Csnk2a1	<b>Ezr</b>	Gnai1	<b>Lin7c</b>	<b>Mtmr2</b>	Pdhh	Rcn1	Tspan15
Acat2	Ckb	Cyp51	Fam177a1	Gnaq	Lss	Mvk	Pgls	Rer1	Tubb2a
Adam10	<b>Cldn19</b>	<b>Dag1</b>	Far1	Gng2	M6pr	Myh14	Plg	Rpl13	Ubl3
Agps	<b>Cmtm5</b>	Dhcr7	<b>Fasn</b>	<b>Gsk3b</b>	<b>Mag</b>	Myo18a	<b>Plp1</b>	Rps16	<b>Ugt8</b>
App1	<b>Cnp</b>	Dhrs1	Fdft1	Gypc	<b>Map1b</b>	Naga	<b>Pmp22</b>	Rps2	
Art3	Col15a1	<b>Dmd</b>	Fdps	Hmgcs1	Map4	Napb	Ppa2	<b>Sept9</b>	
<b>Bcas1</b>	Col1a1	Dusp15	Fmn12	Hsd17b7	Map6	Ndufb7	Prkacb	Slc25a10	
Bdh1	Col1a2	Dync1h1	Fscn1	Idi1	Mapre3	Ndufs8	<b>Prx</b>	Slc25a5	
Brox	Col28a1	<b>Dynll1</b>	Fut8	<b>Itga6</b>	<b>Mbp</b>	Nefl	Psmb6	Slc44a1	
Cab39l	Col4a2	Eci1	Gamt	Itpr3	Mical1	Nefm	Psmc3	Snap91	
<b>Cadm4</b>	Col6a1	Ehd3	Gapdhs	Kif5b	Mlec	Nsdhl	Pura	Sorbs1	
Camk2b	Col6a2	Elov1	<b>Gjc3</b>	Klc2	Mme	Opa1	<b>Pxn</b>	Stk39	

**B**

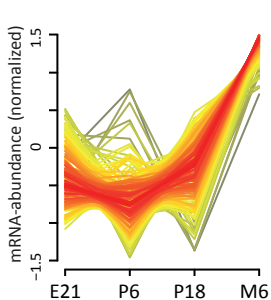
Cluster	#mRNA
1 P6-up	132
2 P18-up	203
3 Late-up	186
4 U-shaped	154
5 Descending	245
6 Unchanged	126
All	1046

**P18-up**



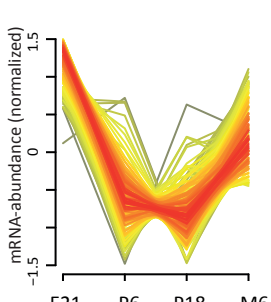
Abat	Aldh9a1	Atp6v1e1	<b>Cd59</b>	<b>Cryab</b>	Fkbp1a	Hibch	<b>Lamb2</b>	Mpc1	Ndufs4	<b>Pmp2</b>	Rab5b	Serpinf1	Steap3	Tst
Abhd12	Anxa11	Atp6v1h	<b>Cd81</b>	Ctsd	Flnb	Hk1	Lamp1	Mpp2	Ndufs7	Por	Rab7a	Sft2d2	Stx12	Tubb4a
Acaa1a	Anxa5	Auh	<b>Cd82</b>	Cyb5a	<b>Flot1</b>	Hras	Lamp2	Mpst	Ndufv2	Prdx5	Rdh11	Sfxn3	Stxbp1	Vat1l
Acaa2	Arl3	Bcap31	<b>Cd9</b>	Cyb5r3	Gatm	Hsd17b10	Lanc1	Prep	Nes	Reep5	Sirt2	Sucla2	Vps26a	
Acadm	Arl8b	Bgn	<b>Cdh1</b>	Ddah1	Gdi1	Hsd17b11	Ldhb	Myo1b	<b>Nfasc</b>	Prkca	Rida	<b>Slc16a1</b>	Sult1a1	Vps29
Acads	Asah1	Bphl	Cdpt	Decr1	<b>Gjb1</b>	Hsd17b12	Limch1	Myo1c	Nptn	Psmf1	Rtkn	Slc25a1	Susd2	Vsn1
Acadvl	Asl	<b>Bsg</b>	Cers2	Dnm1	Glod4	Hsd17b4	Maoa	Ncdn	Ostf1	Rab11b	Rtn4	Slc2a1	Svid	Ywhaq
Acs1	Atp1a1	<b>Cadm3</b>	Chchd3	Dpysl2	Glul	Hspa12a	<b>Map1a</b>	<b>Ncmmap</b>	Pcolce	Rab12	Rufy3	Slc3a2	Sypl1	
Acss2	Atp1a2	Canx	Cliip2	<b>Drp2</b>	Gnao1	Hspa1a	Map1lc3a	<b>Ndrgr1</b>	Pdcd6ip	Rab21	S100a6	Slc44a2	Taldo1	
Ak3	Atp1a4	Capn1	Cmtm6	Ech1	Gpi	Hspa2	Map1lc3b	Ndrgr2	Pfkm	Rab2a	Sacm1	<b>Snta1</b>	Tecr	
Aldh1a1	Atp1b3	Capn2	Cndp2	Eno2	Hadh	<b>Itgb4</b>	<b>Mapk3</b>	Ndrgr4	Phb	Rab2b	Sbds	Sod2	Tkt	
Aldh1a7	Atp6v0c	<b>Cav1</b>	Comt	Etfb	Hagh	<b>Jam3</b>	Marc2	Ndufa13	Plec	Rab3a	Scarb2	Sparc	Tln1	
Aldh3a2	Atp6v1c1	Cavin3	Copg2	Fam213a	Hepacam	Jup	Mgll	Ndufa7	Plekhh1	Rab43	Scp2	<b>Sptan1</b>	Tns3	
Aldh6a1	Atp6v1d	<b>Cd151</b>	Crip2	Fis1	Hibadh	Kit	Mgst3	Ndufb4	<b>Pilp</b>	Rab4b	<b>Sept8</b>	<b>Sptbn1</b>	Tom1l2	

**Late-up**



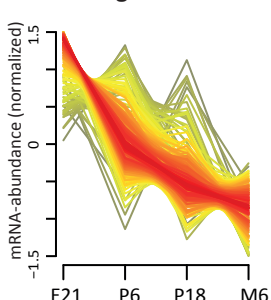
Actn3	Arpc4	Cab39	Cfh	Des	Esyt1	Got2	Idh3g	Myl6	Pdha1	Rab18	Rras	Stx7	Uqcrb
Ahcy	Aspa	Camk2g	Cisd1	Dnajb4	Efta	Gpd1	lvd	Myl9	Pdlim5	Rab5c	Rras2	Tagln	Vat1
Akr1b1	Atp12a	Capg	Ckm	Dnpep	F13a1	Gpd1l	Lap3	Ndufa5	Peebp1	Rhob	Rtn1	Tagln3	Vwa5a
Aldh2	Atp1a3	Capns1	Ckmt1	Dstn	Fabp4	Gpx3	Lcp1	Ndufa6	Pfkp	Rhog	S100b	<b>Tf</b>	Zc2h1a
Aldoa	Atp1b1	Capzb	<b>Cntf</b>	Dusp3	Fam129b	Gpx4	Lypla2	Ndufa8	Pgam2	Rpl12	Sbspon	Tomm34	
Aldoc	Atp2b2	Car3	<b>Cntn1</b>	Dynll2	Fbxo2	<b>Gsn</b>	Lyz2	Ndufb10	Picalm	Rpl13a	Sdha	Tpi1	
Anepc	Atp5f1d	Cast	Coro1a	Echs1	Fgg	Gstk1	Macrodl	Ndufb3	Pkm	Rpl19	Serpinb6a	Tpm1	
Anxa1	Atp5mg	Cat	Cox41	Eef1a2	Flot2	Gstm1	Mapt	Ndufb6	Plin1	Rpl26	Serping1	Tppp3	
Anxa3	Atp6v1g1	Cav2	Cox6c	Ehd2	Fn3krp	Gstm2	Mdh1	Ndufc2	Plin3	Rpl29	Sfn	Tsg101	
Anxa7	Bag3	Cavin1	Cp	Ehd4	G6pd	Gstm3	Me1	Npc2	Pls3	Rpl30	<b>Sgcd</b>	Tuba1c	
Aoc3	Bag5	Cavin2	Csrp1	Eif4a2	Gfap	Gstp1	Mrc1	Ogn	Prnp	Rpl36	Slc25a20	Tuba8	
Apoe	Bcam	Cd36	Cst3	Eno3	Glud1	Hadhb	Myh11	Pacsin2	Prph	Rps14	Scng	Twf2	
ApoH	BlvrB	Ces1d	Dcn	Entpd2	Gnai2	Hspa1l	Myh4	Pc	Psmc6	Rps15	Sord	Uchl1	
Arl6ip5	C3	Cfb	Dctn2	Ephx1	Gng3	Hspb1	Myl12b	Pcmt1	Pygm	Rps25	Sri	Ugp2	

**U-shaped**



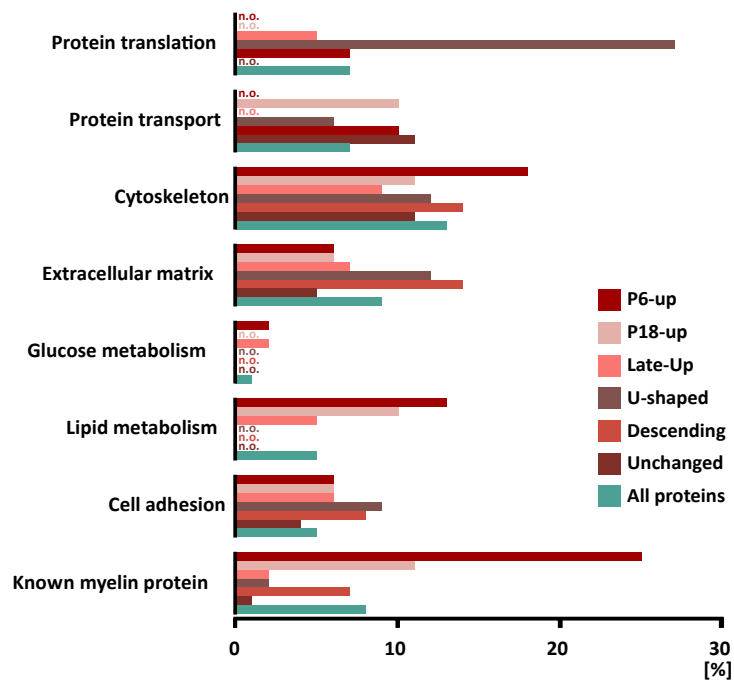
Acadl	Atp5f1b	Cyts	Gclm	Mat2a	Ppia	Rack1	Rpl23	Rpl9	Rps8	Tomm70
Acot7	Atp5mf	Dnm3	Gnb1	Mcts1	Ppid	Ralb	Rpl23a	Rpn2	Rpsa	Tpm3
Actb	Avil	Dpysl4	Gng12	Ndufa12	Ppp1cb	Rap1a	Rpl24	Rps11	S100a10	Tuba4a
Actn1	Cacybp	Dsp	Gpx1	Ndufa3	Ppp2r1b	Rap1b	Rpl27	Rps15a	<b>Sept7</b>	Tubb3
Actn4	Calm1	Dync1i2	Hpcal1	Ndufa4	Ppp2r2a	<b>Rhoa</b>	Rpl27a	Rps20	Skp1	Ube2d1
Adsl	Camk2d	Eef1a1	Hsp90b1	Ndufs1	Prdx1	Rhoc	Rpl28	Rps23	Slc25a24	Ugcr1
Ahsa1	Capza2	Ehd1	Hspa12b	Nxn	Prdx3	Rpl10	Rpl3	Rps24	Slc25a3	Vapa
Akr1a1	Cct4	Emc1	Hspa8	Pacsin1	Prps1	Rpl11	Rpl32	Rps27a	Slc25a4	Vdac3
Anp32a	Cnn2	Eno1	Ina	Paics	Psma6	Rpl14	Rpl35	Rps3	Snx1	Wdr1
Anxa6	Cnn3	Erp29	Kpna4	Pcbp2	Ptges3	Rpl15	Rpl4	Rps3a	Snx2	Ybx3
Ap2b1	Cox6a1	Etf1	Lasp1	Pdia4	Rab39a	Rpl17	Rpl5	Rps4x	Ssr4	Ywhab
Arhgap1	Cpne6	Fbn1	Ldha	Pgam1	Rab6b	Rpl18	Rpl6	Rps5	Stoml2	Ywhag
Arpc1b	Cs	Fh	Lman2	Pgk1	Rab8a	Rpl21	Rpl7	Rps6	Tagln2	Ywhah
Arpc5	<b>Ctnna1</b>	Fhl1	Lxn	Phgdh	<b>Rac1</b>	Rpl22	Rpl7a	Rps6ka3	Thy1	Zyx

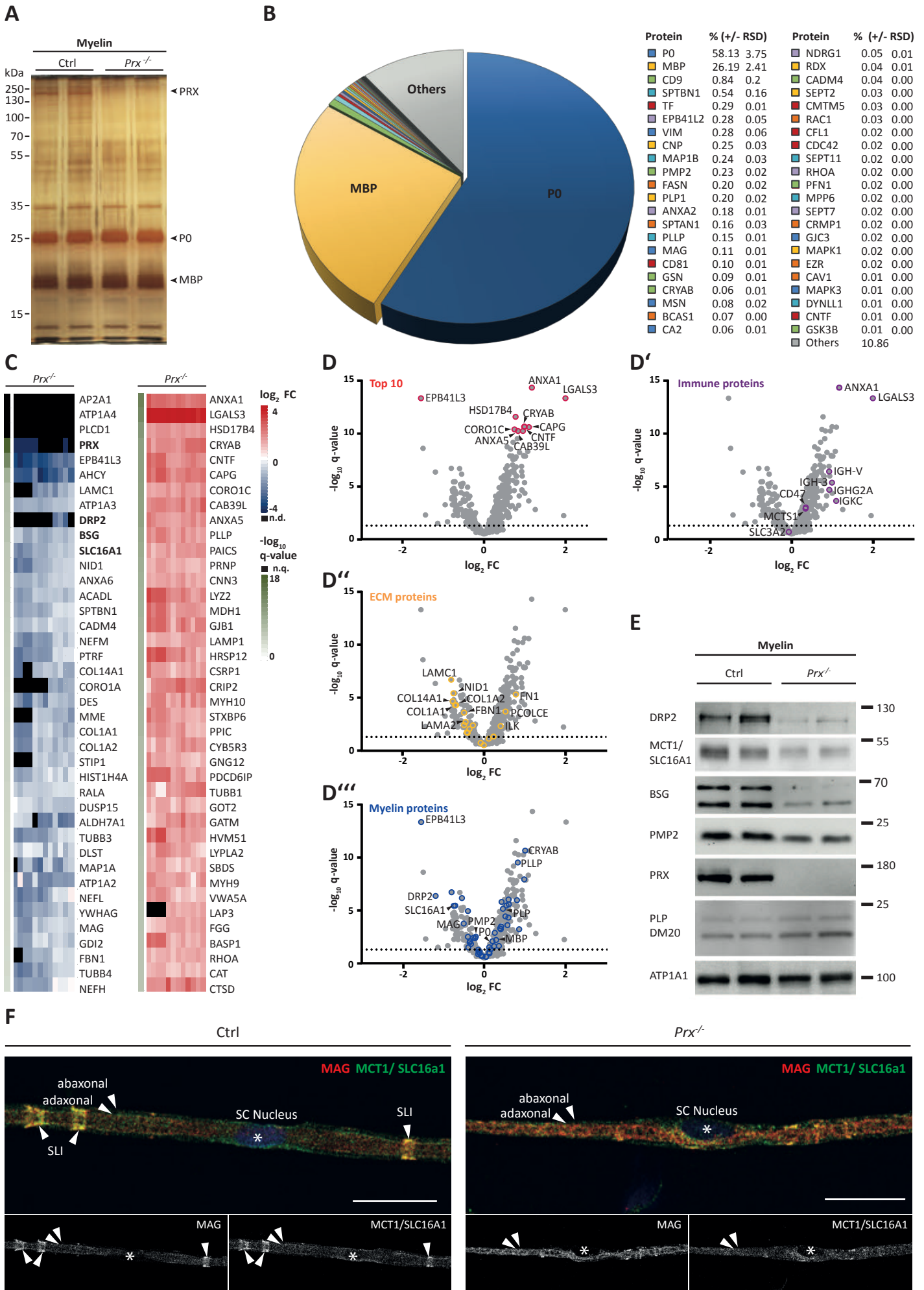
**Descending**



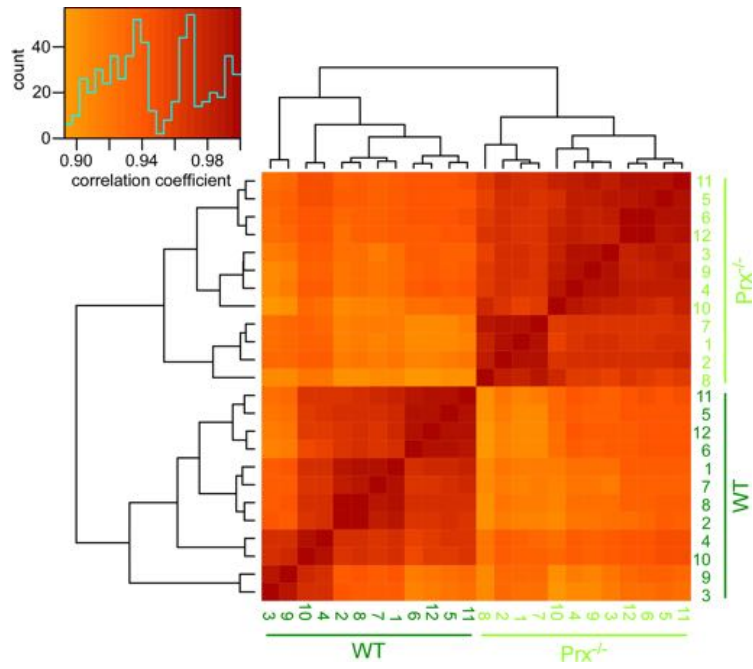
Abce1	Apex1	Calu	Col18a1	Dnajb11	Fermt2	Hist1h1a	Ilk	Lrrc59	Nid2	Pdia3	Psmb2	Rps17	Snd1	Tomm40	Ybx1
Acly	Apoa1	Cand1	Copa	Dnm1l	Flna	Hist1h1b	Immt	Lum	Nipsnap1	Pdia6	Psmd13	Rps18	Snx6	Tubb1	Ykt6
Actr1b	Arcn1	Capn5	Copb1	Dpysl3	Flncl	Hist1h1e	Ipo5	<b>Mapk1</b>	Nipsnap3b	<b>Pfn1</b>	Psmd5	Rps19	Ssr1	Tubb2b	Ywhae
Actr2	Arf4	Capza1	Cope	Dpysl5	Fnl1	Hist1h3a	Ilgap1	Mapre1	Nme1	Phb2	Psmd7	Rrbp1	Ssr3	Tubb4b	Ywhaz
Add3	Arf5	<b>Car2</b>	Copg1	Dync1li1	Ganab	Hist1h3b	Islr	Marcks	Nme2	Plcd1	Ptpa	Sars	Stip1	Tubb5	Zc3hav1l
Agk	Arf6	Cct2	Coro1c	Eef1d	Gars	Hmgb1	Isoc1	<b>Mcam</b>	Nnt	Postn	Ran	Sec22b	Stx1b	Tubb6	
Aifm1	Aspn	Cct3	Crmp1	Eef1g	Glg1	Hnrnpa2b1	<b>Itgav</b>	Mthfd1	Npm1	Ppib	Rap2a	Sec23a	Stxbp6	Tufm	
Ak2	Atp2a2	Cct5	<b>Ctnnb1</b>	Eif2s1	Glipr2	Hnrnpa3	<b>Itgb1</b>	Myadm	Nras	Ppic	Rap2b	Sec31a	Surf4	Txndc5	
Akap12	Atp4a	Cct6a	Cttn	Eif3b	Glr3x	Hnrnpd	Kif5a	Myh10	Nsf	Ppp1ca	Rars	Sec61a1	Syncr1p	Uba1	
Alad	Atp5f1a	Cct7	Dad1	Eif4a1	Gnai3	Hnrnpk	Kif5c	Nap11l	Ola1	Ppp1cc	Rcn3	Sec61b	Tcp1	Ube2i	
Alcam	Basp1	Cct8	Ddost	Eif4h	Gnas	Hsp90aa1	Kpnb1	Nap11l4	Otub1	Prdx2	<b>Rdx</b>	<b>Sept2</b>	Tgfb1	Ube2n	
Aldh7a1	Bax	<b>Cfi1</b>	Ddx1	Eif5a	Gnb2	Hsp90aab1	Kras	Ncam1	P4hb	Prdx4	Rpl10a	<b>Sept11</b>	Tln2	Usp5	
Anp32b	Bin1	Kcap4	<b>Dig1</b>	<b>Epb4113</b>	Gnb4	Hspa5	<b>Lama4</b>	Ncl	Pa2g4	Prkaca	Rpl31	Sept6	Tm9sf3	<b>Vcl</b>	
<b>Anxa2</b>	Bzw1	Kcap5	Dlst	Eprs	Gpd2	Hspd1	<b>Lamb1</b>	<b>Nedd4</b>	Pabpc1	Pasma1	Rpl8	Serpinh1	Tmed2	Vcp	
Ap2a2	C1qbp	Cnrp1	Dnaja1	Fabp5	Gpx7	Idh2	<b>Lamc1</b>	<b>Nefh</b>	Pafah1b2	Pasma5	Rpn1	Set	Tmed9	Vdac1	
Ap2s1	Calr	Col14a1	Dnaja2	Fam129a	Hdlbp	Ikbip	Lpp	<b>Nid1</b>	Pcyox1	Pasma7	Rps10	Slk	Tmx1	Yars	



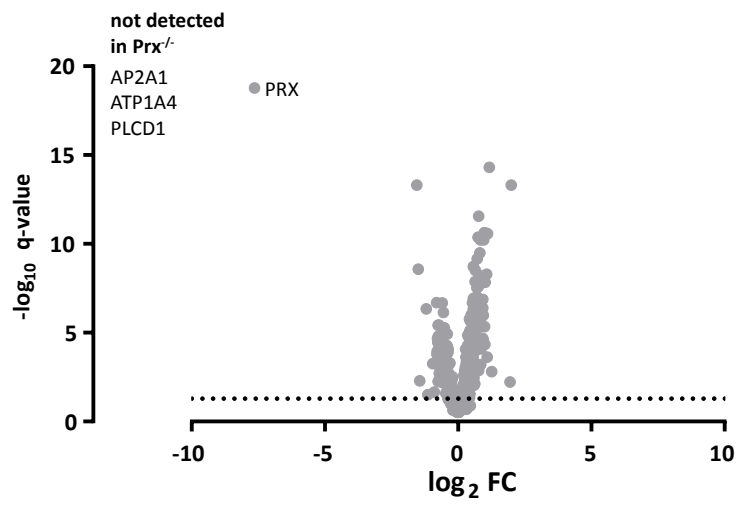


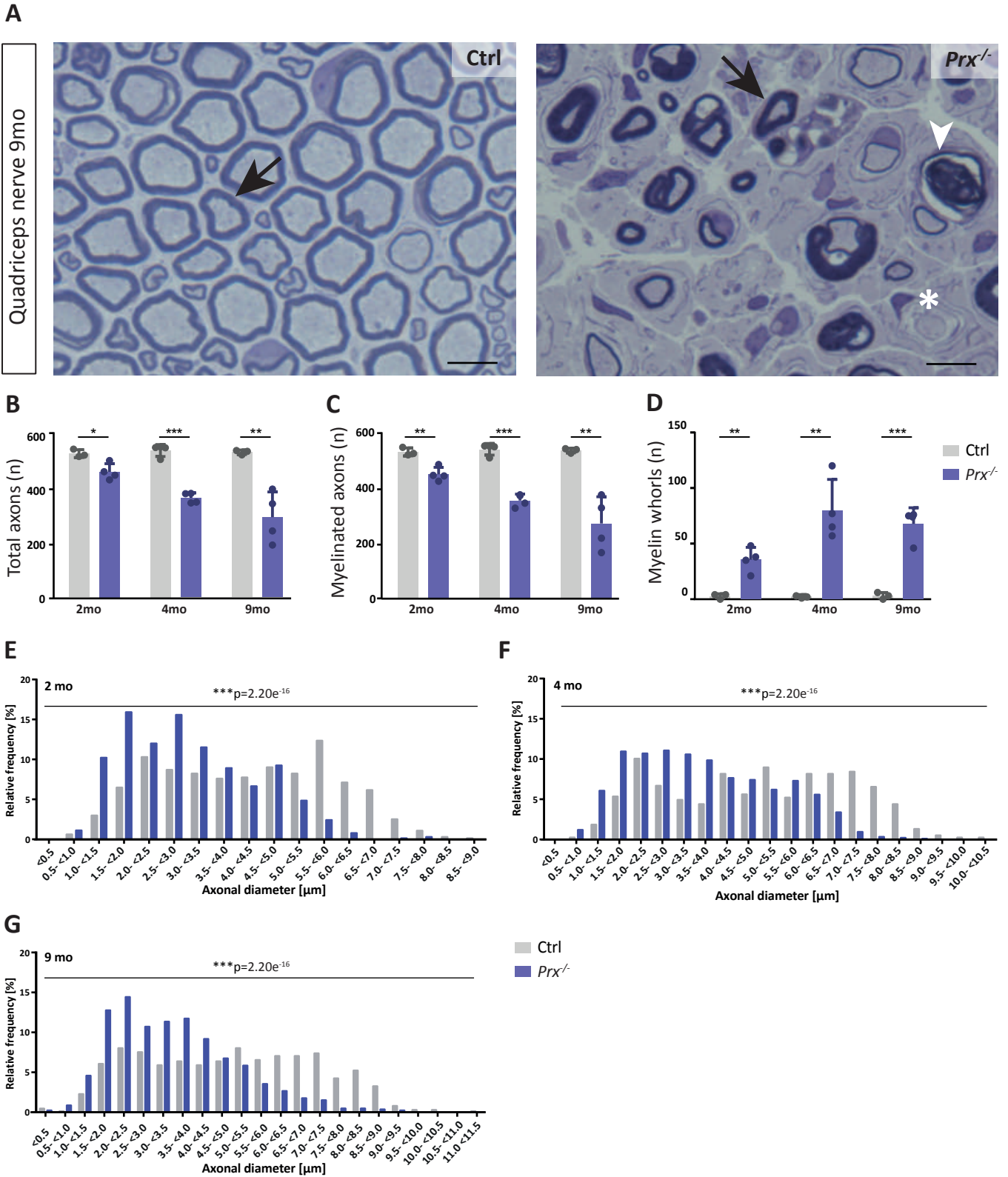


**A**



**B**





1  
2  
3  
4  
5  
6  
7  
8 **Proteome profile of peripheral myelin in healthy mice and in a neuropathy model**  
9

10  
11  
12  
13  
14  
15 Sophie B. Siems<sup>1,7</sup>, Olaf Jahn<sup>2,7</sup>, Maria A. Eichel<sup>1</sup>, Nirmal Kannaiyan<sup>3</sup>, Lai Man N. Wu<sup>4</sup>,  
16 Diane L. Sherman<sup>4</sup>, Kathrin Kusch<sup>1</sup>, Dörte Hesse<sup>2</sup>, Ramona B. Jung<sup>1</sup>, Robert Fledrich<sup>1,5</sup>,  
17 Michael W. Sereda<sup>1,6</sup>, Moritz J. Rossner<sup>3</sup>, Peter J. Brophy<sup>4</sup>, Hauke B. Werner<sup>1,\*</sup>  
18  
19  
20

21 **Affiliations**

22 <sup>1</sup>Department of Neurogenetics, Max Planck Institute of Experimental Medicine, 37075 Göttingen, Germany

23 <sup>2</sup>Proteomics Group, Max Planck Institute of Experimental Medicine, 37075 Göttingen, Germany

24 <sup>3</sup>Department of Psychiatry and Psychotherapy, University Hospital, LMU Munich, 80336 Munich, Germany

25 <sup>4</sup>Centre for Discovery Brain Sciences, University of Edinburgh, Edinburgh, EH16 4SB, UK

26 <sup>5</sup>Institute of Anatomy, University of Leipzig, 04103 Leipzig, Germany

27 <sup>6</sup>Department of Clinical Neurophysiology, University Medical Center, 37075 Göttingen, Germany

28 <sup>7</sup>These authors contributed equally to this work  
29

30 **\* Corresponding author**

31 Dr. Hauke Werner

32 Max Planck Institute of Experimental Medicine

33 Department of Neurogenetics

34 Hermann-Rein-Str. 3

35 D-37075 Göttingen, Germany

36 Tel.: +49 (551) 3899-759; Fax.: +49 (551) 3899-758

37 E-mail: [Hauke@em.mpg.de](mailto:Hauke@em.mpg.de)  
38

39 **Key words**

40 Schwann cell, peripheral nervous system (PNS), myelin proteome, neuropathy, Charcot-  
41 Marie-Tooth disease (CMT4F), periaxin (PRX), MCT1/SLC16A1, demyelination, axon  
42 degeneration, transcriptome  
43

44 **Word and figure count**

45 Abstract 149 words; Introduction/results/discussion 4786 words

46 6 main figures; 2 figure supplements; 2 main tables; 4 source data files  
47  
48

49 **ABSTRACT**

50

51 Proteome and transcriptome analyses aim at comprehending the molecular profiles of the  
52 brain, its cell-types and subcellular compartments including myelin. Despite the relevance of  
53 the peripheral nervous system for normal sensory and motor capabilities, analogous  
54 approaches to peripheral nerves and peripheral myelin have fallen behind evolving technical  
55 standards. Here we assess the peripheral myelin proteome by gel-free, label-free mass-  
56 spectrometry for deep quantitative coverage. Integration with RNA-Sequencing-based  
57 developmental mRNA-abundance profiles and neuropathy disease genes illustrates the utility  
58 of this resource. Notably, the periaxin-deficient mouse model of the neuropathy Charcot-  
59 Marie-Tooth 4F displays a highly pathological myelin proteome profile, exemplified by the  
60 discovery of reduced levels of the monocarboxylate transporter MCT1/SLC16A1 as a novel  
61 facet of the neuropathology. This work provides the most comprehensive proteome resource  
62 thus far to approach development, function and pathology of peripheral myelin, and a  
63 straightforward, accurate and sensitive workflow to address myelin diversity in health and  
64 disease.

65

66

## 67 INTRODUCTION

68

69 The ensheathment of axons with myelin enables rapid impulse propagation, a prerequisite  
70 for normal motor and sensory capabilities of vertebrates (1,2). This is illustrated by  
71 demyelinating neuropathies of the Charcot-Marie-Tooth (CMT) spectrum, in which mutations  
72 affecting myelin genes as *MPZ*, *PMP22*, *GJB1* and *PRX* impair myelin integrity and reduce  
73 the velocity of nerve conduction in the peripheral nervous system (PNS) (3).  
74 Developmentally, myelination by Schwann cells in peripheral nerves is regulated by axonal  
75 neuregulin-1 (4,5) and the basal lamina (6–8) that is molecularly linked to the abaxonal  
76 Schwann cell membrane via integrins and the dystroglycan complex (9–12). In adulthood,  
77 the basal lamina continues to enclose all axon/myelin-units (13), probably to maintain myelin.  
78 Beyond regulation by extracellular cues, myelination involves multiple proteins mediating  
79 radial sorting of axons out of Remak bundles, myelin membrane growth and layer  
80 compaction (14–18). For example, the Ig-domain containing myelin protein zero (MPZ; also  
81 termed P0) mediates adhesion between adjacent extracellular membrane surfaces in  
82 compact myelin (19). At their intracellular surfaces, myelin membranes are compacted by the  
83 cytosolic domain of MPZ/P0 together with myelin basic protein (MBP; previously termed P1)  
84 (20,21). Not surprisingly, MPZ/P0 and MBP were early identified as the most abundant  
85 peripheral myelin proteins (22,23).

86

87 A system of cytoplasmic channels through the otherwise compacted myelin sheath remains  
88 non-compacted throughout life, i.e. the adaxonal myelin layer, paranodal loops, Schmidt-  
89 Lanterman incisures (SLI), and abaxonal longitudinal and transverse bands of cytoplasm  
90 termed bands of Cajal (14,24,25). Non-compacted myelin comprises cytoplasm, cytoskeletal  
91 elements, vesicles and lipid-modifying enzymes, and thus numerous proteins involved in  
92 maintaining the myelin sheath. The cytosolic channels probably also represent transport  
93 routes toward Schwann cell-dependent metabolic support of myelinated axons (26–31).

94

95 Considering that Schwann cells constitute a major proportion of the cells in the PNS,  
96 oligonucleotide microarray analyses have been used for mRNA abundance profiling of total  
97 sciatic nerves (32,33). Indeed, these systematic approaches allowed the identification of  
98 novel myelin constituents including non-compact myelin-associated protein (NCMAP/MP11)  
99 (34). Notwithstanding that the number of known peripheral myelin proteins has grown in  
100 recent years, a comprehensive molecular inventory has been difficult to achieve because  
101 applications of systematic ('omics') approaches specifically to Schwann cells and peripheral  
102 myelin remained comparatively scarce, different from studies addressing oligodendrocytes  
103 and CNS myelin (35–40). One main reason may be that the available techniques were not

104 sufficiently straightforward for general application. For example, the protein composition of  
105 peripheral myelin was previously assessed by proteome analysis (41). However, at that time  
106 the workflow of sample preparation and data acquisition (schematically depicted in **Figure**  
107 **1A**) was very labor-intensive and required a substantial amount of input material; yet the depth  
108 of the resulting datasets remained limited. In particular, differential myelin proteome analysis  
109 by 2-dimensional fluorescence intensity gel electrophoresis (2D-DIGE) requires considerable  
110 hands-on-time and technical expertise (41,42). While this method is powerful for the  
111 separation of proteoforms (43), it typically suffers from under-representation of highly basic  
112 and transmembrane proteins. It thus allows comparing the abundance of only few myelin  
113 proteins rather than quantitatively covering the entire myelin proteome. Because of these  
114 limitations and an only modest sample-to-sample reproducibility, 2D-DIGE analysis of myelin,  
115 although unbiased, has not been commonly applied beyond specialized laboratories.

116

117 The aim of the present study was to establish a straightforward and readily applicable  
118 workflow to facilitate both comprehensive knowledge about the protein composition of  
119 peripheral myelin and systematic assessment of differences between two states, e.g.,  
120 pathological alterations in a neuropathy model. The major prerequisites were the biochemical  
121 purification of myelin, its solubilization with the detergent ASB-14 and the subsequent  
122 automated digestion with trypsin during filter-aided sample preparation (FASP). The tryptic  
123 peptides were fractionated by liquid chromatography and analyzed by mass spectrometry for  
124 gel-free, label-free quantitative proteome analysis. More specifically, we used nano-flow  
125 ultra-performance liquid chromatography (nanoUPLC) coupled to an electrospray-ionization  
126 quadrupole time-of-flight (ESI-QTOF) mass spectrometer with ion mobility option, providing  
127 an orthogonal dimension of peptide separation. The utilized data-independent acquisition  
128 (DIA) strategy relies on collecting data in an alternating low and elevated energy mode  
129 ( $MS^E$ ); it enables simultaneous sequencing and quantification of all peptides entering the  
130 mass spectrometer without prior precursor selection (reviewed in (44,45)). With their high-  
131 duty cycle utilized for the acquisition of precursor ions,  $MS^E$ -type methods are ideally suited  
132 to reliably quantify proteins based on peptide intensities. Notably, these methods do not  
133 involve the use of spectral libraries in the identification of proteins, different from other DIA  
134 strategies. Instead, the achieved high-complexity fragmentation spectra are deconvoluted  
135 before submission to dedicated search engines for peptide and protein identification (46,47).  
136 In the  $MS^E$  mode, this deconvolution involves precursor-fragment ion alignment solely on the  
137 basis of chromatographic elution profiles; on top, drift times of ion mobility-separated  
138 precursors are used in the high-definition (HD) $MS^E$  mode. An expansion of the latter referred  
139 to as the ultra-definition (UD) $MS^E$  mode, additionally implements drift time-dependent  
140 collision energy profiles for more effective precursor fragmentation (48,49).



141  
142  
143  
144  
145  
146  
147  
148  
149  
150  
151  
152

Indeed, compared to the previously used manual handling and in-gel digestion, the current workflow (schematically depicted in **Figure 1A**) is considerably less labor-intensive, and automated FASP increases sample-to-sample reproducibility. Moreover, differential analysis by quantitative mass spectrometry (MS) facilitates reproducible quantification of hundreds rather than a few distinct myelin proteins. Together, the present workflow increases the efficacy of assessing the peripheral myelin proteome while shifting the main workload from manual sample preparation and gel-separation to automated acquisition and processing of data. We propose that comprehending the expression profiles of all myelin proteins in the healthy PNS and in myelin-related disorders can contribute to advancing our understanding of the physiology and pathophysiology of peripheral nerves.

## 153 RESULTS

154

### 155 Purification of peripheral myelin

156 We biochemically enriched myelin as a light-weight membrane fraction from pools of sciatic  
157 nerves dissected from mice at postnatal day 21 (P21) using an established protocol of  
158 discontinuous sucrose density gradient centrifugation (41,50), in which myelin membranes  
159 accumulate at the interface between 0.29 and 0.85 M sucrose. By immunoblotting, proteins  
160 specific for both compact (MPZ/P0, MBP, PMP2) and non-compact (PRX) myelin were  
161 substantially enriched in the myelin fraction compared to nerve lysates (**Figure 1B**).  
162 Conversely, axonal (NEFH, KCNA1) and mitochondrial (VDAC) proteins and a marker for the  
163 Schwann cell nucleus (KROX20/EGR2) were strongly reduced in purified myelin. Together,  
164 these results imply that biochemically purified peripheral myelin is suitable for systematic  
165 analysis of its protein composition.

166

### 167 Proteome analysis of peripheral myelin

168 It has long been difficult to accurately quantify the most abundant myelin proteins both in the  
169 CNS (PLP, MBP, CNP (51)) and the PNS (MPZ/P0, MBP, PRX; this work), probably owing to  
170 their exceptionally high relative abundance. For example, the major CNS myelin constituents  
171 PLP, MBP and CNP comprise 17, 8 and 4% of the total myelin protein, respectively (51). We  
172 have recently provided proof of principle (52) that the mass spectrometric quantification of  
173 these high-abundant myelin proteins is accurate and precise when data are acquired in the  
174 MS<sup>E</sup> data acquisition mode and proteins are quantified according to the TOP3 method, i.e. if  
175 their abundance values are obtained based on the proven correlation between the average  
176 intensity of the three peptides exhibiting the most intense mass spectrometry response and  
177 the absolute amount of their source protein (53,54). Using data acquisition by MS<sup>E</sup> we  
178 confirmed that CNP constitutes about 4% of the total CNS myelin proteome and that the  
179 abundance of CNP in myelin from mice heterozygous for the *Cnp* gene (*Cnp*<sup>WT/null</sup>) compared  
180 to wild-type mice is 50.7% ( $\pm 0.4\%$ ), in agreement with the halved gene dosage and gel-  
181 based quantification by silver staining or immunoblotting (52).

182

183 When applying the MS<sup>E</sup> mode to PNS myelin, we quantified 351 proteins with a false  
184 discovery rate (FDR) of <1% at peptide and protein level and an average sequence coverage  
185 of 35.5% (**Figure 1-source data 1**). While MS<sup>E</sup> (labeled in orange in **Figure 1C**) indeed  
186 provided a dynamic range of more than four orders of magnitude and thus quantitatively  
187 covered the exceptionally abundant myelin proteins MPZ/P0, MBP and PRX, the number of  
188 quantified proteins appeared limited when spectral complexity was deconvoluted solely on  
189 the basis of chromatographic elution profiles. Accordingly, by using the UDMS<sup>E</sup> mode, which

190 comprises ion mobility for additional peptide separation as well as drift time-specific collision  
191 energies for peptide fragmentation, proteome coverage was increased about three-fold (1078  
192 proteins quantified; average sequence coverage 34.3%; **Figure 1-source data 1**). However,  
193 the dynamic range of UDMS<sup>E</sup> (labeled in blue in **Figure 1C**) was found to be somewhat  
194 compressed compared to that of MS<sup>E</sup>, which can be considered an expectable feature of  
195 traveling wave ion mobility devices (55), where the analysis of pulsed ion packages leads to  
196 a temporal and spatial binning of peptides during ion mobility separation. Indeed, this  
197 manifests as a ceiling effect for the detection of exceptionally intense peptide signals, which  
198 results in an underestimation of the relative abundance of MPZ/P0, MBP and PRX by  
199 UDMS<sup>E</sup>.

200

201 The complementary nature of the MS<sup>E</sup> and UDMS<sup>E</sup> data acquisition modes led us to  
202 conclude that a comprehensive analysis of the myelin proteome that facilitates both correct  
203 quantification of the most abundant proteins and deep quantitative coverage of the proteome  
204 would require analyzing the same set of samples with two different instrument settings for  
205 MS<sup>E</sup> and UDMS<sup>E</sup>, respectively. Considering that instrument time is a bottleneck for the  
206 routine differential proteome analysis of myelin from mutant mice, we aimed to combine the  
207 strengths of MS<sup>E</sup> and UDMS<sup>E</sup> into a single data acquisition mode. Based on a gene ontology  
208 enrichment analysis for cellular components of the 200 proteins of highest and lowest  
209 abundance from the UDMS<sup>E</sup> dataset, we realized that the 'bottom' of the quantified proteome  
210 is probably largely unrelated to myelin but dominated by contaminants from other subcellular  
211 sources including mitochondria. We thus reasoned that for a myelin-directed data acquisition  
212 mode, proteome depth may be traded in for a gain in dynamic range and devised a novel  
213 method referred to as dynamic range enhancement (DRE)-UDMS<sup>E</sup>, in which a deflection lens  
214 is used to cycle between full and reduced ion transmission during mass spectrometric  
215 scanning. Indeed, DRE-UDMS<sup>E</sup> quantified an intermediate number of proteins in PNS myelin  
216 (554 proteins; average sequence coverage 30.6%; **Figure 1-source data 1**) while providing  
217 an intermediate dynamic range (labeled in green in **Figure 1C**). We thus consider DRE-  
218 UDMS<sup>E</sup> as the data acquisition mode of choice most suitable for routine differential myelin  
219 proteome profiling (see below).

220

221 Overall, we found a high reproducibility between replicates and even among the different  
222 data acquisition modes as indicated by Pearson's correlation coefficients for protein  
223 abundance in the range of 0.765-0.997 (**Figure 1-supplement 1**). When comparing the  
224 proteins identified in PNS myelin using the three data acquisition modes, we found a very  
225 high overlap (**Figure 1D**). We also found a high overlap (**Figure 1E**) between the proteins  
226 identified in the present study by UDMS<sup>E</sup> and those detected in previous proteomic

227 approaches to PNS myelin (41,42), thus allowing a high level of confidence. Together, the  
228 three data acquisition modes exhibit distinct strengths in the efficient quantification of  
229 exceptionally abundant proteins (MS<sup>E</sup>), establishing a comprehensive inventory (UDMS<sup>E</sup>)  
230 and gel-free, label-free differential analysis of hundreds of distinct proteins (DRE-UDMS<sup>E</sup>) in  
231 peripheral myelin (see **Figure 1A**). Yet, analyzing the same set of samples by different  
232 modes may not always be feasible in all routine applications when considering required  
233 instrument time.

234

### 235 **Relative abundance of peripheral myelin proteins**

236 Considering that MS<sup>E</sup> provides the high dynamic range required for the quantification of the  
237 most abundant myelin proteins, we calculated the relative abundance of the 351 proteins  
238 identified in myelin by MS<sup>E</sup> (**Figure 1-source data 1**). According to quantitative assessment  
239 of this dataset, the most abundant PNS myelin protein, myelin protein zero (MPZ/P0),  
240 constitutes 44% (+/-4% relative standard deviation (RSD)) of the total myelin protein (**Figure**  
241 **2**). Myelin basic protein (MBP), periaxin (PRX) and tetraspanin-29 (CD9) constitute 18% (+/-  
242 1% RSD), 15% (+/-1%) and 1% (+/-0.2%) of the total myelin protein, respectively (**Figure 2**).  
243 For MPZ/P0 and MBP, our quantification by MS<sup>E</sup> is in agreement with but specifies prior  
244 estimations upon gel-separation and protein labeling by Sudan-Black, Fast-Green or  
245 Coomassie-Blue, in which they were judged to constitute 45–70% and 2–26% of the total  
246 myelin protein, respectively (22,56–58). However, gel-based estimates of the relative  
247 abundance of myelin proteins were not very precise with respect to many other proteins,  
248 including those of high molecular weight. Indeed, periaxin was identified as a constituent of  
249 peripheral myelin after the advent of gradient SDS-PAGE gels (59), which allowed improved  
250 migration of large proteins into gels. The present MS<sup>E</sup>-based quantification of myelin proteins  
251 also extends beyond and partially adjusts an earlier mass spectrometric approach (41).  
252 Indeed, the current approach identified and quantified more myelin proteins, probably owing  
253 to improved protein solubilization during sample preparation and higher dynamic range of the  
254 used mass spectrometer. By MS<sup>E</sup>, known myelin proteins (**Table 1**) collectively constitute  
255 over 85% of the total myelin protein (**Figure 2**) while proteins not yet associated with myelin  
256 account for the remaining 15% of the total myelin protein.

257

### 258 **Comprehensive compendium and comparison to the transcriptome**

259 To systematically elucidate the developmental abundance profiles of the transcripts that  
260 encode peripheral myelin proteins (**Figure 3**), we used our combined proteome inventory of  
261 peripheral myelin (**Figure 1-source data 1**) to filter mRNA abundance data of all genes  
262 expressed in sciatic nerves. By this strategy, **Figure 3** displays only those transcripts of  
263 which the protein product was identified in peripheral myelin rather than all transcripts in the

264 nerve, thereby discriminating myelin-related mRNAs from other mRNAs such as those  
265 present in peripheral axons, fibroblasts, immune cells etc. In this assessment we additionally  
266 included PMP22 although it was not detected by MS as well as 45 proteins exclusively  
267 identified by LC-MS of myelin separated by SDS-PAGE (**Figure 1-source data 1**). For  
268 mRNA abundance profiles, we exploited a recently established RNA sequencing analysis  
269 (RNA-Seq; platform Illumina HiSeq 2000) of sciatic nerves dissected from wild type Sprague  
270 Dawley rats at embryonic day 21 (E21), P6, P18 and 6 months (60). RNA-Seq provides  
271 reliable information about the relative abundance of all significantly expressed genes and is  
272 thus not limited to those represented on the previously used oligonucleotide microarrays  
273 (41). The raw data (accessible under GEO accession number GSE115930) were normalized  
274 (**Figure 3-source data 1**) and standardized. When comparing the proteome and  
275 transcriptome datasets, significant mRNA abundance was detected for all 1046 transcripts  
276 for which an unambiguous unique gene identifier was found (**Figure 3**). 126 transcripts  
277 displayed developmentally unchanged abundance levels, i.e., abundance changes below a  
278 threshold of 10% coefficient of variation (**Figure 3B; Figure 3-source data 1**).

279  
280 By fuzzy c-means clustering, those 920 transcripts that showed developmental abundance  
281 changes were grouped into 5 clusters (**Figure 3A; Figure 3-source data 1**). Among those,  
282 one cluster corresponds to an mRNA-abundance peak coinciding with an early phase of  
283 myelin biogenesis (cluster 'P6-UP'), which includes the highest proportion of known myelin  
284 proteins (**Table 1**) such as MPZ/P0, MBP, PRX, cyclic nucleotide phosphodiesterase (CNP),  
285 fatty acid synthase (FASN), myelin-associated glycoprotein (MAG), proteolipid protein  
286 (PLP/DM20), cell adhesion molecule-4 (CADM4/NECL4), connexin-29 (GJC3), claudin-19  
287 (CLDN19) and CKLF-like MARVEL-transmembrane domain containing protein-5 (CMTM5).  
288 However, many known myelin proteins clustered together according to their mRNA-  
289 abundance peak coinciding with a later phase of myelination (cluster 'P18-UP'), including  
290 peripheral myelin protein 2 (PMP2), tetraspanin-29 (CD9), tetraspanin-28 (CD81), connexin-  
291 32 (GJB1), plasmalipin (PLLP), junctional adhesion molecule-3 (JAM3), CD59 and  
292 dystrophin-related protein-2 (DRP2). The proportion of known myelin proteins was lower in  
293 the clusters corresponding to mRNA-abundance peaks in adulthood (clusters 'late-UP', 'U-  
294 shaped'). Yet, a considerable number of transcripts displayed abundance peaks at the  
295 embryonic time-point (cluster 'Descending'), including carbonic anhydrase 2 (CA2), cofilin-1  
296 CFL1), tubulin beta-4 (TUBB4b) and band 4.1-protein B (EPB41L3). Generalized, the  
297 clusters were roughly similar when comparing previous oligonucleotide microarray analysis  
298 of mouse sciatic nerves (41) and the RNA-Seq analysis of rat sciatic nerves (this study); yet,  
299 the latter provides information on a larger number of genes and with a higher level of

300 confidence. Together, clustering of mRNA abundance profiles allows categorizing peripheral  
301 myelin proteins into developmentally co-regulated groups.

302

303 When systematically assessing the proteins identified in myelin by gene ontology (GO)-term  
304 analysis, the functional categories over-represented in the entire myelin proteome included  
305 cell adhesion, cytoskeleton and extracellular matrix (labeled in turquoise in **Figure 4**). When  
306 analyzing the clusters of developmentally co-expressed transcripts (from **Figure 3**), proteins  
307 associated with the lipid metabolism were particularly enriched in the P6-UP and P18-UP  
308 clusters, while those associated with the extracellular matrix (ECM) were over-represented in  
309 the U-shaped and Descending clusters (**Figure 4**). For comparison, known myelin proteins  
310 (**Table 1**) were over-represented in the P6-UP and P18-UP clusters (**Figure 4**). Together,  
311 our proteome dataset provides comprehensive in-depth coverage of the protein constituents  
312 of peripheral myelin purified from the sciatic nerves of wild type mice, and comparison to the  
313 transcriptome allows identifying developmentally co-regulated and functional groups of  
314 myelin proteins. Our data thus supply a solid resource for the molecular characterization of  
315 myelin and for discovering functionally relevant myelin proteins.

316

### 317 **Neuropathy genes encoding myelin proteins**

318 Heritable neuropathies can be caused by mutations affecting genes preferentially expressed  
319 in neurons, Schwann cells or both (3,61–63). To systematically assess which neuropathy-  
320 causing genes encode peripheral myelin proteins, we compared our myelin proteome  
321 dataset with a current overview about disease genes at the NIH National Library of Medicine  
322 at <https://ghr.nlm.nih.gov/condition/charcot-marie-tooth-disease#genes>. Indeed, 31 myelin  
323 proteins were identified to be encoded by a proven neuropathy gene (**Table 2**), a  
324 considerable increase compared to eight disease genes found in a similar previous approach  
325 (41). Notably, this increase is owing to both the larger size of the current myelin proteome  
326 dataset (**Figure 1E**) and the recent discovery of numerous neuropathy genes by the  
327 widespread application of next generation sequencing.

328

### 329 **Pathological proteomic profile of peripheral myelin in a neuropathy model**

330 The results presented thus far were based on analyzing myelin of healthy wild type mice; yet  
331 we also sought to establish a straightforward method to systematically assess myelin  
332 diversity, as exemplified by alterations in a pathological situation. As a model we chose mice  
333 carrying a homozygous deletion of the periaxin gene (*Prx*<sup>-/-</sup>) (26,64). Periaxin (PRX) is the  
334 third-most abundant peripheral myelin protein (**Figure 2**) and scaffolds the dystroglycan  
335 complex in Schwann cells. *Prx*<sup>-/-</sup> mice represent an established model of Charcot-Marie-  
336 Tooth disease type 4F (65–67). Aiming to assess the myelin proteome, we purified myelin

337 from pools of sciatic nerves dissected from *Prx*<sup>-/-</sup> and control mice at P21. Upon SDS-PAGE  
338 separation and silver staining the band patterns appeared roughly similar (**Figure 5A**), with  
339 the most obvious exception of the absence of the high-molecular weight band constituted by  
340 periaxin in *Prx*<sup>-/-</sup> myelin. Yet, several other bands also displayed genotype-dependent  
341 differences in intensity. As expected, PRX was also undetectable by MS<sup>E</sup> in *Prx*<sup>-/-</sup> myelin, in  
342 which most of the total myelin protein was constituted by MPZ/P0 and MBP (**Figure 5B**;  
343 **Figure 5-source data 1**).

344  
345 Upon differential analysis by DRE-UDMS<sup>E</sup> (**Figure 5-source data 2**), multiple proteins  
346 displayed genotype-dependent differences as visualized in a heatmap displaying those 40  
347 proteins of which the abundance was reduced or increased with the highest statistical  
348 significance in *Prx*<sup>-/-</sup> compared to control myelin (**Figure 5C**). For example, the abundance of  
349 the periaxin-associated dystrophin-related protein 2 (DRP2) was strongly reduced in *Prx*<sup>-/-</sup>  
350 myelin, as previously shown by immunoblotting (9). Notably, the abundance of multiple other  
351 proteins was also significantly reduced in *Prx*<sup>-/-</sup> myelin, including the extracellular matrix  
352 protein laminin C1 (LAMC1; previously termed LAMB2), the laminin-associated protein  
353 nidogen (NID1), Ig-like cell adhesion molecules (CADM4, MAG), the desmosomal junction  
354 protein desmin (DES), cytoskeletal and cytoskeleton-associated proteins (EPB41L3, MAP1A,  
355 CORO1A, SPTBN1, various microtubular and intermediate filament monomers), the  
356 monocarboxylate transporter MCT1 (also termed SLC16A1) and the MCT1-associated (68)  
357 immunoglobulin superfamily protein basigin (BSG, also termed CD147). On the other hand,  
358 proteins displaying the strongest abundance increase in *Prx*<sup>-/-</sup> myelin included immune-  
359 related proteins (LGALS3, LYZZ2, CTSD), cytoskeletal and cytoskeleton-associated proteins  
360 (CAPG, CORO1C, CNN3, several myosin heavy chain subunits), peroxisomal enzymes  
361 (CAT, HSD17B4, MDH1) and known myelin proteins (PLLP/plasmolipin, CRYAB,  
362 GJB1/CX32). For comparison, the abundance of the marker proteolipid protein (PLP/DM20)  
363 (69) and the periaxin-associated integrin beta-4 (ITGB4) (12) in myelin was unaltered in *Prx*<sup>-/-</sup>  
364 myelin. Together, differential proteome analysis finds considerably more proteins and protein  
365 groups to be altered in *Prx*<sup>-/-</sup> myelin than previously known (**Figure 5C, D-D''**), probably  
366 reflecting the complex pathology observed in this model (26,64).

367  
368 The monocarboxylate transporter MCT1/SLC16A1 expressed by myelinating  
369 oligodendrocytes (70,71) and Schwann cells (28,72) has been proposed to supply lactate or  
370 other glucose breakdown products to axons, in which they may serve as substrate for the  
371 mitochondrial production of ATP (73–75). In this respect it was striking to find the abundance  
372 of MCT1 significantly reduced in peripheral myelin when PRX is lacking (**Figure 5C**), a result  
373 that we were able to confirm by immunoblotting (**Figure 5E**) and immunolabeling of teased

374 fiber preparations of sciatic nerves (**Figure 5F**). Notably, reduced expression of MCT1 in  
375 *Slc16a1<sup>+/-</sup>* mice impairs axonal integrity at least in the CNS (70,76). The reduced abundance  
376 of MCT1 thus represents an interesting novel facet of the complex pathology in *Prx<sup>-/-</sup>* mice.  
377 Considering that the integrity of peripheral axons may be impaired in *Prx<sup>-/-</sup>* mice, we  
378 assessed their quadriceps nerves. Indeed, *Prx<sup>-/-</sup>* mice displayed reduced axonal diameters, a  
379 progressively reduced total number of axons and a considerable number of myelin whorls  
380 lacking a visible axon (**Figure 6**), indicative of impaired axonal integrity (77). Yet we note that  
381 molecular or neuropathological features other than the reduced abundance of MCT1  
382 probably also contribute to the axonopathy in *Prx<sup>-/-</sup>* mice.

383

384 Together, gel-free, label free proteome analysis provides a cost- and time-efficient method  
385 that provides an accurate, sensitive tool to gain systematic insight into the protein  
386 composition of healthy peripheral myelin and its alterations in pathological situations. Indeed,  
387 gel-free proteome analysis is particularly powerful and comprehensive compared to 2D-  
388 DIGE; the workflow presented here appears readily applicable to other neuropathy models,  
389 thereby promising discovery of relevant novel features of their neuropathology.

390

391



## 392 DISCUSSION

393

394 We used [gel-free](#), [label-free](#) quantitative mass spectrometry to assess the protein  
395 composition of myelin biochemically purified from the sciatic nerves of wild-type mice,  
396 thereby establishing a straightforward and readily applicable workflow to approach the  
397 peripheral myelin proteome. The key to comprehensiveness was to combine the strengths of  
398 three data acquisition modes, i.e., MS<sup>E</sup> for correct quantification of high-abundant proteins,  
399 UDMS<sup>E</sup> for deep quantitative proteome coverage including low-abundant proteins and DRE-  
400 UDMS<sup>E</sup> for differential analysis. We suggest that DRE-UDMS<sup>E</sup> provides a good compromise  
401 between dynamic range, identification rate and instrument run time for routine differential  
402 myelin proteome profiling as a prerequisite for a molecular understanding of myelin  
403 (patho)biology. We have also integrated the resulting compendium with RNA-Seq-based  
404 mRNA abundance profiles in peripheral nerves and neuropathy disease loci. Beyond  
405 providing the largest peripheral myelin proteome dataset thus far, the workflow is appropriate  
406 to serve as starting point for assessing relevant variations of myelin protein composition, e.g.,  
407 in different nerves, ages, species and in pathological conditions. The identification of  
408 numerous pathological alterations of myelin protein composition in the *Prx*<sup>-/-</sup> neuropathy  
409 model indicates that the method is well suited to assess such diversity.

410

411 Aiming to understand nervous system function at the molecular level, multiple 'omics'-scale  
412 projects assess the spatio-temporal expression profiles of all mRNAs and proteins in the  
413 CNS including oligodendrocytes and myelin (35–39). Yet, peripheral nerves are also  
414 essential for normal sensory and motor capabilities. Prior approaches to the molecular  
415 profiles of Schwann cells and PNS myelin thus far, however, were performed >8 years ago  
416 (32–34,41,78–80), and the techniques have considerably advanced since. For example,  
417 current gel-free, label-free mass spectrometry can simultaneously identify and quantify the  
418 vast majority of proteins in a sample, thereby providing comprehensive in depth-information.  
419 Moreover, RNA-Seq technology has overcome limitations of the previously used microarrays  
420 for characterizing mRNA abundance profiles with respect to the number of represented  
421 genes and the suitability of the oligonucleotide probes. The present compendium thus  
422 provides high confidence with respect to the identification of myelin proteins, their relative  
423 abundance and their developmental mRNA expression profiles. This view is supported by the  
424 finding that over 80% of the total myelin proteome is constituted by approximately 50  
425 previously known myelin proteins. We believe that the majority of the other identified proteins  
426 represent low-abundant myelin-associated constituents in line with the high efficiency of  
427 biochemical myelin purification. Doubtless, however, the myelin proteome also comprises

428 contaminants from other cellular sources, underscoring the need of independent validation  
429 for establishing newly identified constituents as true myelin proteins.

430

431 Do myelin proteins exist that escape identification by standard proteomic approaches?  
432 Indeed, some proteins display atypically distributed lysine and arginine residues, which  
433 represent the cleavage sites of the commonly used protease trypsin. The tryptic digest of  
434 these proteins leads to peptides that are not well suited for chromatographic separation  
435 and/or mass spectrometric detection/sequencing, as exemplified by the small hydrophobic  
436 tetraspan-transmembrane myelin proteins MAL (81) and PMP22 (82). We can thus not  
437 exclude that additional proteins with atypical tryptic digest patterns exist in peripheral myelin,  
438 which would need to be addressed by the use of alternative proteases. Moreover, potent  
439 signaling molecules including erbB receptor tyrosine kinases (83,84) and G-protein coupled  
440 receptors (GPRs) (85–87) display exceptionally low abundance. Such proteins may be  
441 identified when applying less stringent identification criteria, e.g., by requiring the sequencing  
442 of only one unique peptide per protein. However, lower stringency would also result in  
443 identifying false-positive proteins, which we wished to avoid for the purpose of the present  
444 compendium. We note that a truly comprehensive spatio-temporally resolved myelin  
445 proteome should preferentially also include systematic information about protein isoforms  
446 and post-translational modifications, which still poses technical challenges.

447

448 Mutations affecting the periaxin (*PRX*) gene in humans cause CMT type 4F (65,88–90); the  
449 neuropathology resulting from mutations affecting periaxin has been mainly investigated in  
450 the *Prx*<sup>-/-</sup> mouse model. Indeed, *Prx*<sup>-/-</sup> mice display a progressive peripheral neuropathy  
451 including axon/myelin-units with abnormal myelin thickness, demyelination, tomaculae, onion  
452 bulbs, reduced nerve conduction velocity (64), reduced abundance and mislocalization of the  
453 periaxin-associated DRP2 (9) and reduced internode length (26). Absence of SLIs (64) and  
454 bands of Cajal (26) imply that the non-compact myelin compartments are impaired when  
455 PRX is lacking. In the differential analysis of myelin purified from *Prx*<sup>-/-</sup> and control mice we  
456 find that the previously reported reduced abundance of DRP2 (9) represents one of the  
457 strongest molecular changes in the myelin proteome when PRX is lacking. Notably, the  
458 reported morphological changes in this neuropathy model (9,26,64) go along with alterations  
459 affecting the abundance of multiple other myelin-associated proteins, including junctional,  
460 cytoskeletal, extracellular matrix and immune-related proteins as well as lipid-modifying  
461 enzymes. Thus, the neuropathology in *Prx*<sup>-/-</sup> mice at the molecular level is more complex  
462 than previously anticipated. It is striking that the abundance of the monocarboxylate  
463 transporter MCT1/SLC16A1 that may contribute to the metabolic supply of lactate from  
464 myelinating cells to axons (27–31) is strongly reduced in *Prx*<sup>-/-</sup> myelin. Considering that

465 MCT1 in Schwann cells mainly localizes to Schmidt Lanterman incisures (SLI) (28) and that  
466 SLI are largely absent from myelin when PRX is lacking (64), the reduced abundance of  
467 MCT1 in *Prx*<sup>-/-</sup> myelin may be a consequence of the impaired myelin ultrastructure. Yet,  
468 considering that SLI are part of the cytosolic channels that may represent transport routes  
469 toward Schwann cell-dependent metabolic support of myelinated axons, the diminishment of  
470 MCT1 may contribute to reduced axonal diameters or axonal loss in *Prx*<sup>-/-</sup> mice, probably in  
471 conjunction with other molecular or morphological defects. Together, the in depth-analysis of  
472 proteins altered in neuropathy models can contribute to an improved understanding of nerve  
473 pathophysiology.

474

475 Compared to a previous approach (41), the number of proven neuropathy genes of which the  
476 encoded protein is mass spectrometrically identified in peripheral myelin has increased four-  
477 fold from eight to 32 in the present study. This reflects both that the number of proteins  
478 identified in myelin has approximately doubled and that more neuropathy genes are known  
479 due to the common use of genome sequencing. We note that our compendium comprises  
480 not only myelin-associated proteins causing (when mutated) demyelinating CMT1 (e.g.,  
481 MPZ/P0, NEFL, PMP2) or intermediate CMT4 (GDAP1, NDRG1, PRX) but also axonal  
482 CMT2 (RAB7, GARS, HSPB1). Yet, the expression of genes causative of CMT2 is not  
483 necessarily limited to neurons, as exemplified by the classical myelin protein MPZ/P0.  
484 Indeed, a subset of *MPZ*-mutations causes axonal CMT2I or CMT2J (91–95), probably  
485 reflecting impaired axonal integrity as consequence of a mutation primarily affecting  
486 Schwann cells. We also note that the nuclear *EGR2/KROX20* causative of demyelinating  
487 CMT1D has not been mass spectrometrically identified in myelin, reflecting that Schwann cell  
488 nuclei are efficiently removed during myelin purification.

489

490 While morphological analysis of peripheral nerves by light and electron microscopy is routine  
491 in numerous laboratories, systematic molecular analysis has been less straightforward.  
492 Using the sciatic nerve as a model, we show that systematic assessment of the myelin  
493 proteome and the total nerve transcriptome are suited to determine comprehensive  
494 molecular profiles in healthy nerves and in myelin-related disorders. Myelin proteome  
495 analysis can thus complement transcriptome analysis in assessing development, function  
496 and pathophysiology of peripheral nerves.

497

498 **MATERIALS AND METHODS**

499

500 **Mouse models**

501 *Prx*<sup>-/-</sup> mice (64) were kept on c57Bl/6 background in the animal facility of the University of  
502 Edinburgh (United Kingdom). Genotyping was by PCR on genomic DNA using the forward  
503 primers 5'-CAGATTTGCT CTGCCCAAGT and 5'-CGCCTTCTAT CGCCTTCTTGAC in  
504 combination with reverse primer 5'-ATGCCCTCAC CCACTAACAG. The PCR yielded a 0.5  
505 kb fragment for the wildtype allele and a 0.75 kb product for the mutant allele. The age of  
506 experimental animals is given in the figure legends. All animal work conformed to United  
507 Kingdom legislation (Scientific Procedures) Act 1986 and to the University of Edinburgh  
508 Ethical Review Committee policy; Home Office project license No. P0F4A25E9.

509

510 **Myelin purification**

511 A light-weight membrane fraction enriched for myelin was purified from sciatic nerves of mice  
512 by sucrose density centrifugation and osmotic shocks as described (41,52). Myelin  
513 accumulates at the interface between 0.29 and 0.85 M sucrose. *Prx*<sup>-/-</sup> and wild type control  
514 C57Bl/6 mice were sacrificed by cervical dislocation at postnatal day 21 (P21). For each  
515 genotype, myelin was purified as three biological replicates (n=3); each biological replicate  
516 representing a pool of 20 sciatic nerves dissected from 10 mice. Protein concentration was  
517 determined using the DC Protein Assay Kit (Bio-Rad).

518

519 **Filter-aided sample preparation for proteome analysis**

520 Protein fractions corresponding to 10 µg myelin protein were dissolved and processed  
521 according to a filter-aided sample preparation (FASP) protocol essentially as previously  
522 described for synaptic protein fractions (96) and as adapted to CNS myelin (52,97). Unless  
523 stated otherwise, all steps were automated on a liquid-handling workstation equipped with a  
524 vacuum manifold (Freedom EVO 150, Tecan) by using an adaptor device constructed in-  
525 house. Briefly, myelin protein samples were lysed and reduced in lysis buffer (7 M urea, 2 M  
526 thiourea, 10 mM DTT, 0.1 M Tris pH 8.5) containing 1% ASB-14 by shaking for 30 min at  
527 37°C. Subsequently, the sample was diluted with ~10 volumes lysis buffer containing 2%  
528 CHAPS to reduce the ASB-14 concentration and loaded on centrifugal filter units (30 kDa  
529 MWCO, Merck Millipore). After removal of the detergents by washing twice with wash buffer  
530 (8 M urea, 10 mM DTT, 0.1 M Tris pH 8.5), proteins were alkylated with 50 mM  
531 iodoacetamide in 8 M urea, 0.1 M Tris pH 8.5 (20 min at RT), followed by two washes with  
532 wash buffer to remove excess reagent. Buffer was exchanged by washing three times with  
533 50 mM ammonium bicarbonate (ABC) containing 10 % acetonitrile. After three additional  
534 washes with 50 mM ABC/10% acetonitrile, which were performed by centrifugation to ensure

535 quantitative removal of liquids potentially remaining underneath the ultrafiltration membrane,  
536 proteins were digested overnight at 37°C with 400 ng trypsin in 40 µl of the same buffer.  
537 Tryptic peptides were recovered by centrifugation followed by two additional extraction steps  
538 with 40 µl of 50 mM ABC and 40 µl of 1% trifluoroacetic acid (TFA), respectively. Aliquots of  
539 the combined flow-throughs were spiked with 10 fmol/µl of yeast enolase-1 tryptic digest  
540 standard (Waters Corporation) for quantification purposes and directly subjected to analysis  
541 by liquid chromatography coupled to electrospray mass spectrometry (LC-MS). A pool of all  
542 samples was injected at least before and after any sample set to monitor stability of  
543 instrument performance.

544

#### 545 **Mass spectrometry**

546 Nanoscale reversed-phase UPLC separation of tryptic peptides was performed with a  
547 nanoAcquity UPLC system equipped with a Symmetry C18 5 µm, 180 µm × 20 mm trap  
548 column and a HSS T3 C18 1.8 µm, 75 µm × 250 mm analytical column (Waters Corporation)  
549 maintained at 45°C. Injected peptides were trapped for 4 min at a flow rate of 8 µl/min 0.1%  
550 TFA and then separated over 120 min at a flow rate of 300 nl/min with a gradient comprising  
551 two linear steps of 3-35% mobile phase B in 105 min and 35-60% mobile phase B in 15 min,  
552 respectively. Mobile phase A was water containing 0.1% formic acid while mobile phase B  
553 was acetonitrile containing 0.1% formic acid. Mass spectrometric analysis of tryptic peptides  
554 was performed using a Synapt G2-S quadrupole time-of-flight mass spectrometer equipped  
555 with ion mobility option (Waters Corporation). Positive ions in the mass range  $m/z$  50 to 2000  
556 were acquired with a typical resolution of at least 20,000 FWHM (full width at half maximum)  
557 and data were lock mass corrected post-acquisition. UDMS<sup>E</sup> and DRE-UDMS<sup>E</sup> analyses  
558 were performed in the ion mobility-enhanced data-independent acquisition mode with drift  
559 time-specific collision energies as described in detail by Distler et al. (48,49). Specifically, for  
560 DRE-UDMS<sup>E</sup> a deflection device (DRE lens) localized between the quadrupole and the ion  
561 mobility cell of the mass spectrometer was cycled between full (100% for 0.4 sec) and  
562 reduced (5% for 0.4 sec) ion transmission during one 0.8 sec full scan. Continuum LC-MS  
563 data were processed for signal detection, peak picking, and isotope and charge state  
564 deconvolution using Waters ProteinLynx Global Server (PLGS) version 3.0.2 (47). For  
565 protein identification, a custom database was compiled by adding the sequence information  
566 for yeast enolase 1 and porcine trypsin to the UniProtKB/Swiss-Prot mouse proteome and by  
567 appending the reversed sequence of each entry to enable the determination of false  
568 discovery rate (FDR). Precursor and fragment ion mass tolerances were automatically  
569 determined by PLGS 3.0.2 and were typically below 5 ppm for precursor ions and below 10  
570 ppm (root mean square) for fragment ions. Carbamidomethylation of cysteine was specified  
571 as fixed and oxidation of methionine as variable modification. One missed trypsin cleavage

572 was allowed. Minimal ion matching requirements were two fragments per peptide, five  
573 fragments per protein, and one peptide per protein. The FDR for protein identification was set  
574 to 1% threshold.

575

### 576 **Analysis of proteomic data**

577 For each genotype (*Prx*<sup>-/-</sup> and wild type control mice sacrificed at P21), biochemical fractions  
578 enriched for PNS myelin were analyzed as three biological replicates (n=3 per condition);  
579 each biological replicate representing a pool of 20 sciatic nerves dissected from 10 mice. The  
580 samples were processed with replicate digestion and injection, resulting in four technical  
581 replicates per biological replicate and thus a total of 12 LC-MS runs per condition to be  
582 compared, essentially as previously reported for CNS myelin (36,97). The freely available  
583 software ISOQuant ([www.isoquant.net](http://www.isoquant.net)) was used for post-identification analysis including  
584 retention time alignment, exact mass and retention time (EMRT) and ion mobility clustering,  
585 peak intensity normalization, isoform/homology filtering and calculation of absolute in-sample  
586 amounts for each detected protein (48,49,98) according to the TOP3 quantification approach  
587 (53,54). Only peptides with a minimum length of seven amino acids that were identified with  
588 scores above or equal to 5.5 in at least two runs were considered. FDR for both peptides and  
589 proteins was set to 1% threshold and only proteins reported by at least two peptides (one of  
590 which unique) were quantified using the TOP3 method. The parts per million (ppm)  
591 abundance values (i.e. the relative amount (w/w) of each protein in respect to the sum over  
592 all detected proteins) were log<sub>2</sub>-transformed and normalized by subtraction of the median  
593 derived from all data points for the given protein. Significant changes in protein abundance  
594 were detected by moderated t-statistics essentially as described (96,97) across all technical  
595 replicates using an empirical Bayes approach and false discovery (FDR)-based correction for  
596 multiple comparisons (100). For this purpose, the Bioconductor R packages "limma" (101)  
597 and "q-value" (102) were used in RStudio, an integrated development environment for the  
598 open source programming language R. Proteins identified as contaminants (e.g. components  
599 of blood or hair cells) were removed from the analysis. Proteins with ppm values below 100  
600 which were not identified in one genotype were considered as just above detection level and  
601 also removed from the analysis. The relative abundance of a protein in myelin was accepted  
602 as altered if both statistically significant (q-value <0.05). Pie charts, heatmaps and volcano  
603 plots were prepared in Microsoft Excel 2013 and GraphPad Prism 7. Pearson's correlation  
604 coefficients derived from log<sub>2</sub>-transformed ppm abundance values were clustered and  
605 visualized with the tool heatmap.2 contained in the R package gplots ([CRAN.R-](http://CRAN.R-project.org/package=gplots)  
606 [project.org/package=gplots](http://CRAN.R-project.org/package=gplots)). Only pairwise complete observations were considered to  
607 reduce the influence of missing values on clustering behavior. The mass spectrometry  
608 proteomics data have been deposited to the ProteomeXchange Consortium

609 ([proteomecentral.proteomexchange.org](http://proteomecentral.proteomexchange.org)) via the PRIDE partner repository (103) with the  
610 dataset identifier PXD015960.

611

### 612 **Gel electrophoresis and silver staining of gels**

613 Protein concentration was determined using the DC Protein Assay kit (BioRad). Samples  
614 were separated on a 12% SDS-PAGE for 1 h at 200 V using the BioRad system, fixated  
615 overnight in 10% [v/v] acetic acid and 40 % [v/v] ethanol and then washed in 30% ethanol (2x  
616 20 min) and ddH<sub>2</sub>O (1x 20 min). For sensitization, gels were incubated 1 min in 0.012% [v/v]  
617 Na<sub>2</sub>S<sub>2</sub>O<sub>3</sub> and subsequently washed with ddH<sub>2</sub>O (3x 20 sec). For silver staining, gels were  
618 impregnated for 20 min in 0.2 % [w/v] AgNO<sub>3</sub> / 0.04% formaldehyde, washed with ddH<sub>2</sub>O (3x  
619 20 sec) and developed in 3% [w/v] Na<sub>2</sub>CO<sub>3</sub> / 0.02% [w/v] formaldehyde. The reaction was  
620 stopped by exchanging the solution with 5% [v/v] acetic acid.

621

### 622 **Immunoblotting**

623 Immunoblotting was performed as described (104,105). Primary antibodies were specific for  
624 dystrophin-related-protein 2 (DRP2; Sigma; 1:1000), peripheral myelin protein 2 (PMP2;  
625 ProteinTech Group 12717-1-AP; 1:1000), proteolipid protein (PLP/DM20; A431 (106);  
626 1:5000), Monocarboxylate transporter 1 (MCT1/SLC16A1; (107); 1:1000), periaxin (PRX;  
627 (59); 1:1000), sodium/potassium-transporting ATPase subunit alpha-1 (ATP1A1; 1:2000;  
628 Abcam #13736-1-AP), myelin protein zero (MPZ/P0; (108); kind gift by J. Archelos-Garcia;  
629 1:10.000), voltage-dependent anion-selective channel protein (VDAC; Abcam #ab15895;  
630 1:1000), basigin (BSG/CD147; ProteinTech Group #ab64616; 1:1000), neurofilament H  
631 (NEFH/NF-H; Covance #SMI-32P; 1:1000), voltage-gated potassium channel subunit A  
632 member 1 (KCNA1; Neuromab #73-007; 1:1000), EGR2/KROX20 ((109); kind gift by D.  
633 Meijer, Edinburgh; 1:1000) and myelin basic protein (MBP; 1:2000). To generate the latter  
634 antisera, rabbits were immunized (Pineda Antikörper Service, Berlin, Germany) with the  
635 KLH-coupled peptide CQDENPVVHFFK corresponding to amino acids 212-222 of mouse  
636 MBP isoform 1 (Swisprot/Uniprot-identifier P04370-1). Anti-MBP antisera were purified by  
637 affinity chromatography and extensively tested for specificity by immunoblot analysis of  
638 homogenate of brains dissected from wild-type mice compared to *Mbp*<sup>shiverer/shiverer</sup> mice that  
639 lack expression of MBP. Appropriate secondary anti-mouse or -rabbit antibodies conjugated  
640 to HRP were from dianova. Immunoblots were developed using the Enhanced  
641 Chemiluminescence Detection kit (Western Lightning® Plus, Perkin Elmer) and detected with  
642 the Intas ChemoCam system (INTAS Science Imaging Instruments GmbH, Göttingen,  
643 Germany).

644

### 645 **Immunolabelling of teased fibers**

646 Teased fibers were prepared as previously described (9,110). For each genotype, one male  
647 mouse was sacrificed by cervical dislocation at P17. Immunolabelling of teased fibers was  
648 performed as described (69). Briefly, teased fibers were fixed for 5 min in 4%  
649 paraformaldehyde, permeabilized 5 min with ice-cold methanol, washed in PBS (3x 5 min)  
650 and blocked for 1 h at 21°C in blocking buffer (10% horse serum, 0.25% Triton X-100, 1%  
651 bovine serum albumin in PBS). Primary antibodies were applied overnight at 4°C in  
652 incubation buffer (1.5% horse serum, 0.25% Triton X-100 in PBS). Samples were washed in  
653 PBS (3x 5 min) and secondary antibodies were applied in incubation buffer (1 h, RT).  
654 Samples were again washed in PBS (2x 5 min), and 4',6-diamidino-2-phenylindole (DAPI;  
655 1:50 000 in PBS) was applied for 10 min at RT. Samples were briefly washed 2x with ddH<sub>2</sub>O  
656 and mounted using Aqua-Poly/Mount (Polysciences, Eppelheim, Germany). Antibodies were  
657 specific for myelin-associated glycoprotein (MAG clone 513; Chemicon MAB1567; 1:50) and  
658 MCT1/SLC16A1 (107). Secondary antibodies were donkey  $\alpha$ -rabbit-Alexa488 (Invitrogen  
659 A21206; 1:1000) and donkey  $\alpha$ -mouse-Alexa555 (Invitrogen A21202; 1:1000). Labeled  
660 teased fibers were imaged using the confocal microscope Leica SP5. The signal was  
661 collected with the objective HCX PL APO lambda blue 63.0.x1.20. DAPI staining was excited  
662 with 405 nm and collected between 417 nm - 480 nm. To excite the Alexa488 fluorophore an  
663 Argon laser with the excitation of 488 nm was used and the emission was set to 500 nm -  
664 560 nm. Alexa555 was excited by using the DPSS561 laser at an excitation of 561 nm and  
665 the emission was set to 573 nm - 630 nm. To export and process the images LAS AF lite and  
666 Adobe Photoshop were used.

667

### 668 **mRNA abundance profiles**

669 Raw data were previously established (60) from the sciatic nerves of wild type Sprague  
670 Dawley rats at the indicated ages (E21, P6, P18; n=4 per time point). Briefly, sciatic nerves  
671 were dissected, the epineurium was removed, total RNA was extracted with the RNeasy Kit  
672 (Qiagen), concentration and quality (ratio of absorption at 260/280 nm) of RNA samples were  
673 determined using the NanoDrop spectrophotometer (ThermoScientific), integrity of the  
674 extracted RNA was determined with the Agilent 2100 Bioanalyser (Agilent Technologies) and  
675 RNA-Seq was performed using the Illumina HiSeq2000 platform. RNA-Seq raw data are  
676 available under the GEO accession number GSE115930 (60). For the present analysis, the  
677 fastqfiles were mapped to *rattus norvegicus* m6 using Tophat Aligner and then quantified  
678 based on the Ensemble Transcripts release v96. The raw read counts were then normalized  
679 using the R package DESeq2. The normalized gene expression data was then standardized  
680 to a mean of zero and a standard deviation of one, therefore genes with similar changes in  
681 expression are close in the euclidian space. Clustering was performed on the standardized



682 data using the R package mfuzz. Transcripts displaying abundance differences of less than  
683 10% coefficient of variation were considered developmentally unchanged.

684

### 685 **Venn diagrams**

686 Area-proportional Venn diagrams were prepared using BioVenn (111) at [www.biovenn.nl/](http://www.biovenn.nl/).

687

### 688 **GO-term**

689 For functional categorization of the myelin proteome the associated gene ontology terms  
690 were systematically analyzed on the mRNA abundance cluster using the Database for  
691 Annotation, Visualization and Integrated Discovery (DAVID; <https://david.ncifcrf.gov>). For  
692 comparison known myelin proteins according to literature were added.

693

### 694 **Histological analysis**

695 *Prx*<sup>-/-</sup> and control mice were perfused at the indicated ages intravascularly with fixative  
696 solution (2.5% glutaraldehyde, 4% paraformaldehyde, 0.1 M sodium cacodylate buffer, pH  
697 7.4). Quadriceps nerves were removed, fixed for 2 h at room temperature, followed by 18 h  
698 at 4°C in the same fixative, postfixed in OsO<sub>4</sub>, dehydrated a graded series of ethanol,  
699 followed by propylene oxide and embedded in Araldite. All axons not associated with a  
700 Remak bundle were counted and categorized as myelinated or non-myelinated. All myelin  
701 profiles lacking a recognizable axon were counted. The total number of axons were counted  
702 on micrographs of toluidine blue stained Araldite sections (0.5 μm) of quadriceps nerves.  
703 Precise p-values for the quantitative comparison between Ctrl and *Prx*<sup>-/-</sup> mice were: Total  
704 number of axons (**Figure 6B**; Student's unpaired t-test): 2 mo p=0.01734; 4 mo p=2.1E-05; 9  
705 mo p=0.007625; Number of myelinated axons (**Figure 6C**; Student's unpaired t-test): 2 mo  
706 p=0.00444; 4 mo p=2.12E-05; 9 mo p=0.005766; Number of empty myelin profiles (**Figure**  
707 **6D**; Student's unpaired t-test): 2 mo p=0.004445; 4 mo p=0.001461; 9 mo p=0.000695;  
708 Axonal diameters (**Figure 6E-G**; two-sided Kolmogorow-Smirnow test): 2 mo p=2.20E-16; 4  
709 mo p=2.20E-16; 9 mo p=2.20E-16.

710

711

712 **ACKNOWLEDGMENTS**

713 We thank J. Archelos-Garcia and D. Meijer for antibodies, T. Buscham and J. Edgar for  
714 discussions, L. Piepkorn for support in data analysis, K.-A. Nave for support made possible  
715 by a European Research Council Advanced Grant ('MyeliNano' to K.-A.N.) and the  
716 International Max Planck Research School for Genome Science (IMPRS-GS) for supporting  
717 S.B.S..

718

719

720 **FUNDING**

721 Our work is supported by the Deutsche Forschungsgemeinschaft (DFG; Grants WE 2720/2-  
722 2, WE 2720/4-1 and WE 2720/5-1 to H.B.W. and RO 4076/3-2 to M.J.R.) and the Wellcome  
723 Trust (Grant No 0842424 to P.J.B.).

724

725

726 **CONFLICT OF INTEREST STATEMENT**

727 The authors declare no conflict of interest.

728

729

730

731 **REFERENCES**

732

- 733 1. Weil M-T, Heibeck S, Töpperwien M, tom Dieck S, Ruhwedel T, Salditt T, et al. Axonal  
734 Ensheathment in the Nervous System of Lamprey: Implications for the Evolution of Myelinating  
735 Glia. *J Neurosci* [Internet]. 2018 Jul 18;38(29):6586–96. Available from:  
736 <http://www.jneurosci.org/lookup/doi/10.1523/JNEUROSCI.1034-18.2018>
- 737 2. Hartline DK, Colman DR. Rapid Conduction and the Evolution of Giant Axons and Myelinated  
738 Fibers. *Curr Biol* [Internet]. 2007 Jan;17(1):R29–35. Available from:  
739 <https://linkinghub.elsevier.com/retrieve/pii/S0960982206025231>
- 740 3. Rossor AM, Polke JM, Houlden H, Reilly MM. Clinical implications of genetic advances in  
741 Charcot–Marie–Tooth disease. *Nat Rev Neurol* [Internet]. 2013 Oct 10;9(10):562–71. Available  
742 from: <http://www.nature.com/articles/nrneuro.2013.179>
- 743 4. Michailov G V. Axonal Neuregulin-1 Regulates Myelin Sheath Thickness. *Science* (80- )  
744 [Internet]. 2004 Apr 30;304(5671):700–3. Available from:  
745 <http://www.sciencemag.org/cgi/doi/10.1126/science.1095862>
- 746 5. Taveggia C, Zanazzi G, Petrylak A, Yano H, Rosenbluth J, Einheber S, et al. Neuregulin-1  
747 Type III Determines the Ensheathment Fate of Axons. *Neuron* [Internet]. 2005 Sep;47(5):681–  
748 94. Available from: <https://linkinghub.elsevier.com/retrieve/pii/S0896627305006926>
- 749 6. Chernousov MA, Yu W-M, Chen Z-L, Carey DJ, Strickland S. Regulation of Schwann cell  
750 function by the extracellular matrix. *Glia* [Internet]. 2008 Nov 1;56(14):1498–507. Available  
751 from: <http://doi.wiley.com/10.1002/glia.20740>
- 752 7. Petersen SC, Luo R, Liebscher I, Giera S, Jeong S-J, Mogha A, et al. The Adhesion GPCR  
753 GPR126 Has Distinct, Domain-Dependent Functions in Schwann Cell Development Mediated  
754 by Interaction with Laminin-211. *Neuron* [Internet]. 2015 Feb;85(4):755–69. Available from:  
755 <https://linkinghub.elsevier.com/retrieve/pii/S0896627314011660>
- 756 8. Ghidinelli M, Poitelon Y, Shin YK, Ameroso D, Williamson C, Ferri C, et al. Laminin 211 inhibits  
757 protein kinase A in Schwann cells to modulate neuregulin 1 type III-driven myelination. Emery  
758 B, editor. *PLOS Biol* [Internet]. 2017 Jun 21;15(6):e2001408. Available from:  
759 <https://dx.plos.org/10.1371/journal.pbio.2001408>
- 760 9. Sherman DL, Fabrizi C, Gillespie CS, Brophy PJ. Specific Disruption of a Schwann Cell  
761 Dystrophin-Related Protein Complex in a Demyelinating Neuropathy. *Neuron* [Internet]. 2001  
762 May;30(3):677–87. Available from:  
763 <https://linkinghub.elsevier.com/retrieve/pii/S0896627301003270>
- 764 10. Masaki T, Matsumura K, Hirata A, Yamada H, Hase A, Arai K, et al. Expression of  
765 Dystroglycan and the Laminin- $\alpha$ 2 Chain in the Rat Peripheral Nerve during Development. *Exp*  
766 *Neurol* [Internet]. 2002 Mar;174(1):109–17. Available from:  
767 <https://linkinghub.elsevier.com/retrieve/pii/S0014488601978562>
- 768 11. Nodari A, Previtali SC, Dati G, Occhi S, Court FA, Colombelli C, et al.  $\alpha$ 4 Integrin and  
769 Dystroglycan Cooperate to Stabilize the Myelin Sheath. *J Neurosci* [Internet]. 2008 Jun  
770 25;28(26):6714–9. Available from: [http://www.jneurosci.org/cgi/doi/10.1523/JNEUROSCI.0326-](http://www.jneurosci.org/cgi/doi/10.1523/JNEUROSCI.0326-08.2008)  
771 08.2008

- 772 12. Raasakka A, Linxweiler H, Brophy PJ, Sherman DL, Kursula P. Direct Binding of the Flexible  
773 C-Terminal Segment of Periaxin to  $\beta$ 4 Integrin Suggests a Molecular Basis for CMT4F. *Front*  
774 *Mol Neurosci* [Internet]. 2019 Apr 9;12. Available from:  
775 <https://www.frontiersin.org/article/10.3389/fnmol.2019.00084/full>
- 776 13. Hess A, Lansing AI. The fine structure of peripheral nerve fibers. *Anat Rec.* 1953;
- 777 14. Sherman DL, Brophy PJ. Mechanisms of axon ensheathment and myelin growth. *Nat Rev*  
778 *Neurosci* [Internet]. 2005 Sep;6(9):683–90. Available from:  
779 <http://www.nature.com/articles/nrn1743>
- 780 15. Pereira JA, Lebrun-Julien F, Suter U. Molecular mechanisms regulating myelination in the  
781 peripheral nervous system. *Trends Neurosci* [Internet]. 2012 Feb;35(2):123–34. Available from:  
782 <https://linkinghub.elsevier.com/retrieve/pii/S0166223611001937>
- 783 16. Grove M, Brophy PJ. FAK Is Required for Schwann Cell Spreading on Immature Basal Lamina  
784 to Coordinate the Radial Sorting of Peripheral Axons with Myelination. *J Neurosci* [Internet].  
785 2014 Oct 1;34(40):13422–34. Available from:  
786 <http://www.jneurosci.org/cgi/doi/10.1523/JNEUROSCI.1764-14.2014>
- 787 17. Monk KR, Feltri ML, Taveggia C. New insights on schwann cell development. *Glia* [Internet].  
788 2015 Aug;63(8):1376–93. Available from: <http://doi.wiley.com/10.1002/glia.22852>
- 789 18. Feltri ML, Poitelon Y, Previtali SC. How Schwann Cells Sort Axons. *Neurosci* [Internet]. 2016  
790 Jun 16;22(3):252–65. Available from:  
791 <http://journals.sagepub.com/doi/10.1177/1073858415572361>
- 792 19. Giese KP, Martini R, Lemke G, Soriano P, Schachner M. Mouse P0 gene disruption leads to  
793 hypomyelination, abnormal expression of recognition molecules, and degeneration of myelin  
794 and axons. *Cell* [Internet]. 1992 Nov;71(4):565–76. Available from:  
795 <https://linkinghub.elsevier.com/retrieve/pii/009286749290591Y>
- 796 20. Martini R, Mohajeri MH, Kasper S, Giese KP, Schachner M. Mice doubly deficient in the genes  
797 for P0 and myelin basic protein show that both proteins contribute to the formation of the major  
798 dense line in peripheral nerve myelin. *J Neurosci.* 1995;
- 799 21. Nawaz S, Schweitzer J, Jahn O, Werner HB. Molecular evolution of myelin basic protein, an  
800 abundant structural myelin component. *Glia* [Internet]. 2013 Aug;61(8):1364–77. Available  
801 from: <http://doi.wiley.com/10.1002/glia.22520>
- 802 22. Greenfield S, Brostoff S, Eylar EH, Morell P. PROTEIN COMPOSITION OF MYELIN OF THE  
803 PERIPHERAL NERVOUS SYSTEM. *J Neurochem* [Internet]. 1973 Apr;20(4):1207–16.  
804 Available from: <http://doi.wiley.com/10.1111/j.1471-4159.1973.tb00089.x>
- 805 23. Brostoff SW, Karkhanis YD, Carlo DJ, Reuter W, Eylar EH. Isolation and partial  
806 characterization of the major proteins of rabbit sciatic nerve myelin. *Brain Res* [Internet]. 1975  
807 Mar;86(3):449–58. Available from:  
808 <https://linkinghub.elsevier.com/retrieve/pii/0006899375908951>
- 809 24. Nave K-A, Werner HB. Myelination of the Nervous System: Mechanisms and Functions. *Annu*  
810 *Rev Cell Dev Biol* [Internet]. 2014 Oct 11;30(1):503–33. Available from:  
811 <http://www.annualreviews.org/doi/10.1146/annurev-cellbio-100913-013101>
- 812 25. Kleopa KA, Sargiannidou I. Connexins, gap junctions and peripheral neuropathy. *Neurosci Lett*

- 813 [Internet]. 2015 Jun;596:27–32. Available from:  
814 <https://linkinghub.elsevier.com/retrieve/pii/S0304394014008453>
- 815 26. Court FA, Sherman DL, Pratt T, Garry EM, Ribchester RR, Cottrell DF, et al. Restricted growth  
816 of Schwann cells lacking Cajal bands slows conduction in myelinated nerves. *Nature* [Internet].  
817 2004 Sep;431(7005):191–5. Available from: <http://www.nature.com/articles/nature02841>
- 818 27. Beirowski B, Babetto E, Golden JP, Chen Y-J, Yang K, Gross RW, et al. Metabolic regulator  
819 LKB1 is crucial for Schwann cell-mediated axon maintenance. *Nat Neurosci* [Internet]. 2014  
820 Oct 7;17(10):1351–61. Available from: <http://www.nature.com/articles/nn.3809>
- 821 28. Domenech-Estevez E, Baloui H, Repond C, Rosafio K, Medard J-J, Tricaud N, et al.  
822 Distribution of Monocarboxylate Transporters in the Peripheral Nervous System Suggests  
823 Putative Roles in Lactate Shuttling and Myelination. *J Neurosci* [Internet]. 2015 Mar  
824 11;35(10):4151–6. Available from: [http://www.jneurosci.org/cgi/doi/10.1523/JNEUROSCI.3534-](http://www.jneurosci.org/cgi/doi/10.1523/JNEUROSCI.3534-14.2015)  
825 [14.2015](http://www.jneurosci.org/cgi/doi/10.1523/JNEUROSCI.3534-14.2015)
- 826 29. Kim S, Maynard JC, Sasaki Y, Strickland A, Sherman DL, Brophy PJ, et al. Schwann Cell O-  
827 GlcNAc Glycosylation Is Required for Myelin Maintenance and Axon Integrity. *J Neurosci*  
828 [Internet]. 2016 Sep 14;36(37):9633–46. Available from:  
829 <http://www.jneurosci.org/cgi/doi/10.1523/JNEUROSCI.1235-16.2016>
- 830 30. Gonçalves NP, Vægter CB, Andersen H, Østergaard L, Calcutt NA, Jensen TS. Schwann cell  
831 interactions with axons and microvessels in diabetic neuropathy. *Nat Rev Neurol* [Internet].  
832 2017 Mar 30;13(3):135–47. Available from: <http://www.nature.com/articles/nrneuro.2016.201>
- 833 31. Stassart RM, Möbius W, Nave K-A, Edgar JM. The Axon-Myelin Unit in Development and  
834 Degenerative Disease. *Front Neurosci* [Internet]. 2018 Jul 11;12. Available from:  
835 <https://www.frontiersin.org/article/10.3389/fnins.2018.00467/full>
- 836 32. Nagarajan R, Le N, Mahoney H, Araki T, Milbrandt J. Deciphering peripheral nerve myelination  
837 by using Schwann cell expression profiling. *Proc Natl Acad Sci* [Internet]. 2002 Jun  
838 25;99(13):8998–9003. Available from: <http://www.pnas.org/cgi/doi/10.1073/pnas.132080999>
- 839 33. Le N, Nagarajan R, Wang JYT, Araki T, Schmidt RE, Milbrandt J. Analysis of congenital  
840 hypomyelinating Egr2Lo/Lo nerves identifies Sox2 as an inhibitor of Schwann cell  
841 differentiation and myelination. *Proc Natl Acad Sci* [Internet]. 2005 Feb 15;102(7):2596–601.  
842 Available from: <http://www.pnas.org/cgi/doi/10.1073/pnas.0407836102>
- 843 34. Ryu EJ, Yang M, Gustin JA, Chang L-W, Freimuth RR, Nagarajan R, et al. Analysis of  
844 Peripheral Nerve Expression Profiles Identifies a Novel Myelin Glycoprotein, MP11. *J Neurosci*  
845 [Internet]. 2008 Jul 23;28(30):7563–73. Available from:  
846 <http://www.jneurosci.org/cgi/doi/10.1523/JNEUROSCI.1659-08.2008>
- 847 35. Zhang Y, Chen K, Sloan SA, Bennett ML, Scholze AR, O’Keeffe S, et al. An RNA-Sequencing  
848 Transcriptome and Splicing Database of Glia, Neurons, and Vascular Cells of the Cerebral  
849 Cortex. *J Neurosci* [Internet]. 2014 Sep 3;34(36):11929–47. Available from:  
850 <http://www.jneurosci.org/cgi/doi/10.1523/JNEUROSCI.1860-14.2014>
- 851 36. Patzig J, Erwig MS, Tenzer S, Kusch K, Dibaj P, Möbius W, et al. Septin/anillin filaments  
852 scaffold central nervous system myelin to accelerate nerve conduction. *Elife*. 2016;5:e17119.
- 853 37. Sharma K, Schmitt S, Bergner CG, Tyanova S, Kannaiyan N, Manrique-Hoyos N, et al. Cell

- 854 type- and brain region-resolved mouse brain proteome. *Nat Neurosci* [Internet]. 2015 Dec  
855 2;18(12):1819–31. Available from: <http://www.nature.com/articles/nn.4160>
- 856 38. Thakurela S, Garding A, Jung RB, Müller C, Goebbels S, White R, et al. The transcriptome of  
857 mouse central nervous system myelin. *Sci Rep* [Internet]. 2016 May 13;6(1):25828. Available  
858 from: <http://www.nature.com/articles/srep25828>
- 859 39. Marques S, Zeisel A, Codeluppi S, van Bruggen D, Mendanha Falcao A, Xiao L, et al.  
860 Oligodendrocyte heterogeneity in the mouse juvenile and adult central nervous system.  
861 *Science* (80- ) [Internet]. 2016 Jun 10;352(6291):1326–9. Available from:  
862 <http://www.sciencemag.org/cgi/doi/10.1126/science.aaf6463>
- 863 40. De Monasterio-Schrader P, Jahn O, Tenzer S, Wichert SP, Patzig J, Werner HB. Systematic  
864 approaches to central nervous system myelin. *Cellular and Molecular Life Sciences*. 2012.
- 865 41. Patzig J, Jahn O, Tenzer S, Wichert SP, de Monasterio-Schrader P, Rosfa S, et al.  
866 Quantitative and Integrative Proteome Analysis of Peripheral Nerve Myelin Identifies Novel  
867 Myelin Proteins and Candidate Neuropathy Loci. *J Neurosci* [Internet]. 2011 Nov  
868 9;31(45):16369–86. Available from:  
869 <http://www.jneurosci.org/cgi/doi/10.1523/JNEUROSCI.4016-11.2011>
- 870 42. Kangas SM, Ohlmeier S, Sormunen R, Jouhilahti E-M, Peltonen S, Peltonen J, et al. An  
871 approach to comprehensive genome and proteome expression analyses in Schwann cells and  
872 neurons during peripheral nerve myelin formation. *J Neurochem* [Internet]. 2016  
873 Sep;138(6):830–44. Available from: <http://doi.wiley.com/10.1111/jnc.13722>
- 874 43. Kusch K, Uecker M, Liepold T, Möbius W, Hoffmann C, Neumann H, et al. Partial  
875 Immunoblotting of 2D-Gels: A Novel Method to Identify Post-Translationally Modified Proteins  
876 Exemplified for the Myelin Acetylome. *Proteomes* [Internet]. 2017 Jan 12;5(4):3. Available  
877 from: <http://www.mdpi.com/2227-7382/5/1/3>
- 878 44. Neilson KA, Ali NA, Muralidharan S, Mirzaei M, Mariani M, Assadourian G, et al. Less label,  
879 more free: Approaches in label-free quantitative mass spectrometry. *Proteomics*. 2011.
- 880 45. Distler U, Kuharev J, Tenzer S. Biomedical applications of ion mobility-enhanced data-  
881 independent acquisition-based label-free quantitative proteomics. *Expert Rev Proteomics*.  
882 2014;
- 883 46. Geromanos SJ, Vissers JPC, Silva JC, Dorschel CA, Li GZ, Gorenstein M V., et al. The  
884 detection, correlation, and comparison of peptide precursor and product ions from data  
885 independent LC-MS with data dependant LC-MS/MS. *Proteomics*. 2009;
- 886 47. Li GZ, Vissers JPC, Silva JC, Golick D, Gorenstein M V., Geromanos SJ. Database searching  
887 and accounting of multiplexed precursor and product ion spectra from the data independent  
888 analysis of simple and complex peptide mixtures. *Proteomics*. 2009;
- 889 48. Distler U, Kuharev J, Navarro P, Tenzer S. Label-free quantification in ion mobility-enhanced  
890 data-independent acquisition proteomics. *Nat Protoc* [Internet]. 2016 Apr 24;11(4):795–812.  
891 Available from: <http://www.nature.com/articles/nprot.2016.042>
- 892 49. Distler U, Kuharev J, Navarro P, Levin Y, Schild H, Tenzer S. Drift time-specific collision  
893 energies enable deep-coverage data-independent acquisition proteomics. *Nat Methods*  
894 [Internet]. 2014 Feb 15;11(2):167–70. Available from:

- 895 <http://www.nature.com/articles/nmeth.2767>
- 896 50. Larocca JN, Norton WT. Isolation of Myelin. *Curr Protoc Cell Biol* [Internet]. 2006  
897 Dec;33(1):3.25.1-3.25.19. Available from: <http://doi.wiley.com/10.1002/0471143030.cb0325s33>
- 898 51. Jahn O, Tenzer S, Werner HB. Myelin proteomics: Molecular anatomy of an insulating sheath.  
899 *Molecular Neurobiology*. 2009.
- 900 52. Erwig MS, Hesse D, Jung RB, Uecker M, Kusch K, Tenzer S, et al. Myelin: Methods for  
901 Purification and Proteome Analysis. In: *Methods in Molecular Biology* [Internet]. 2019. p. 37–  
902 63. Available from: [http://link.springer.com/10.1007/978-1-4939-9072-6\\_3](http://link.springer.com/10.1007/978-1-4939-9072-6_3)
- 903 53. Silva JC, Gorenstein M V., Li G-Z, Vissers JPC, Geromanos SJ. Absolute Quantification of  
904 Proteins by LCMS E. *Mol Cell Proteomics* [Internet]. 2006 Jan;5(1):144–56. Available from:  
905 <http://www.mcponline.org/lookup/doi/10.1074/mcp.M500230-MCP200>
- 906 54. Ahrné E, Molzahn L, Glatter T, Schmidt A. Critical assessment of proteome-wide label-free  
907 absolute abundance estimation strategies. *Proteomics*. 2013;
- 908 55. Dodds JN, Baker ES. Ion Mobility Spectrometry: Fundamental Concepts, Instrumentation,  
909 Applications, and the Road Ahead. *J Am Soc Mass Spectrom*. 2019;
- 910 56. Micko S, Schlaepfer WW. PROTEIN COMPOSITION OF AXONS and MYELIN FROM RAT  
911 and HUMAN PERIPHERAL NERVES. *J Neurochem* [Internet]. 1978 May;30(5):1041–9.  
912 Available from: <http://doi.wiley.com/10.1111/j.1471-4159.1978.tb12397.x>
- 913 57. Smith ME, Curtis BM. FROG SCIATIC NERVE MYELIN: A CHEMICAL CHARACTERIZATION.  
914 *J Neurochem* [Internet]. 1979 Aug;33(2):447–52. Available from:  
915 <http://doi.wiley.com/10.1111/j.1471-4159.1979.tb05174.x>
- 916 58. Whitaker JN. The protein antigens of peripheral nerve myelin. *Ann Neurol* [Internet].  
917 1981;9(S1):56–64. Available from: <http://doi.wiley.com/10.1002/ana.410090710>
- 918 59. Gillespie CS, Sherman DL, Blair GE, Brophy PJ. Periaxin, a novel protein of myelinating  
919 schwann cells with a possible role in axonal ensheathment. *Neuron* [Internet]. 1994  
920 Mar;12(3):497–508. Available from:  
921 <https://linkinghub.elsevier.com/retrieve/pii/0896627394902089>
- 922 60. Fledrich R, Abdelaal T, Rasch L, Bansal V, Schütza V, Brügger B, et al. Targeting myelin lipid  
923 metabolism as a potential therapeutic strategy in a model of CMT1A neuropathy. *Nat Commun*  
924 [Internet]. 2018 Dec 2;9(1):3025. Available from: [http://www.nature.com/articles/s41467-018-](http://www.nature.com/articles/s41467-018-05420-0)  
925 [05420-0](http://www.nature.com/articles/s41467-018-05420-0)
- 926 61. Pareyson D, Marchesi C. Diagnosis, natural history, and management of Charcot–Marie–Tooth  
927 disease. *Lancet Neurol* [Internet]. 2009 Jul;8(7):654–67. Available from:  
928 <https://linkinghub.elsevier.com/retrieve/pii/S1474442209701103>
- 929 62. Baets J, De Jonghe P, Timmerman V. Recent advances in Charcot–Marie–Tooth disease. *Curr*  
930 *Opin Neurol* [Internet]. 2014 Oct;27(5):532–40. Available from:  
931 [http://content.wkhealth.com/linkback/openurl?sid=WKPTLP:landingpage&an=00019052-](http://content.wkhealth.com/linkback/openurl?sid=WKPTLP:landingpage&an=00019052-201410000-00006)  
932 [201410000-00006](http://content.wkhealth.com/linkback/openurl?sid=WKPTLP:landingpage&an=00019052-201410000-00006)
- 933 63. Brennan KM, Bai Y, Shy ME. Demyelinating CMT—what’s known, what’s new and what’s in  
934 store? *Neurosci Lett* [Internet]. 2015 Jun;596:14–26. Available from:  
935 <https://linkinghub.elsevier.com/retrieve/pii/S0304394015000725>

- 936 64. Gillespie CS, Sherman DL, Fleetwood-Walker SM, Cottrell DF, Tait S, Garry EM, et al.  
937 Peripheral Demyelination and Neuropathic Pain Behavior in Periaxin-Deficient Mice. *Neuron*  
938 [Internet]. 2000 May;26(2):523–31. Available from:  
939 <https://linkinghub.elsevier.com/retrieve/pii/S0896627300811848>
- 940 65. Guilbot A. A mutation in periaxin is responsible for CMT4F, an autosomal recessive form of  
941 Charcot-Marie-Tooth disease. *Hum Mol Genet* [Internet]. 2001 Feb 1;10(4):415–21. Available  
942 from: <https://academic.oup.com/hmg/article-lookup/doi/10.1093/hmg/10.4.415>
- 943 66. Berger P, Niemann A, Suter U. Schwann cells and the pathogenesis of inherited motor and  
944 sensory neuropathies (Charcot-Marie-Tooth disease). *Glia* [Internet]. 2006 Sep;54(4):243–57.  
945 Available from: <http://doi.wiley.com/10.1002/glia.20386>
- 946 67. Marchesi C, Milani M, Morbin M, Cesani M, Lauria G, Scaioli V, et al. Four novel cases of  
947 periaxin-related neuropathy and review of the literature. *Neurology* [Internet]. 2010 Nov  
948 16;75(20):1830–8. Available from:  
949 <http://www.neurology.org/cgi/doi/10.1212/WNL.0b013e3181fd6314>
- 950 68. Philp NJ, Ochrietor JD, Rudoy C, Muramatsu T, Linser PJ. Loss of MCT1, MCT3, and MCT4  
951 Expression in the Retinal Pigment Epithelium and Neural Retina of the 5A11/Basigin-Null  
952 Mouse. *Investig Ophthalmology Vis Sci* [Internet]. 2003 Mar 1;44(3):1305. Available from:  
953 <http://iovs.arvojournals.org/article.aspx?doi=10.1167/iovs.02-0552>
- 954 69. Patzig J, Kusch K, Fledrich R, Eichel MA, Lüders KA, Möbius W, et al. Proteolipid protein  
955 modulates preservation of peripheral axons and premature death when myelin protein zero is  
956 lacking. *Glia* [Internet]. 2016 Jan;64(1):155–74. Available from:  
957 <http://doi.wiley.com/10.1002/glia.22922>
- 958 70. Lee Y, Morrison BM, Li Y, Lengacher S, Farah MH, Hoffman PN, et al. Oligodendroglia  
959 metabolically support axons and contribute to neurodegeneration. *Nature* [Internet]. 2012 Jul  
960 11;487(7408):443–8. Available from: <http://www.nature.com/articles/nature11314>
- 961 71. Fünfschilling U, Supplie LM, Mahad D, Boretius S, Saab AS, Edgar J, et al. Glycolytic  
962 oligodendrocytes maintain myelin and long-term axonal integrity. *Nature* [Internet]. 2012 May  
963 29;485(7399):517–21. Available from: <http://www.nature.com/articles/nature11007>
- 964 72. Morrison BM, Tsingalia A, Vidensky S, Lee Y, Jin L, Farah MH, et al. Deficiency in  
965 monocarboxylate transporter 1 (MCT1) in mice delays regeneration of peripheral nerves  
966 following sciatic nerve crush. *Exp Neurol* [Internet]. 2015 Jan;263:325–38. Available from:  
967 <https://linkinghub.elsevier.com/retrieve/pii/S0014488614003549>
- 968 73. Morrison BM, Lee Y, Rothstein JD. Oligodendroglia: Metabolic supporters of axons. *Trends in*  
969 *Cell Biology*. 2013.
- 970 74. Saab AS, Tzvetanova ID, Nave K-A. The role of myelin and oligodendrocytes in axonal energy  
971 metabolism. *Curr Opin Neurobiol* [Internet]. 2013 Dec;23(6):1065–72. Available from:  
972 <https://linkinghub.elsevier.com/retrieve/pii/S0959438813001888>
- 973 75. Rinholm JE, Bergersen LH. White matter lactate – Does it matter? *Neuroscience* [Internet].  
974 2014 Sep;276:109–16. Available from:  
975 <https://linkinghub.elsevier.com/retrieve/pii/S0306452213008464>
- 976 76. Jha MK, Lee Y, Russell KA, Yang F, Dastgheyb RM, Deme P, et al. Monocarboxylate



- 977 transporter 1 in Schwann cells contributes to maintenance of sensory nerve myelination during  
978 aging. *Glia*. 2019;
- 979 77. Edgar JM, McLaughlin M, Werner HB, McCulloch MC, Barrie JA, Brown A, et al. Early  
980 ultrastructural defects of axons and axon-glia junctions in mice lacking expression of *Cnp1*.  
981 *Glia*. 2009;
- 982 78. Verheijen MHG. Local regulation of fat metabolism in peripheral nerves. *Genes Dev* [Internet].  
983 2003 Oct 1;17(19):2450–64. Available from:  
984 <http://www.genesdev.org/cgi/doi/10.1101/gad.1116203>
- 985 79. Buchstaller J. Efficient Isolation and Gene Expression Profiling of Small Numbers of Neural  
986 Crest Stem Cells and Developing Schwann Cells. *J Neurosci* [Internet]. 2004 Mar  
987 10;24(10):2357–65. Available from:  
988 <http://www.jneurosci.org/cgi/doi/10.1523/JNEUROSCI.4083-03.2004>
- 989 80. D'antonio M, Michalovich D, Paterson M, Droggiti A, Woodhoo A, Mirsky R, et al. Gene  
990 profiling and bioinformatic analysis of Schwann cell embryonic development and myelination.  
991 *Glia* [Internet]. 2006 Apr 1;53(5):501–15. Available from:  
992 <http://doi.wiley.com/10.1002/glia.20309>
- 993 81. Schaeren-Wiemers N, Bonnet A, Erb M, Erne B, Bartsch U, Kern F, et al. The raft-associated  
994 protein MAL is required for maintenance of proper axon–glia interactions in the central nervous  
995 system. *J Cell Biol* [Internet]. 2004 Aug 30;166(5):731–42. Available from:  
996 <http://www.jcb.org/lookup/doi/10.1083/jcb.200406092>
- 997 82. Adlkofer K, Martini R, Aguzzi A, Zielasek J, Toyka K V., Suter U. Hypermyelination and  
998 demyelinating peripheral neuropathy in *Pmp22*-deficient mice. *Nat Genet* [Internet]. 1995  
999 Nov;11(3):274–80. Available from: <http://www.nature.com/articles/ng1195-274>
- 1000 83. Riethmacher D, Sonnenberg-Riethmacher E, Brinkmann V, Yamaai T, Lewin GR, Birchmeier  
1001 C. Severe neuropathies in mice with targeted mutations in the ErbB3 receptor. *Nature*  
1002 [Internet]. 1997 Oct;389(6652):725–30. Available from: <http://www.nature.com/articles/39593>
- 1003 84. Woldeyesus MT, Britsch S, Riethmacher D, Xu L, Sonnenberg-Riethmacher E, Abou-Rebyeh  
1004 F, et al. Peripheral nervous system defects in *erbB2* mutants following genetic rescue of heart  
1005 development. *Genes Dev* [Internet]. 1999 Oct 1;13(19):2538–48. Available from:  
1006 <http://www.genesdev.org/cgi/doi/10.1101/gad.13.19.2538>
- 1007 85. Ackerman SD, Luo R, Poitelon Y, Mogha A, Harty BL, D'Rozario M, et al. GPR56/ADGRG1  
1008 regulates development and maintenance of peripheral myelin. *J Exp Med* [Internet]. 2018 Mar  
1009 5;215(3):941–61. Available from: <http://www.jem.org/lookup/doi/10.1084/jem.20161714>
- 1010 86. Monk KR, Oshima K, Jors S, Heller S, Talbot WS. Gpr126 is essential for peripheral nerve  
1011 development and myelination in mammals. *Development* [Internet]. 2011 Jul 1;138(13):2673–  
1012 80. Available from: <http://dev.biologists.org/cgi/doi/10.1242/dev.062224>
- 1013 87. Monk KR, Naylor SG, Glenn TD, Mercurio S, Perlin JR, Dominguez C, et al. A G Protein-  
1014 Coupled Receptor Is Essential for Schwann Cells to Initiate Myelination. *Science* (80- )  
1015 [Internet]. 2009 Sep 11;325(5946):1402–5. Available from:  
1016 <http://www.sciencemag.org/cgi/doi/10.1126/science.1173474>
- 1017 88. Kabzinska D, Drac H, Sherman DL, Kostera-Pruszczyk A, Brophy PJ, Kochanski A, et al.

- 1018 Charcot-Marie-Tooth type 4F disease caused by S399fsx410 mutation in the PRX gene.  
1019 Neurology [Internet]. 2006 Mar 14;66(5):745–7. Available from:  
1020 <http://www.neurology.org/cgi/doi/10.1212/01.wnl.0000201269.46071.35>
- 1021 89. Baránková L, Šišková D, Hühne K, Vyhňálková E, Sakmaryová I, Bojar M, et al. A 71-  
1022 nucleotide deletion in the periaxin gene in a Romani patient with early-onset slowly progressive  
1023 demyelinating CMT. Eur J Neurol [Internet]. 2008 Jun;15(6):548–51. Available from:  
1024 <http://doi.wiley.com/10.1111/j.1468-1331.2008.02104.x>
- 1025 90. Tokunaga S, Hashiguchi A, Yoshimura A, Maeda K, Suzuki T, Haruki H, et al. Late-onset  
1026 Charcot-Marie-Tooth disease 4F caused by periaxin gene mutation. Neurogenetics [Internet].  
1027 2012 Nov 1;13(4):359–65. Available from: <http://link.springer.com/10.1007/s10048-012-0338-5>
- 1028 91. Gallardo E, García A, Ramón C, Maraví E, Infante J, Gastón I, et al. Charcot-Marie-Tooth  
1029 disease type 2J with MPZ Thr124Met mutation: clinico-electrophysiological and MRI study of a  
1030 family. J Neurol [Internet]. 2009 Dec 22;256(12):2061–71. Available from:  
1031 <http://link.springer.com/10.1007/s00415-009-5251-y>
- 1032 92. Leal A, Berghoff C, Berghoff M, Rojas-Araya M, Ortiz C, Heuss D, et al. A Costa Rican family  
1033 affected with Charcot-Marie-Tooth disease due to the myelin protein zero (MPZ) p.Thr124Met  
1034 mutation shares the Belgian haplotype. Rev Biol Trop [Internet]. 2014 Dec 1;62(4):1285.  
1035 Available from: <http://revistas.ucr.ac.cr/index.php/rbt/article/view/13473>
- 1036 93. Tokuda N, Noto Y, Kitani-Morii F, Hamano A, Kasai T, Shiga K, et al. Parasympathetic  
1037 Dominant Autonomic Dysfunction in Charcot-Marie-Tooth Disease Type 2J with the *MPZ*  
1038 Thr124Met Mutation. Intern Med [Internet]. 2015;54(15):1919–22. Available from:  
1039 [https://www.jstage.jst.go.jp/article/internalmedicine/54/15/54\\_54.4259/\\_article](https://www.jstage.jst.go.jp/article/internalmedicine/54/15/54_54.4259/_article)
- 1040 94. Duan X, Gu W, Hao Y, Wang R, Wen H, Sun S, et al. A Novel Asp121Asn Mutation of Myelin  
1041 Protein Zero Is Associated with Late-Onset Axonal Charcot-Marie-Tooth Disease, Hearing  
1042 Loss and Pupil Abnormalities. Front Aging Neurosci [Internet]. 2016 Sep 22;8. Available from:  
1043 <http://journal.frontiersin.org/Article/10.3389/fnagi.2016.00222/abstract>
- 1044 95. Fabrizi GM, Tamburin S, Cavallaro T, Cabrini I, Ferrarini M, Taioli F, et al. The spectrum of  
1045 Charcot-Marie-Tooth disease due to myelin protein zero: An electrodiagnostic, nerve  
1046 ultrasound and histological study. Clin Neurophysiol [Internet]. 2018 Jan;129(1):21–32.  
1047 Available from: <https://linkinghub.elsevier.com/retrieve/pii/S1388245717310854>
- 1048 96. Ambrozkiwicz MC, Schwark M, Kishimoto-Suga M, Borisova E, Hori K, Salazar-Lázaro A, et  
1049 al. Polarity Acquisition in Cortical Neurons Is Driven by Synergistic Action of Sox9-Regulated  
1050 Wwp1 and Wwp2 E3 Ubiquitin Ligases and Intronic miR-140. Neuron [Internet]. 2018  
1051 Dec;100(5):1097-1115.e15. Available from:  
1052 <https://linkinghub.elsevier.com/retrieve/pii/S0896627318308961>
- 1053 97. Erwig MS, Patzig J, Steyer AM, Dibaj P, Heilmann M, Heilmann I, et al. Anillin facilitates septin  
1054 assembly to prevent pathological unfoldings of central nervous system myelin. Elife [Internet].  
1055 2019 Jan 23;8. Available from: <https://elifesciences.org/articles/43888>
- 1056 98. Kuharev J, Navarro P, Distler U, Jahn O, Tenzer S. In-depth evaluation of software tools for  
1057 data-independent acquisition based label-free quantification. Proteomics [Internet]. 2015  
1058 Sep;15(18):3140–51. Available from: <http://doi.wiley.com/10.1002/pmic.201400396>

- 1059 99. Silva JC, Denny R, Dorschel C, Gorenstein M V., Li G-Z, Richardson K, et al. Simultaneous  
1060 Qualitative and Quantitative Analysis of the Escherichia coli Proteome. *Mol Cell Proteomics*  
1061 [Internet]. 2006 Apr;5(4):589–607. Available from:  
1062 <http://www.mcponline.org/lookup/doi/10.1074/mcp.M500321-MCP200>
- 1063 100. Kammers K, Cole RN, Tiengwe C, Ruczinski I. Detecting significant changes in protein  
1064 abundance. *EuPA Open Proteomics* [Internet]. 2015 Jun;7:11–9. Available from:  
1065 <https://linkinghub.elsevier.com/retrieve/pii/S2212968515000069>
- 1066 101. Ritchie ME, Phipson B, Wu D, Hu Y, Law CW, Shi W, et al. limma powers differential  
1067 expression analyses for RNA-sequencing and microarray studies. *Nucleic Acids Res* [Internet].  
1068 2015 Apr 20;43(7):e47–e47. Available from:  
1069 [http://academic.oup.com/nar/article/43/7/e47/2414268/limma-powers-differential-expression-](http://academic.oup.com/nar/article/43/7/e47/2414268/limma-powers-differential-expression-analyses-for)  
1070 [analyses-for](http://academic.oup.com/nar/article/43/7/e47/2414268/limma-powers-differential-expression-analyses-for)
- 1071 102. Storey JD. The positive false discovery rate: a Bayesian interpretation and the  $q$ -value. *Ann*  
1072 *Stat* [Internet]. 2003 Dec;31(6):2013–35. Available from:  
1073 <http://projecteuclid.org/euclid.aos/1074290335>
- 1074 103. Vizcaíno JA, Csordas A, Del-Toro N, Dianes JA, Griss J, Lavidas I, et al. 2016 update of the  
1075 PRIDE database and its related tools. *Nucleic Acids Res* [Internet]. 2016 Jan 4;44(D1):D447–  
1076 56. Available from: <https://academic.oup.com/nar/article-lookup/doi/10.1093/nar/gkv1145>
- 1077 104. Schardt A, Brinkmann BG, Mitkovski M, Sereda MW, Werner HB, Nave K-A. The SNARE  
1078 protein SNAP-29 interacts with the GTPase Rab3A: Implications for membrane trafficking in  
1079 myelinating glia. *J Neurosci Res* [Internet]. 2009 Nov 15;87(15):3465–79. Available from:  
1080 <http://doi.wiley.com/10.1002/jnr.22005>
- 1081 105. de Monasterio-Schrader P, Patzig J, Möbius W, Barrette B, Wagner TL, Kusch K, et al.  
1082 Uncoupling of neuroinflammation from axonal degeneration in mice lacking the myelin protein  
1083 tetraspanin-2. *Glia*. 2013;
- 1084 106. Jung M, Sommer I, Schachner M, Nave KA. Monoclonal antibody O10 defines a  
1085 conformationally sensitive cell- surface epitope of proteolipid protein (PLP): Evidence that PLP  
1086 misfolding underlies dysmyelination in mutant mice. *J Neurosci*. 1996;16(24):7920–9.
- 1087 107. Stumpf SK, Berghoff SA, Trevisiol A, Spieth L, Düking T, Schneider L V., et al. Ketogenic diet  
1088 ameliorates axonal defects and promotes myelination in Pelizaeus–Merzbacher disease. *Acta*  
1089 *Neuropathol* [Internet]. 2019 Jul 27;138(1):147–61. Available from:  
1090 <http://link.springer.com/10.1007/s00401-019-01985-2>
- 1091 108. Archelos JJ, Roggenbuck K, Scheider-Schaulies J, Lington C, Toyka K V., Hartung H-P.  
1092 Production and characterization of monoclonal antibodies to the extracellular domain of P0. *J*  
1093 *Neurosci Res* [Internet]. 1993 May 1;35(1):46–53. Available from:  
1094 <http://doi.wiley.com/10.1002/jnr.490350107>
- 1095 109. Darbas A, Jaegle M, Walbeehm E, van den Burg H, Driegen S, Broos L, et al. Cell autonomy of  
1096 the mouse claw paw mutation. *Dev Biol* [Internet]. 2004 Aug;272(2):470–82. Available from:  
1097 <https://linkinghub.elsevier.com/retrieve/pii/S0012160604003616>
- 1098 110. Catenaccio A, Court FA. Teased Fiber Preparation of Myelinated Nerve Fibers from Peripheral  
1099 Nerves for Vital Dye Staining and Immunofluorescence Analysis. In: *Methods in Molecular*

1100 Biology [Internet]. 2018. p. 329–37. Available from: <http://link.springer.com/10.1007/978-1->  
1101 [4939-7649-2\\_21](http://link.springer.com/10.1007/978-1-4939-7649-2_21)  
1102 111. Hulsen T, de Vlieg J, Alkema W. BioVenn – a web application for the comparison and  
1103 visualization of biological lists using area-proportional Venn diagrams. BMC Genomics  
1104 [Internet]. 2008;9(1):488. Available from:  
1105 <http://bmcbgenomics.biomedcentral.com/articles/10.1186/1471-2164-9-488>  
1106  
1107

1108 **FIGURE LEGENDS**

1109

1110

1111 **Figure 1. Proteome analysis of peripheral myelin**

1112 **(A)** Schematic illustration of a previous approach to the peripheral myelin proteome (41)  
1113 compared with the present workflow. Note that the current workflow allows largely automated  
1114 sample processing and omits labor-intense 2-dimensional differential gel-electrophoresis,  
1115 thereby considerably reducing hands-on time. Nano LC-MS analysis by data-independent  
1116 acquisition (DIA) using three different data acquisition modes provides efficient identification  
1117 and quantification of abundant myelin proteins ( $MS^E$ ; see **Figure 2**), a comprehensive  
1118 inventory ( $UDMS^E$ ; see **Figures 3-4**) and gel-free differential analysis of hundreds of distinct  
1119 proteins ( $DRE-UDMS^E$ ; see **Figure 5**). Samples were analyzed in three biological replicates.

1120 **(B)** Immunoblot of myelin biochemically enriched from sciatic nerves of wild-type mice at  
1121 postnatal day 21 (P21). Equal amounts of corresponding nerve lysate were loaded to  
1122 compare the abundance of marker proteins for compact myelin (MPZ/P0, MBP, PMP2), non-  
1123 compact myelin (PRX), the Schwann cell nucleus (KROX20/EGR2), axons (NEFH, KCNA1)  
1124 and mitochondria (VDAC). Blots show n=2 biological replicates representative of n=3  
1125 biological replicates. Note that myelin markers are enriched in purified myelin; other cellular  
1126 markers are reduced.

1127 **(C)** Number and relative abundance of proteins identified in myelin purified from the sciatic  
1128 nerves of wild-type mice using three different data acquisition modes ( $MS^E$ ,  $UDMS^E$ ,  $DRE-$   
1129  $UDMS^E$ ). Note that  $MS^E$  (orange) provides the best information about the relative abundance  
1130 of high-abundant myelin proteins (dynamic range of more than four orders of magnitude) but  
1131 identifies comparatively fewer proteins in purified myelin.  $UDMS^E$  (blue) identifies the largest  
1132 number of proteins but provides only a lower dynamic range of about three orders of  
1133 magnitude.  $DRE-UDMS^E$  (green) identifies an intermediate number of proteins with an  
1134 intermediate dynamic range of about four orders of magnitude. Note that  $MS^E$  with very high  
1135 dynamic range is required for the quantification of the exceptionally abundant myelin protein  
1136 zero (MPZ/P0), myelin basic protein (MBP) and periaxin (PRX). ppm, parts per million.

1137 **(D)** Venn diagram comparing the number of proteins identified in PNS myelin by  $MS^E$ ,  
1138  $UDMS^E$  and  $DRE-UDMS^E$ . Note the high overlap of identified proteins.

1139 **(E)** Venn diagram of the proteins identified in PNS myelin by  $UDMS^E$  in this study compared  
1140 with those identified in two previous approaches (41,42).

1141

1142

1143 **Figure 1-supplement 1. Clustered heatmap of Pearson's correlation coefficients for**  
1144 **protein abundance comparing data acquisition modes.**

1145 The heatmap compares the  $\log_2$  transformed ppm protein abundance values to assess  
1146 peripheral myelin purified from wild type mice using three data acquisition modes ( $MS^E$ ,  
1147  $UDMS^E$ ,  $DRE-UDMS^E$ ). The inset shows the color key and the histogram for the values of the  
1148 correlation coefficients. Note that the runs cluster with a high overall correlation ( $>0.75$ ) into  
1149 three conditions defined by the acquisition mode, in agreement with the experimental design.  
1150 Among the samples analyzed by different acquisition modes,  $DRE-UDMS^E$  similarly  
1151 correlates with both  $MS^E$  and  $UDMS^E$ , reflecting its intermediate nature.

1152

1153

#### 1154 **Figure 2. Relative abundance of peripheral myelin proteins**

1155  $MS^E$  was used to identify and quantify proteins in myelin purified from the sciatic nerves of  
1156 wild-type mice at P21; their relative abundance is given as percent with relative standard  
1157 deviation (% +/- RSD). Note that known myelin proteins constitute  $>80\%$  of the total myelin  
1158 protein; proteins not previously associated with myelin constitute  $<20\%$ . Mass spectrometric  
1159 quantification based on 3 biological replicates per genotype with 4 technical replicates each  
1160 (see **Figure 1-source data 1**).

1161

1162

#### 1163 **Figure 3. Developmental mRNA abundance profiles of myelin-associated genes**

1164 **(A)** K-means clustering was performed for the mRNA profiles of those 1046 proteins in our  
1165 myelin proteome inventory for which significant mRNA expression was found by RNA-Seq in  
1166 the sciatic nerve of rats dissected at ages E21, P6, P18 and 6 months (M6). [Note that this  
1167 filtering strategy allows to selectively display the developmental abundance profiles of those  
1168 transcripts that encode myelin-associated proteins rather than of all transcripts present in the  
1169 nerve.](#) Standardized mRNA abundance profiles are shown (n=4 biological replicates per  
1170 age). Known myelin genes are displayed in red. For comparison, *Pmp22* mRNA was  
1171 included although the small tetraspan protein PMP22 was not mass spectrometrically  
1172 identified due to its unfavorable distribution of tryptic cleavage sites. Normalized counts for all  
1173 mRNAs including those displaying developmentally unchanged abundance are provided in  
1174 **Figure 3-Source data 1**.

1175 **(B)** Numbers of mRNAs per cluster.

1176

1177

#### 1178 **Figure 4. Categorization of annotated protein functions**

1179 All proteins identified in peripheral myelin by  $UDMS^E$  (turquoise) and the respective  
1180 developmental expression clusters (**Figure 3**; shades of red) were analyzed for  
1181 overrepresented functional annotations using gene ontology (GO) terms. The graph displays

1182 the percentage of proteins in each cluster that were annotated with a particular function. For  
1183 comparison, known myelin proteins were annotated. n.o., not over-represented.

1184

1185

1186 **Figure 5. Molecular analysis of myelin in the *Prx*<sup>-/-</sup> mouse model of CMT4F**

1187 **(A)** Myelin purified from sciatic nerves dissected from *Prx*<sup>-/-</sup> and control mice at P21 was  
1188 separated by SDS-PAGE (0.5 µg protein load) and proteins were visualized by silver  
1189 staining. Bands constituted by the most abundant myelin proteins (MPZ/P0, MBP, PRX) are  
1190 annotated. Note that no band constituted by PRX was detected in *Prx*<sup>-/-</sup> myelin [and that](#)  
1191 [several other bands also display genotype-dependent differences in intensity](#). Gel shows n=2  
1192 biological replicates representative of n=3 biological replicates.

1193 **(B)** The relative abundance of proteins in myelin purified from *Prx*<sup>-/-</sup> sciatic nerves as  
1194 quantified by MS<sup>E</sup> is given as percent with relative standard deviation (% +/- RSD). Note the  
1195 increased relative abundance of MPZ/P0 and MBP compared to wild-type myelin (see  
1196 **Figure 2**) when PRX is lacking. Mass spectrometric quantification based on 3 biological  
1197 replicates with 4 technical replicates each (see **Figure 5-source data 1**).

1198 **(C,D)** Differential proteome analysis by DRE-UDMS<sup>E</sup> of myelin purified from *Prx*<sup>-/-</sup> and wild-  
1199 type mice. Mass spectrometric quantification based on 3 biological replicates per genotype  
1200 with 4 technical replicates each (see **Figure 5-source data 2**). **(C)** Top 40 proteins of which  
1201 the abundance is reduced (blue) or increased (red) in peripheral myelin purified from *Prx*<sup>-/-</sup>  
1202 compared to wild-type mice [with the highest level of significance according to the -log<sub>10</sub>](#)  
1203 [transformed q-value \(green\)](#). In the heatmaps, each horizontal line corresponds to the fold-  
1204 change (FC) of a distinct protein compared to its average abundance in wild-type myelin  
1205 plotted on a log<sub>2</sub> color scale. Heatmaps display [12 replicates, i.e. 3 biological replicates per](#)  
1206 [genotype with 4 technical replicates each](#). **(D-D''')** Volcano plots representing genotype-  
1207 dependent quantitative myelin proteome analysis. Data points represent quantified proteins  
1208 in *Prx*<sup>-/-</sup> compared to wild-type myelin and are plotted as the log<sub>2</sub>-transformed fold-change  
1209 (FC) on the x-axis against the -log<sub>10</sub>-transformed q-value on the y-axis. Stippled lines mark a  
1210 -log<sub>10</sub>-transformed q-value of 1.301, reflecting a q-value of 0.05 as significance threshold.  
1211 Highlighted are the datapoints representing the Top 10 proteins displaying highest zdist  
1212 values (Euclidean distance between the two points (0,0) and (x,y) with x = log<sub>2</sub>(FC) and y = -  
1213 log<sub>10</sub>(q-value) (red circles in **D**), immune-related proteins (purple circles in **D'**), proteins of  
1214 the extracellular matrix (ECM; yellow circles in **D''**) and known myelin proteins (blue circles in  
1215 **D'''**). n.d., not detected; n.q., no q-value computable due to protein identification in one  
1216 [genotype only](#). Also see **Figure 5-supplement 1**.

1217 **(E)** Immunoblot of myelin purified from *Prx*<sup>-/-</sup> and control sciatic nerves confirms the reduced  
1218 abundance of DRP2, SLC16A1/MCT1, BSG and PMP2 in *Prx*<sup>-/-</sup> myelin, as found by

1219 differential DRE-UDMS<sup>E</sup> analysis (in **Figure 5C,D**). PRX was detected as genotype control;  
1220 PLP/DM20 and ATP1A1 serve as markers. Blot shows n=2 biological replicates per  
1221 genotype.

1222 **(F)** Teased fiber preparations of sciatic nerves dissected from *Prx*<sup>-/-</sup> and control mice  
1223 immunolabelled for MAG (red) and SLC16A1 (green). Note that SLC16A1 co-distributes with  
1224 MAG in Schmidt-Lanterman incisures (SLI) in control but not in *Prx*<sup>-/-</sup> nerves, in accordance  
1225 with the reduced abundance of SLC16A1 in *Prx*<sup>-/-</sup> myelin (**Figure 5C-E**). Also note that, in  
1226 *Prx*<sup>-/-</sup> myelin, SLI were largely undetectable by MAG immunolabeling.

1227

1228

1229 **Figure 5-supplement 1. Clustered heatmap of Pearson's correlation coefficients for**  
1230 **protein abundance comparing genotypes.**

1231 **(A)** The heatmap compares the log<sub>2</sub> transformed ppm protein abundance values from the  
1232 DRE-UDMS<sup>E</sup> runs to assess peripheral myelin purified from wild type and *Prx*<sup>-/-</sup> mice. The  
1233 inset shows the color key and the histogram for the values of the correlation coefficients.  
1234 Note that the runs cluster with a high overall correlation (>0.85) into two conditions defined  
1235 by the genotype, in agreement with the experimental design.

1236 **(B)** Volcano plot representing genotype-dependent quantitative myelin proteome analysis.  
1237 Data points represent quantified proteins in *Prx*<sup>-/-</sup> compared to wild-type myelin plotted as the  
1238 log<sub>2</sub>-transformed fold-change (FC) on the x-axis against the -log<sub>10</sub>-transformed q-value on  
1239 the y-axis. Note the different axis scale compared to **Figure 5D**. Stippled line marks a -log<sub>10</sub>-  
1240 transformed q-value of 1.301, reflecting a q-value of 0.05 as significance threshold.  
1241 Highlighted is the datapoint for PRX to illustrate that only trace amounts of PRX were  
1242 detected when assessing *Prx*<sup>-/-</sup> myelin. ATP2A1, ATP1A4 and PLCD1 were not detected in  
1243 *Prx*<sup>-/-</sup> myelin.

1244

1245

1246 **Figure 6. Progressive loss and reduced diameters of peripheral axons in *Prx*<sup>-/-</sup> mice**

1247 **(A-D)** Genotype-dependent quantitative assessment of light micrographs of toluidine-stained  
1248 semi-thin sectioned quadriceps nerve dissected at 2, 4 and 9 months of age reveals  
1249 progressive loss of peripheral axons in *Prx*<sup>-/-</sup> compared to control mice.

1250 **(A)** Representative micrographs. Arrows point at myelinated axons; asterisk denotes an  
1251 unmyelinated axon; arrowhead points at a myelin whorl lacking a recognizable axon. Scale  
1252 bars, 10 μm.

1253 **(B)** Total number of axons per nerve that are not associated with a Remak bundle.

1254 **(C)** Total number of myelinated axons per nerve.

1255 **(D)** Total number per nerve of myelin whorls that lack a recognizable axon.



1256 Mean +/- SD, n=3-4 mice per genotype and age; \*P<0.05, \*\*P<0.01, \*\*\*P<0.001 by Student's  
1257 unpaired t-test.

1258 **(E-G)** Genotype-dependent assessment of myelinated axons shows a shift toward reduced  
1259 axonal diameters in quadriceps nerves of *Prx*<sup>-/-</sup> compared to control mice at 2 months **(E)**, 4  
1260 months **(F)** and 9 months **(G)** of age. Data are presented as frequency distribution with 0.5  
1261 μm bin width. \*\*\*, p<0.001 by two-sided Kolmogorow-Smirnow test. For precise p-values see  
1262 methods section.

1263

1264

1265 **Figure 1-source data 1. Label-free quantification of proteins in wild-type PNS myelin**  
1266 **fractions by three different data acquisition modes**

1267 Identification and quantification data of detected myelin-associated proteins. Tryptic peptides  
1268 derived from four technical replicates (replicate digestion and replicate injection) per three  
1269 biological replicate (20 sciatic nerves pooled from 10 animals) were analyzed by LC-MS (12  
1270 runs in total). Proteins (FDR < 1%; 2 peptides/protein) and peptides (FDR < 1%; ≥7 amino  
1271 acids) were identified by database search against the UniprotKB/SwissProt mouse database  
1272 using PLGS. Data were post-processed with the software package ISOQuant to calculate  
1273 absolute in-sample amounts for each detected protein based on the TOP3 approach.  
1274 Reported abundance values are defined as the relative amount of each protein in respect to  
1275 the sum over all detected proteins (ppm: parts per million (w/w) of total protein). Typical  
1276 contaminant proteins like keratins were filtered.

1277 → sheet 1: protein identification details

1278 → sheet 2: WT myelin proteome by MS<sup>E</sup>

1279 → sheet 3: WT myelin proteome by UD-MS<sup>E</sup>

1280 → sheet 4: WT myelin proteome by DRE UD-MS<sup>E</sup>

1281 → sheet 5: 45 proteins additionally identified in WT myelin by 1D-gel-LC-MS

1282

1283

1284 **Figure 3-source data 1. Normalized developmental mRNA abundance data**

1285 → sheet 1: normalized values for all individual 4 biological replicates per age

1286 → sheet 2: normalized values for biological replicates averaged to give mean per age

1287

1288

1289 **Figure 5-source data 1. Label-free quantification of proteins in PNS myelin fractions**  
1290 **from *Prx*<sup>-/-</sup> mice by MSe**

1291 Identification and quantification data of detected myelin-associated proteins. Tryptic peptides  
1292 derived from four technical replicates (replicate digestion and replicate injection) per three

1293 biological replicate (20 sciatic nerves pooled from 10 animals) were analyzed by LC-MS (12  
1294 runs in total). Proteins (FDR < 1%; 2 peptides/protein) and peptides (FDR < 1%; ≥7 amino  
1295 acids) were identified by database search against the UniprotKB/SwissProt mouse database  
1296 using PLGS. Data were post-processed with the software package ISOQuant to calculate  
1297 absolute in-sample amounts for each detected protein based on the TOP3 approach.  
1298 Reported abundance values are defined as the relative amount of each protein in respect to  
1299 the sum over all detected proteins (ppm: parts per million (w/w) of total protein). Typical  
1300 contaminant proteins like keratins were filtered.

1301 → sheet 1: protein identification details

1302 → sheet 2: *Prx*<sup>-/-</sup> myelin proteome by MS<sup>E</sup>

1303

1304

1305 **Figure 5-source data 2. Label-free quantification of proteins in PNS myelin fractions**  
1306 **from WT and *Prx*<sup>-/-</sup> mice by DRE-UDMS<sup>e</sup>**

1307 Identification and quantification data of detected myelin-associated proteins by DRE-UDMS<sup>e</sup>.  
1308 For each genotype, tryptic peptides derived from four technical replicates (replicate digestion  
1309 and replicate injection) per three biological replicate (20 sciatic nerves pooled from 10  
1310 animals) were analyzed by LC-MS (24 runs in total). Proteins (FDR < 1%; 2 peptides/protein)  
1311 and peptides (FDR < 1%; ≥7 amino acids) were identified by database search against the  
1312 UniprotKB/SwissProt mouse database using PLGS. Data were post-processed with the  
1313 software package ISOQuant to calculate absolute in-sample amounts for each detected  
1314 protein based on the TOP3 approach. Reported abundance values are defined as the  
1315 relative amount of each protein in respect to the sum over all detected proteins (ppm: parts  
1316 per million (w/w) of total protein). Typical contaminant proteins like keratins were filtered. The  
1317 -log<sub>10</sub>-transformed q-value was plotted against the log<sub>2</sub>-transformed fold change to obtain  
1318 the volcano plot shown in Figure 5D. As no imputation of missing values was performed,  
1319 proteins exclusive for only one of the conditions do not appear in the volcano plot, but are  
1320 appended at the end of the list. Criteria for statistically significant regulation were as follows:  
1321 fold change of at least 1.5 and q-value below 0.05.

1322 → sheet 1: protein identification details

1323 → sheet 2: comparison of WT vs. *Prx*<sup>-/-</sup> myelin proteome by DRE-UDMS<sup>E</sup>

1324

1325

Protein name	Gene	Reference	TMD	Cluster
2-hydroxyacylsphingosine 1-beta-galactosyltransferase	<i>Ugt8</i>	Bosio et al., 1996	2	P6-up
Syntrophin $\alpha$ 1	<i>Snta1</i>	Fuhrmann-Stroissnigg et al., 2012	-	P18-up
Annexin A2	<i>Anxa2</i>	Hayashi et al., 2007	-	Descending
Band 4.1 protein B / 4.1B	<i>Epb41l3</i>	Ivanovic et al., 2012	-	Descending
Band 4.1 protein G / 4.1G	<i>Epb41l2</i>	Ohno et al., 2006	-	P6-up
Breast carcinoma-amplified sequence 1	<i>Bcas1</i>	Ishimoto et al., 2017	-	P6-up
Cadherin 1/ E-Cadherin	<i>Cdh1</i>	Fannon et al., 1995	1	P18-up
Carbonic anhydrase 2	<i>Ca2</i>	Cammer et al., 1987	-	Descending
Catenin $\alpha$ 1	<i>Ctnna1</i>	Murata et al., 2006	-	U-shaped
Catenin $\beta$ 1	<i>Ctnnb1</i>	Fannon et al., 1995	-	Descending
Caveolin 1	<i>Cav1</i>	Mikol et al., 2002	1	P18-up
CD9, tetraspanin 29	<i>Cd9</i>	Ishibashi et al., 2004	4	P18-p
CD59A	<i>Cd59a</i>	Funabashi et al., 1994	1	P18-up
CD47, integrin-associated signal transducer	<i>Cd47</i>	Gitik et al., 2011	5	P6-up
CD81, tetraspanin 28	<i>Cd81</i>	Ishibashi et al., 2004	4	P18-up
CD82, tetraspanin 27	<i>Cd82</i>	Chernousov et al., 2013	4	P18-up
CD151, tetraspanin 24	<i>Cd151</i>	Patzig et al., 2011	4	P18-up
Cell adhesion molecule 4/ NECL4	<i>Cadm4</i>	Spiegel et al., 2007	1	P6-up
Cell division control protein 42	<i>Cdc42</i>	Benninger et al., 2007	-	P6-up
Cell surface glycoprotein MUC18	<i>Mcam</i>	Shi et al., 1998	1	Descending
Ciliary neurotrophic factor	<i>Cntf</i>	Rende et al., 1992	-	Late-up
CKLF-like MARVEL TMD-containing 5	<i>Cmtm5</i>	Patzig et al., 2011	4	P6-up
Claudin-19	<i>Cldn19</i>	Miyamoto et al., 2005	4	P6-up
Cofilin 1	<i>Cfl1</i>	Sparrow et al., 2012	-	Descending
Crystallin $\alpha$ 2	<i>Cryab</i>	d'Antonio et al., 2006	-	P18-up
Cyclic nucleotide phosphodiesterase	<i>Cnp</i>	Matthieu et al., 1980	-	P6-up
Sarcoglycan $\delta$	<i>Sgcd</i>	Cai et al., 2007	1	Late-up
Dihydropyrimidinase related protein 1	<i>Crmp1</i>	d'Antonio et al., 2006	-	Descending
Disks large homolog 1	<i>Dlg1</i>	Cotter et al., 2010	-	Descending
Dynein light chain 1	<i>Dynll1</i>	Mylykoski et al. 2018	-	P6-up
Dystroglycan	<i>Dag1</i>	Yamada et al., 1994	1	P6-up
Dystrophin/DP116	<i>Dmd</i>	Cai et al., 2007	-	P6-up
Dystrophin-related protein 2	<i>Drp2</i>	Sherman et al., 2001	-	P18-up
E3 ubiquitin-protein ligase NEDD4	<i>Nedd4</i>	Liu et al., 2009	-	Descending
Ezrin	<i>Ezr</i>	Scherer et al., 2001	-	P6-up
Fatty acid synthase	<i>Fasn</i>	Salles et al., 2002	-	P6-up
Flotillin 1	<i>Flot1</i>	Lee et al., 2014	-	P18-up
Gap junction $\beta$ 1 protein / Cx32	<i>Gjb1</i>	Li et al., 2002	4	P18-up
Gap junction $\gamma$ 3 protein / Cx29	<i>Gjc3</i>	Li et al., 2002	1	P6-up
Gelsolin	<i>Gsn</i>	Gonçaves et al., 2010	-	Late-up
Glycogen synthase kinase 3 $\beta$	<i>Gsk3b</i>	Ogata et al., 2004	-	P6-up
Integrin $\alpha$ 6	<i>Itga6</i>	Nodari et al., 2008	1	P6-up
Integrin $\alpha$ V	<i>Itgav</i>	Chernousov & Carey, 2003	1	Descending
Integrin $\beta$ 1	<i>Itgb1</i>	Feltri et al., 2002	1	Descending
Integrin $\beta$ 4	<i>Itgb4</i>	Quattrini et al., 1996	2	P18-up
Junctional adhesion molecule C	<i>Jam3</i>	Scheiermann et al., 2007	1	P18-up
Laminin $\alpha$ 2	<i>Lama2</i>	Yang et al., 2005	-	P6-up
Laminin $\alpha$ 4	<i>Lama4</i>	Yang et al., 2005	-	Descending
Laminin $\beta$ 1	<i>Lamb1</i>	LeBeau et al., 1994	-	Descending
Laminin $\beta$ 2	<i>Lamb2</i>	LeBeau et al., 1994	-	P18-up
Laminin $\gamma$ 1	<i>Lamc1</i>	Chen & Strickland, 2003	-	Descending
Membrane Palmitoylated Protein 6	<i>Mpp6</i>	Saitoh et al., 2019	-	P6-up
Microtubule-associated protein 1A	<i>Map1a</i>	Fuhrmann-Stroissnigg et al., 2012	-	P18-up
Microtubule-associated protein 1B	<i>Map1b</i>	Fuhrmann-Stroissnigg et al., 2012	-	P6-up
Mitogen-activated protein kinase 1/ ERK2	<i>Mapk1</i>	Mantuano et al., 2015	-	Descending
Mitogen-activated protein kinase 3/ ERK1	<i>Mapk3</i>	Mantuano et al., 2015	-	P18-up
Moesin	<i>Msn</i>	Scherer et al., 2001	-	Unchanged
Monocarboxylate transporter 1	<i>Slc16a1</i>	Domenech-Estevéz et al., 2015	11	P18-up

Myelin associated glycoprotein	<i>Mag</i>	Figlewicz et al., 1981	1	P6-up
Myelin basic protein	<i>Mbp</i>	Boggs, 2006	-	P6-up
Myelin protein 2	<i>Pmp2</i>	Trapp et al., 1984	-	P18-up
Myelin protein zero/ P0	<i>Mpz</i>	Giese et al., 1992	1	P6-up
Myelin proteolipid protein	<i>Plp1</i>	Garbern et al., 1997	4	P6-up
Myotubularin-related protein 2	<i>Mtmr2</i>	Bolino et al., 2004	-	P6-up
Noncompact myelin-associated protein	<i>Nemap</i>	Ryu et al., 2008	1	P18-up
NDRG1, N-myc downstream regulated	<i>Ndrg1</i>	Berger et al., 2004	-	P18-uP
Neurofascin	<i>Nfasc</i>	Tait et al., 2000	2	P18-up
Nidogen 1	<i>Nid1</i>	Lee et al., 2007	-	Descending
P2X purinoceptor 7	<i>P2rx7</i>	Faroni et al., 2014	-	P6-up
Paxillin	<i>Pxn</i>	Fernandez-Valle et al., 2002	-	P6-up
Periaxin	<i>Prx</i>	Gillespie et al., 1994	-	P6-up
Plasmalipin	<i>Plip</i>	Bosse et al., 2003	4	P18-up
Profilin 1	<i>Pfn1</i>	Montani et al., 2014	-	Descending
Lin-7 homolog C	<i>Lin7c</i>	Saitoh et al., 2017	-	P6-up
Rac1	<i>Rac1</i>	Benninger et al., 2007	-	U-Shaped
Radixin	<i>Rdx</i>	Scherer et al., 2001	-	Descending
RhoA	<i>Rhoa</i>	Brancolini et al., 1999	-	U-Shaped
Septin 2	<i>Sept 2</i>	Buser et al., 2009	-	Descending
Septin 7	<i>Sept 7</i>	Buser et al., 2009	-	U-Shaped
Septin 8	<i>Sept 8</i>	Patzig et al., 2011	-	P18-up
Septin 9	<i>Sept 9</i>	Patzig et al., 2011	-	P6-up
Septin 11	<i>Sept 11</i>	Buser et al., 2009	-	Descending
Sirtuin 2, NAD-dependent deacetylase	<i>Sirt2</i>	Werner et al., 2007	-	P18-up
Spectrin alpha chain, non-erythrocytic 1	<i>Sptan1</i>	Susuki et al., 2018	-	P18-up
Spectrin beta chain, non-erythrocytic 1	<i>Sptbn1</i>	Susuki et al., 2018	-	P18-up
Tight junction protein ZO-1	<i>Tjp1</i>	Poliak et al., 2007	-	P6-up
Tight junction protein ZO-2	<i>Tjp2</i>	Poliak et al., 2007	-	P6-up
Transferrin	<i>Tf</i>	Liu et al., 1990	2	Late-up
Vimentin	<i>Vim</i>	Triolo et al., 2012	-	Unchanged
Vinculin	<i>Vcl</i>	Beppu et al., 2015	-	Descending

**Table 1. Known myelin proteins in the myelin proteome.** Proteins mass-spectrometrically identified in peripheral myelin are compiled according to availability of prior references as myelin proteins. Given are the official gene name, one selected reference, the number of transmembrane domains (TMD) and the mRNA abundance profile cluster (see **Figure 3**).

1327  
1328  
1329  
1330  
1331

Protein name	Gene name	OMIM#	Gene Locus	Neuropathy
Monoacylglycerol lipase ABHD12	<i>ABHD12</i>	613599	20p11.21	PHARC
Apoptosis-inducing factor 1	<i>AIFM1</i>	300169	Xq26.1	CMTX4, DFNX5
Na <sup>+</sup> /K <sup>+</sup> -transporting ATPase $\alpha$ 1	<i>ATP1A1</i>	182310	1p13.1	CMT2DD
Cytochrome c oxidase subunit 6A1	<i>COX6A1</i>	602072	12q24.31	CMTRID
Dystrophin-related protein 2	<i>DRP2</i>	300052	Xq22.1	CMTX
Dynactin subunit 1	<i>DCTN1</i>	601143	2p13.1	DHMN7B
Dynamain 2	<i>DNM2</i>	602378	19p13.2	CMT2M, CMTDIB
Cytoplasmic dynein 1 heavy chain 1	<i>DYNC1H1</i>	600112	14q32.31	CMT20, SMALED1
E3 SUMO-protein ligase	<i>EGR2</i>	129010	10q21.3	CMT1D, CMT3, CMT4E
Glycine-tRNA ligase	<i>GARS</i> (Gart)	600287	7p14.3	CMT2D, HMN5A
Gap junction $\beta$ 1 protein / Cx32	<i>GJB1</i>	304040	Xq13.1	CMTX1
Guanine nucleotide-binding protein $\beta$ 4	<i>GNB4</i>	610863	3q26.33	CMTDIF
Histidine triad nucleotide-binding protein 1	<i>HINT1</i>	601314	5q23.3	NMAN
Hexokinase 1	<i>HK1</i>	142600	10q22.1	CMT4G
Heat shock protein $\beta$ 1	<i>HSPB1</i>	602195	7q11.23	CMT2F, DHMN2B
Kinesin heavy chain isoform 5A	<i>KIF5A</i>	602821	12q13.3	SPG10
Prelamin A/C	<i>LMNA</i>	150330	1q22	CMT2B1
Neprilysin	<i>MME</i>	120520	3q25.2	CMT2T, SCA43
Myelin protein zero/ P0	<i>MPZ</i>	159440	1q23.3	CHN2, CMT1B, CMT2I, CMT2J, CMT3, CMTDID, Roussy-Levy syndrome
Myotubularin-related protein 2	<i>MTMR2</i>	603557	11q21	CMT4B1
Alpha-N-acetylglucosaminidase	<i>NAGLU</i> (NAGA)	609701	17q21.2	CMT2V
NDRG1, N-myc downstream regulated	<i>NDRG1</i>	605262	8q24.22	CMT4D
Neurofilament heavy polypeptide	<i>NEFH</i>	162230	22q12.2	CMT2CC
Neurofilament light polypeptide	<i>NEFL</i>	162280	8p21.2	CMT2E, CMT1F, CMTDIG
Peripheral myelin protein 2	<i>PMP2</i>	170715	8q21.13	CMT1G
Peripheral myelin protein 22	<i>PMP22</i>	601907	17p12	CMT1A, CMT1E, CMT3, HNPP, Roussy-Levy syndrome
Ribose-phosphate pyrophosphokinase 1	<i>PRPS1</i>	311850	Xq22.3	Arts syndrome, CMTX5, DFNX1
Periaxin	<i>PRX</i>	605725	19q13.2	CMT4F, CMT3
Ras-related protein Rab 7a	<i>RAB7A</i>	602298	3q21.3	CMT2B
Septin 9	<i>SEPT9</i>	604061	17q25.3	HNA
Transitional ER-ATPase	<i>VCP</i>	601023	9p13.3	CMT2Y
Tryptophan-tRNA ligase, cytoplasmic	<i>WARS</i>	191050	14q32.32	HMN9
Tyrosine-tRNA ligase, cytoplasmic	<i>YARS</i>	603623	1p35.1	DI-CMTC

1333 **Table 2. Peripheral myelin proteins identified in PNS myelin involved in neuropathological diseases.** Proteins  
1334 massspectrometrically identified in peripheral myelin were analyzed regarding the involvement of the ortholog human gene  
1335 in neuropathological diseases. PMP22 was added, though it was not identified by MS analyses due to its unfavorable  
1336 distribution of tryptic cleavage sites. CMT, Charcot-Marie-Tooth disease; DHMN, distal hereditary motor neuropathy; DI-  
1337 CMTC, dominant intermediate CMTC; DFN, X-linked deafness; HMN, hereditary motor neuropathy; HSAN, hereditary  
1338 sensory and autonomic neuropathy; HNA, hereditary sensory and autonomic neuropathy; OMIM, Online Mendelian  
1339 Inheritance in Man; PHARC, polyneuropathy, hearing loss, ataxia, retinitis pigmentosa and cataract; SCA, spinocerebellar  
1340 ataxia; SPG, spastic paraplegia.